The Effect of Aluminum Content and Processing on the Tensile Behavior of High Pressure Die Cast Mg Alloys

by

Erin M. Deda

A dissertation submitted in partial fulfillment
of the requirements for the degree of
Doctor of Philosophy
(Materials Science and Engineering)
in The University of Michigan
2017

Doctoral Committee:
Professor John E. Allison, Chair
Professor J. Wayne Jones
Professor Amit Misra
Associate Professor Veera Sundararaghavan

“And bless our loved ones wherever they may be.”

Acknowledgements

I would like to express my gratitude to Professor John Allison for his support and guidance throughout my time at the University of Michigan. I would also like to thank the rest of my committee Professor J. Wayne Jones, Professor Amit Misra, and Assoc. Professor Veera Sundararaghavan for their insights and helpful critiques.

In addition, thanks to our collaborators at Pacific Northwest National Lab and Ford Motor Company Research and Innovation Center. Dr. Xin Sun, Dr. Erin Barker, and Dr. Kyoo Sil Choi at PNNL provided a great many insightful discussions. Dr. Mei Li, Dr. Joy Forsmark, Dr. Larry Godlewski, and Dr. Jacob Zindel at Ford Research and Innovation who provided the castings and fruitful discussions regarding the casting process. Special thanks also to Professor Samantha Daly, for her support, encouragement and advice, as well as the use of the microtensile stage.

I would also like to extend a thank you to all of the colleagues whose support and discussions have made this work more pleasant and productive. Dr. Tracy Berman, Dr. Zhe Chen, Dr. Alfred Okello, Dr. Jason Geathers, Jacob Adams, Alan Githens, Joyce Gong, Sinsar Hsie, Aeriel Murphy, Maya Nath, Vir Nirankari, and Anna Trump. Their assistance made all the difference.

In addition, the support of all of my friends and family near and far made all of the difference. Thanks to my Dad and brother for their support and encouragement. My partner, Alex, for his endless support and care, this would not have happened without you. The support of the

community of Ann Arbor Roller Derby means more than just the athletic pursuits we have in common. The support of Dr. Jillian Bellovary, Dr. Amy Hillard, Jenny Metzger Hansen, Christy Varner, and the rest of the Ann Arbor Brawlstars was invaluable through this process. I am so thankful to have all of you in my life.

Finally, to acknowledge the funding of this work from Department of Energy and Rackham Graduate School. This work was supported by the Department of Energy Office of Vehicle Technologies under the Automotive Lightweighting Materials Program managed by Dr. Will Joost, via subcontract with Pacific Northwest National Laboratory. In addition, I was supported by a Rackham Merit Fellowship. I would like to thank the Horace H. Rackham Graduate School for financial travel awards that supported travel to conferences throughout my work.

Table of Contents

List of Tables

List of Figures

Abstract

Due to their high specific strength and good castability, magnesium alloys are desirable for use in weight reduction strategies in automotive applications. However, the mechanical properties of high pressure die cast (HPDC) magnesium can be highly variable and dependent on location in the casting. To better understand the relationship between microstructure and tensile properties, the influence of alloying and section thickness on the microstructural features and tensile properties of Mg-Al and Mg-Al-Mn alloys is quantified. This investigation provides experimental input to modeling activities for the development of an Integrated Computational Materials Engineering capability, to assess and quantify the impact of microstructure on the tensile behavior of HPDC Mg AM series (magnesium-aluminum-manganese) alloys.

As a result of this work, it is found that with increasing aluminum content, the yield strength increases and the ductility decreases. Increasing the plate thickness results in a decrease in both the yield strength and ductility. HPDC components have varying microstructural features through the plate thickness, developing a "skin" and "core". The grain size, beta-$Mg_{17}Al_{12}$ phase, and solute content are all quantified through the thickness of the plates. By quantifying microstructural variations, a physics-based model has been developed which is able to predict the effects of alloying and plate thickness on yield strength. The primary factors affecting strengthening are accounted for using a linear superposition model of solid solution, grain size, and dispersion hardening. This model takes into account through-thickness microstructure gradients that exist in HPDC components by using a composite model to incorporate the skin and core changes. The

yield strength in these alloys is dominated by grain boundary strengthening and solute hardening effects.

In order to isolate the effects of eutectic phases, shrinkage porosity and oxide films on strength and ductility, HPDC plates were solution treated and processed by hot isostatic pressing. It is found that there is a hierarchical effect on ductility associated with these features - oxide films have the most deleterious effect, followed by shrinkage porosity and finally beta-phase volume fraction. By identifying the critical microstructural features, we can better predict and design for the desired properties during the manufacturing process.

Chapter 1

Introduction

1.1 Motivation

Magnesium alloys are being widely explored for use in automotive applications for vehicle weight reduction due to their high specific strength [1,2]. Magnesium is the lightest structural metal with a density of 1.7 g/cm^3. One recent example of the utilization of Mg to reduce the overall weight in vehicles is the 2010 Lincoln MKT rear liftgate inner panel – a 1.3m x 1.3m single casting which was designed to be lighter to avoid redesigning the lift system [3]. By using high pressure die casting to form these Mg alloys, components can be made in large, complex, thin-walled geometries, which also minimizes the finishing steps.

One common die casting alloy system is the AM series (magnesium-aluminum-manganese). It is popular due to the combination of ductility and strength, and good energy absorption exhibited by alloys AM50 and AM60 [4]. However, Al content can have a significant influence on the mechanical properties of these alloys. For example, when comparing two common casting alloys, AM50 (Mg-5Al-0.5Mn) and AM60 (Mg-6Al-0.5Mn), it is observed that with increased Al content, ductility is reduced and yield strength increases [5,6]. There is also a high degree of variability observed in the tensile behavior of these die cast alloys – Alain et al. reported that the average ductility varies by up to 50% for ten tensile tests [7]. This is associated with the

variation in the microstructure and casting defects. Increased use of Mg alloys in crash sensitive applications requires improved strength and ductility with better predictability.

Currently, the high variability observed within a single cast part makes it difficult to design and optimize parts for the average properties [5]. This results in overdesign of components, which minimizes the weight reduction that can be achieved. This unpredictability in failure behavior has been shown to be related to casting features including porosity, oxide films, and eutectic phases along the grain boundaries [8]. By improving our understanding of the mechanical behavior of these alloys, these materials can be used to more fully address needs of industry for increased usage in weight reduction strategies.

This chapter provides a review of the high pressure die casting process, the microstructural features and tensile behavior in these alloys, and our current understanding of these properties. The objective of this review is to summarize the current state of research in the microstructure and tensile behavior of HPDC Mg alloys, and to identify shortcomings in our understanding.

1.2 Production and Processing

1.2.1 High Pressure Die Casting

High pressure die casting (HPDC) is a largely automatic, high volume process. A diagram of the high pressure die casting process is shown in Figure 1.1. HPDC is a process which consists of the rapid injection of molten metal into a die using a hydraulic plunger, allowing it to cool, and removing the part. During HPDC, molten metal is poured into the shot sleeve. Once the metal is in the shot sleeve, the plunger moves at a varied pace to move the metal into the die, as determined by the desired shot speed. Once the part has cooled, it is ejected from the die, and the excess material removed. The HPDC process provides a high level of productivity and quality for mass produced components. It produces parts with a high quality surface, fine grain structure, and a thin,

complex structure with little machining required to finish the parts [9]. Four base metals that are commonly used for HPDC components are aluminum, magnesium, zinc, and copper alloys due to their low melting points [10].

The properties of parts produced by HPDC are strongly dependent on the casting parameters including melt temperature, shot speed, and gating configuration in the part [5]. The cold walls of the die produce a rapid cooling rate, on the order of 100 to 1000 K s^{-1} [11]. HPDC is a rapid, turbulent flow process which results in a range of microstructures due to the high rate of filling and solidification.

Super vacuum die casting (SVDC), or vacuum assisted high pressure die casting, is the application of vacuum pressure in the die cavity during casting. This process was developed for use in Mg alloys in 2009 [12]. It is the maintenance of a vacuum pressure in the die of <60 mbar in order to dramatically reduce the entrapped gas (air) porosity, which is common in die castings [13]. Prior to the use of SVDC, heat treatment of die cast Mg alloys was not considered to be possible due to expansion of the air bubbles at typical solution treatment temperatures which produces blistering on the casting surfaces. Due to the reduction in entrapped air bubbles with SVDC, Mg die cast alloys can be heat treated using standard methods. This has been demonstrated in AZ91 alloys, where the effects of aging on the microstructure have been studied [14,15]. In castings of the same structure, it has been shown that the SVDC process improves the mechanical properties [12].

1.3 Microstructure Characterization

In the process of casting these alloys, a number of intrinsic and extrinsic microstructural features develop. Intrinsic microstructural features are those that are related to the microstructure

and composition of the alloy – such as composition variation and formation of eutectic phases. Extrinsic features are those that are uniquely related to the manufacturing process. The HPDC process leads to extrinsic features specific to die casting including entrapped air, porosity, heterogeneous microstructures (e.g., externally solidified crystals), and large casting defects such as oxides and hot tears. All of these features and defects impact the overall tensile behavior in different ways, which will be discussed in the following sections.

1.3.1 Intrinsic Features

Mg alloys are the lightest structural metal, with a hexagonal close packed (hcp) crystal structure [16]. By alloying with Al, the strength, corrosion resistance, and castability are all improved [17]. Al is also slightly less costly compared to Mg, allowing property improvements at a reasonable cost compared to other common alloying elements, such as rare earth metals. Frequently, when Al is added to Mg as an alloying element, Mn is also. Mn reduces the solubility of Fe in Mg, which is typically detrimental to the corrosion resistance in Mg alloys. The nomenclature used for commercial Mg alloys consists of the letters designating an alloying element, followed by the integer signifying the rounded weight percentage. Alloying elements reference in this work include aluminum (A), manganese (M), and zinc (Z). The alloy systems commonly referred to in this work are the AM series, such as AM60 (Mg – 6 wt.% Al – 0.5 wt.% Mn) and the AZ series, such as AZ91 (Mg – 9 wt.% Al – 1 wt.% Zn).

The effects of alloying elements determine much of the relevant variation in the intrinsic microstructural features in Mg alloys. Al is one of the most important alloying elements for Mg. It readily dissolves in Mg up to a solubility limit of 12.6 wt.%. Above the solubility limit, the β-$Mg_{17}Al_{12}$ eutectic phase forms, as shown in Figure 1.2. These intrinsic microstructural features in

AM series alloys are the grain size, and the formation of secondary eutectic phases including β-$Mg_{17}Al_{12}$ and AlMn phases.

HPDC produces a fine-grained, randomly textured material. Typical grain sizes in HPDC Mg alloys are on the order of 5-10 μm. There is no preferred texture associated with die cast material, that is, the grains are randomly oriented, which is in stark contrast to the strong basal textures typically developed in other manufacturing methods, such as rolling and extrusions [18]. Grain size in HPDC alloys is typically predicted to be controlled by the cooling rate [19]. There is some conflicting research regarding the effect of alloying on the grain size of HPDC alloys. Some research shows that there is a decrease in grain size with increasing Al content [20], due to growth restriction factors in Mg alloys [21,22]. This effect of Al on grain size is was not observed in other investigations, which show no change in the grain size with alloying or distance from the casting surface [23]. The lack of change in grain size could be related to observation that the change in grain size with alloying is most apparent in very low Al composition alloys, less than 2 wt.% Al [20]. Previous work in die cast AZ91 has shown an increase in the average grain size from the surface of the casting to the center [24,25].

Aluminum partitions during the solidification process, leading to coring of the grains, with increasing aluminum content towards the cell boundaries which are the last regions to solidify [26]. This coring is due to the rapid solidification rate, which results in Al rich α-Mg near the grain boundaries [27]. This change in solute content is predicted by Scheil solidification, which is frequently used to predict the fraction of secondary phases in HPDC parts. Scheil solidification assumes that no diffusion or solute redistribution occurs in the solid due to rapid solidification, complete mixing in the liquid, and that equilibrium is maintained between the solid and liquid phases [28]. Compared to equilibrium solidification, by using the assumptions made in the Scheil

equation, we can more accurately describe the kinetics of segregation during HPDC. The segregation behavior is predicted to influence the mechanical properties, as it is found that increasing Al content in α-Mg solid solution decreases the lattice parameters, and increases the c/a ratio [29].

The primary eutectic phase in these alloys is the β-$Mg_{17}Al_{12}$ eutectic phase. β-$Mg_{17}Al_{12}$ forms a complex BCC structure, which has an incoherent interface with the hcp α-Mg phase [30]. It has been reported that the high cooling rate associated with HPDC results in the formation of a divorced eutectic structure, with small α-Mg grains and a fine distribution of β-$Mg_{17}Al_{12}$ along the grain boundaries [31]. Previous work has shown that composition and cooling rate determines the nature of the eutectic - at higher cooling rates, there are more dendritic structures, which limit the growth of β-$Mg_{17}Al_{12}$, creating a divorced structure. A divorced structure is composed of highly segregated zones of each phase.

In general, with increasing Al content, the β-phase fraction increases. As Al content increases, the morphology of the β-$Mg_{17}Al_{12}$ eutectic phase changes from divorced (<6wt%) to fibrous (9-20wt%) to lamellar(>20wt%) [32]. For Al contents less than 6wt%, β-$Mg_{17}Al_{12}$ appears as discrete particles surrounded by regions of α-Mg that are Al rich, with α-Mg grains [32,33]. Barbagallo has conducted a thorough examination of the divorced eutectic formed by β-$Mg_{17}Al_{12}$ during the casting process. The rapid cooling rate associated with HPDC produces a fully divorced eutectic due to the formation of fine α-Mg grains on the surface of the mold, and β-$Mg_{17}Al_{12}$ on the cell boundaries [31]. This transitions to a partially divorced eutectic above 6wt%Al, where islands of α-Mg form within the β-$Mg_{17}Al_{12}$ [34]. A 3-D morphology assessment of β-$Mg_{17}Al_{12}$ in AZ91 shows uniform α–Mg grains at the surface of the casting, with eutectic β-$Mg_{17}Al_{12}$ forming at the surface of the grains [35]. In alloys with higher aluminum contents, such as in AZ91, β-

$Mg_{17}Al_{12}$ forms an interconnected scaffold network throughout the entire matrix. Song et al. found that regions near the surface (the skin) of HPDC Mg AZ91 alloys show a higher volume fraction of β-$Mg_{17}Al_{12}$ and continuous distribution of the β-phase [36]. Song's results conflict with Prakash however, as they show no variation in β-$Mg_{17}Al_{12}$ through the thickness [37].

AlMn phases are distributed randomly throughout the thickness of the casting. The manganese content in the matrix is much lower than nominal, indicating that most of the manganese is present in the form of AlMn precipitates [38]. These phases are predicted to be Al_8Mn_5, $AlMn_4$, and $Al_{11}Mn_4$ using the TCMG4 database in ThermoCalc. Al_8Mn_5 also has an HCP crystal structure, and has been verified to be present in AM50 alloys [38,39]. There is little quantitative work on these precipitates, though they are noted in many microstructural analyses of AM series alloys. Initial characterization by Wei et al. suggest that there are two types of phases: type 1 equiaxed or short bar phase morphology and type 2 a flower shaped morphology, both of which are BCC crystal structures [40]. It is likely that the equiaxed AlMn particles are formed in the melt, and are potential nucleation points for the flower type precipitates observed in AM series Mg alloys. The equiaxed particles have a higher Mn/Al ratio than the flower particles. By increasing the amount of Mn in the alloy, the number of Mn particles likely increases [34], due to the low solubility of Mn in a Mg matrix, with a maximum solubility of 2 wt.% Mn.

1.3.2 Extrinsic Features

High pressure die casting generates extrinsic microstructural features specific to the process. These extrinsic features include the formation of a skin and core microstructure, externally solidified crystals (ESCs), shrinkage porosity, air entrapment, and oxide films.

The formation of a skin and core microstructure has been widely studied in die cast alloys, though there is some disagreement on precisely how to define the "skin" of a casting. Initially, the

skin thickness was defined as the distance to the defect band from the surface [41]. Defect bands are theorized to form from strain localizations during the solidification process [42,43]. Defect bands have been found to form inconsistently, and at irregular intervals within a casting. Due to this inconsistency, the formation of a skin has also been defined in terms of plasticity, as measured by the hardness through the thickness of the casting [44–46]. Additionally, the skin has been defined as the change in grain size [45,47,48], occurrence of ESCs and change in areal fraction of eutectic phase [47]. There is currently no consistent standard for the determination of the skin, and it remains a current area of research [19].

Externally solidified crystals (ESCs) (also referenced as externally solidified grains) are large, dendritic α-Mg grains typically found in the core of HPDC components. ESCs form in the shot sleeve thus the nomenclature that solidification occurs "external" to the part mold. Rather they begin to form as soon as molten metal is poured into the shot sleeve and heat is removed. These grains nucleate and begin to grow even before injection into the die and thus the metal entering the part mold is somewhat semi-solid. Once ESCs have entered the die, it has been found that ESCs segregate to the center of the casting until a maximum packing is reached [49]. The amount of segregation that then occurs is predicted to be determined by the number of ESCs and die temperature. With ESCs segregated to the center of the casting, a defect band can form between the finer grains on the walls of the die and the ESCs [10,42]. Operationally, the minimum ESC size is determined to be 30 μm in diameter, with a maximum grain diameter typically observed of 300 μm [50]. In addition, a change in the solute content is observed across the diameter of an ESC, with very low Al contents in the center [51,52]. This leads to the prediction of significant effects of the ESCs on the mechanical behavior of HPDC alloys [53].

Shrinkage porosity occurs due to the contraction of the melt by cooling rapidly in the mold leading to the formation of pores where the grains pull apart due to shrinkage during the cooling process. Shrinkage porosity has also been predicted to form around impurities such as oxide inclusions and other metal impurities in the melt [54,55]. Shrinkage porosity is frequently observed in bands, which has been attributed to an initial influx of metal which coats the walls of the mold, and then a second front fills the center of the mold, which is filled with a semi-solid mixture of molten Mg and externally solidified crystals (ESCs). This leads to a band of shrinkage porosity and defects between the initial and secondary flow patterns [32,36]. Shrinkage porosity is also observed around the edges of ESCs, where the dendrite arms have small gaps formed during the cooling process [53].

The other form of porosity in these castings is gas, or entrapped air, porosity. This is due to the presence of air in the die cavity during the casting process. This air can be entrapped by the rapidly moving molten metal front and lead to air bubbles that remain throughout the casting after solidification. Entrapped air pores range in size from 20 to over 100 μm in diameter [56]. The location of gas pores varies through the thickness of the casting, with no obvious pattern to the locations observed, though they are frequently found at the intersection of melt fronts. Gas porosity can be minimized by the usage of SVDC, which results in much lower porosity levels [3].

Oxide bifilms are common in cast oxidizing metals, Mg and Al, and are largely detailed by the work of Campbell [57]. These films are the results of an oxide film forming on the surface, and upon removal of the melt from the pot for casting or mixing, the film forms a fold in the melt. This folded bifilm can result in the formation of an incipient crack in the microstructure [58]. Oxide films are typically seen as a strong contributor to early failure of castings, including both magnesium and aluminum alloy castings [55]. In particular, this has been shown in research on

the fatigue life of these castings, where a common feature on the fracture surface is a straightened bifilm [59]. It is also predicted that the number of pores in the microstructure are affected by the number of oxide films, as they are thought to be heterogenous nucleation sites for porosity [60]. These films have been isolated in A206 Al alloys though the use of HIP, and have been shown to have a significant effect on the mechanical behavior of castings [61].

In summary, it is found that the intrinsic and extrinsic microstructural features of these alloys are all heavily impacted by the casting parameters. In turn, these microstructural features tend to have a significant impact on the mechanical behavior of the castings, as discussed in the next section.

1.4 Tensile Behavior of HPDC alloys

HPDC generates a broad distribution of microstructural features dependent on casting related factors, such as gating structure and flow patterns of the molten metal. These features can have a strong effect on the local mechanical properties, which affect the component level behaviors [5]. In order to better understand these effects, tensile tests on simpler components can give insight into the mechanical properties on a local level, and better understand the microstructure-property relationship to go into the design of larger components.

The mechanical properties of Mg depend on the effects of alloying. In general, with increasing Al content, the yield strength increases and strain hardening exponent and ductility both decrease [62–67]. Yield strength is found using the 0.2% offset method in Mg alloys. The yield strength in these alloys has been shown to be a function of solid solution strengthening, dispersion hardening, and grain boundary strengthening [68,69]. This is discussed in detail in section 1.7.1. The strain hardening exponent in these alloys is frequently characterized using the Hollomon

formulation, which is shown in Equation 1.1. This is determined by a fit of the true stress-true strain curve with an exponential term, which is the strain hardening exponent, n. This is one of the common constitutive models of the stress-strain behavior. High strain hardening exponents indicate that more plastic flow is possible, and that the formabilty is increased relative to conditions with low strain hardening exponents.

[1.1] $\sigma = K\varepsilon^n$

The hardness and yield strength has been observed to be higher for the skin section due to the denser grain structure and decrease in voids, while fracture is typically initiated at the larger individual pores and regions which have clusters of pores [46]. This increased hardness of the skin is likely based on the change in average grain size, and formation of eutectics between the grains. The higher hardness in the skin is attributed to the fine grained nature of the skin as compared to the core, which tends to have a much larger ESC fraction, and a lower average strength. ESCs tend to have a large deleterious effect on the strength of these castings due to reduction in area of the fine grained regions [70]. The skin has been shown to impact both the strength and the ductility in these alloys [50,7]. By removing the cast skin, more defects are typically exposed to the surface, and this significantly reduces the observed yield strength and ductility. Additionally, through the thickness there is an effect of both solute content eutectic phase formation. Work in AM50 predicts that solute distribution has an effect on the strength of these alloys [71], but that the mechanisms are still unclear. The β-phase changes shape through the thickness of the plate, and this is predicted to change the nature of the dispersion strengthening. The structure of the eutectic phase whether isolated point precipitates or larger network structures may play a role in the strengthening behavior [69,72,73]

Increasing the aluminum content also increases the castability, and is predicted to decrease the grain size [63]. In theory, ductility is limited by a combination of the intrinsic ductility and the castability (extrinsic factors), leading to an optimum Al content in different types of castings. This relationship is still unclear, so in order to optimize parts for specific use cases, accurate models of the different processing effects on tensile behavior, especially ductility, need to be developed and validated.

Ductility in Mg alloys is generally thought to be reduced due to presence of entrapped air and shrinkage microporosity at grain boundaries as well as the brittle $Mg_{17}Al_{12}$ particles that are found in the grain boundaries as divorced eutectic phases [54]. The primary reduction in ductility is predicted to be due to the porosity in the castings. Song et al. reported that the UTS and elongation increase with a decrease in the size of the void or fracture initiation site [74]. In addition, α-Mg has an hcp structure, while the β-phase is a complex bcc structure. This results in a lattice mismatch and has been proposed to lead to decreased ductility due to an increase in internal strains [31]. Barbagallo has associated the value of the internal strains as a function of the gradient of Al content through the grain. [31] By varying the aluminum content, the amount of β-phase is varied, which is one location where phase decohesion can occur. However Song et al. have used in-situ deformation observations to show that decohesion and detachment of β-phase only occurs in the late stages of plastic deformation and fracture tends to occur through regions with either coalesced or large micro-voids [74,75]. Some studies have shown that the boundary between β-phase and α–Mg is semi-coherent indicating the complexity of this problem [14].

The effect of section thickness on the tensile properties has also been studied, and inconsistent results are found [64,74,76]. Song et al. showed that for increasing specimen thickness in AM50, UTS and elongation decrease, and then increase again, while yield strength consistently

decreases. The minimum occurs at 6mm section thickness with an elongation of 5% [74]. This was likely due to an increase in the number of micro-voids in the specimen at that thickness, as they only tested one specimen of each thickness. The variation of micro-voids within each thickness was not well characterized, which may explain why these results are inconsistent with earlier results from Abbott et al. [64]. Abbott et al. showed elongation and UTS decrease from their peak value with respect to thickness with a maximum elongation of 13% at 5mm thick in AM60. The thickness effect has been attributed to the effect on grain size and dendrite structure. In a thinner walled structure, the cooling rate is higher than in comparatively thicker walled structures, which leads to a finer grain size [4].

There is a large variation in tensile properties between casting processes, though yield strength is highly consistent within samples from the same casting process. Additional work from Aghion et al. shows that with increasing section thickness, the yield strength decreases, and elongation increases and decreases from the peak, which is consistent with Abbott et al. [77]. Aghion et al. noted that porosity decreased with increasing wall thickness, and that as wall thickness increases, the average grain diameter increases. This is theorized to be due to the decreased cooling rate for thicker specimens. With increasing grain diameter (increased solidification time), the impact energy is reduced. Prior work from Zhou et al. also contrasts with Aghion et al. however, where Zhou et al. shows that bulk porosity increases with section thickness, as well as UTS, yield strength and elongation in an AM50 alloy [76]. There is clearly still disagreement in literature on how section thickness impacts the tensile behavior. This could be related to the strong impact of casting parameters on the grain size in a given casting.

In addition, porosity is traditionally shown to be detrimental to the tensile properties. This is shown in the research on section thickness, as well as computational modeling of the effect of

porosity. It is found that the use of SVDC improves the mechanical properties of die cast Mg alloys compared to HPDC in both AM60 and AZ91 for the same component [3,12]. This is due to the reduction in porosity observed through the use of vacuum assisted die casting. However, ductility cannot be modeled solely by porosity effects. Elongation has been shown to decrease with increasing porosity area fraction. However, there are also situations in which with the same porosity level produces a range of elongations. This is likely at least partially due to bulk casting defects. There are multiple extrinsic casting defects that can have a deleterious effect on ductility. This shows how much the tensile behavior can vary within a single casting, and is extremely dependent on the local microstructural features developed [78].

1.5 Processing

In order to isolate different microstructural features intrinsic to the high pressure die casting process, solution heat treatment (ST) and hot isostatic pressing (HIP) are used. These techniques are only recently available for use in HPDC parts with a reduction in gas entrapment porosity [79] with technologies such as SVDC. Previously, the heat treatment process would result in failure of the part due to cracking and blistering. Due to the rapid solidification process of HPDC, eutectic phases form at the grain boundaries in these alloys. In order to remove these eutectic phases, solution heat treatment is utilized. Solution heat treatment involves holding the component at a temperature just below the eutectic temperature, in order to dissolve the eutectic phases. This is followed by water quenching to hold the alloying elements in solid solution [80].

Solution treatment of HPDC alloys has been shown to dissolve the β-phase [81]. The duration of solution treatment determines the degree of dissolution, and solute distribution in the matrix [71]. In AZ91, it has been shown that the dissolution of β-phase is diffusion controlled, and can be fully dissolved in one hour at 400°C [82]. If the ST time is not limited, grain growth

has been observed with increasing solution treatment times [83]. By limiting the ST time to the minimum to dissolve the β-phase, the effects can be isolated with minimal change to the grain size. Aging is not considered in this study, though high Al AM series (> 7 wt.%) have been found to slightly age harden [13].

HIP is the application of high temperature and pressure in order to densify a material [84]. In the case of castings, HIP is used to reduce the shrinkage porosity. Since the pores are due to shrinkage of the metal during the cooling process, they are generally assumed to be a vacuum with no entrapped gas, and the surfaces can weld or "heal" during the HIP process. HIP does not significantly influence castings with entrapped air bubbles since the process cannot reduce the size and volume fraction of the entrapped gases. The HIP process has been used to significantly reduce the porosity in aluminum die castings [61,85], however only limited investigation of this process has been conducted for magnesium castings [84,86–89]. Studies on the influence of HIP on the mechanical properties in Mg AZ91 suggests that the reduction in porosity improves the yield strength, UTS, and ductility [84]. In Al alloys, HIP has been shown to significantly improve the fatigue life due to the reduction in shrinkage porosity [61]. By utilizing ST and HIP in these alloys, the microstructural features can be systematically varied.

1.6 Modeling approaches for yield strength and ductility

In order to better use Mg die castings in production parts, a better understanding of the effect of microstructure on the tensile behavior is needed. To that end, both analytical and numerical models have been used for the prediction of the mechanical properties. These models are developed as part of an integrated computational and materials engineering (ICME) approach to reduce the time to production, by aiming to connect material manufacturing and design [90,91].

1.6.1 Yield Strength

The yield strength of die cast Mg alloys has been shown to be a function of solid solution strengthening, grain boundary hardening, and dispersion hardening [69]. In order to predict strengthening, it is typically broken down into an additive model based on linear superposition of the above strengthening mechanisms. The grain size effect on yield strength of polycrystalline alloys is described by the Hall-Petch relationship, Equation 1.2 [92,93]. Solid solution strengthening has been accurately predicted by Yasi et al [94]. Yasi uses solute misfit interactions as calculated from a density functional theory model as input to a Fleischer solid solution model to predict strengthening effects of solutes, given by the term σ_{ss} [94]. This can be combined with Hall-Petch relationship, which relates the yield strength to the grain size, and the intrinsic strength of the material [95]

$$[1.2]\ \sigma_y = \sigma_0 + k * d^{-\frac{1}{2}}$$

As shown in Equation 1.2, σ_y is the yield strength of the material, σ_o is the intrinsic, or friction stress, k is the locking parameter, and d is the average grain size of the material. The grain size, d, has been shown to be dependent on the casting conditions in these alloys [23]. The intrinsic strength, grain size dependence and solid solution strengthening can be combined in an additive or linear superposition model to accurately predict the yield strength in Mg castings [39,47,96].

This relationship can be further broken down by taking into account the entire grain size distribution. The grain size distribution can be more accurately described as a bi-modal microstructures by using a linear combination of the two grain sizes (in-mold and ESC) and their respective fractions [97]. The skin has been shown to have a significant effect on the mechanical properties [25,50], and as such has been separated into separate components using a composite

model by Yang et al. [51]. The above models for yield strength do not take into account the effects of Mn and fraction of ESCs, requiring further refinement for use in AM series castings.

1.6.2 Ductility

In Mg alloys, with increasing Al content, the ductility is observed to decrease [62–66]. The reasons for this are still not well understood. Predicted limiting factors for ductility are casting defects – including oxide films, shrinkage porosity, and β-phase [24]. This is given in order of the most likely to have a large effect on ductility to least likely [8]. Analytical models for ductility in casting alloys have been investigated and developed for Al and Mg alloys [98–104]. These models tend to center on prediction of ductile void nucleation and growth.

One of the first models for ductility was the Brown-Embury model. Brown and Embury developed a physics based model for the nucleation of voids through a sample, and growth to a critical size which lead to fracture [105]. It was originally published in 1973, and is based on the reduction of area in the necking region of a sample. It is an estimate of true strain to fracture [105]. Jung then modified the Brown-Embury model [106] to derive an analytical model for the tensile ductility, and to modify it to apply to cast materials. The engineering strain at fracture was related to the pore size and mechanical properties of the matrix. This approach was used by Chadha et al. to predict the ductility in die cast AM50 and AM60 as a function of the mean pore size, crack tip radius and overall fraction of porosity [98].

Other work predicting ductility of these alloys is centered on analysis of the fracture surfaces for porosity and other defects. This is theorized by Lee and Gokhale, who examined the variability in ductility of AM50 [104]. It has been observed that ductility has no correlation with bulk porosity, but instead shows a positive relationship with porosity on the fracture surface.

Cracks tended to propagate through pore clusters, indicating that extreme cases determine the tensile properties [104,107]. Research has suggested microporosity has a strong effect on the tensile properties, in particular, Gokhale has investigated the effect of microporosity on the tensile fracture surface and described the results in terms of the load carrying capacity of the cast metal [104,108].

Fracture initiation in castings are predominantly assumed to be a function of the reduced area due to local in-homogeneities in the microstructure, such as oxide films and pores, which are predicted to act as initiation sites for void formation (or fracture) [109]. Weiler et al. determined that local area fraction of porosity in AM60B was the primary factor influencing tensile failure of specimens [110]. It was observed that the fracture path tends to go through pore clusters in AM50 alloys [74,104]. This indicates that the local area fraction of defects on the surface tends to determine the failure behavior. In order to account for local defect fraction, a model was developed by Ghosh to quantify the effect of reduced cross sectional area on strain localization in that area [111]. This was modified by Caceres and Selling to use a simplified constitutive model, and is shown in Equation 1.3 [101].

[1.3] $(1-f)\varepsilon_i^n\, e^{-\varepsilon_i} = \varepsilon_h^n e^{-\varepsilon_h}$

This relates the strain in the reduced area section ε_i to the homogenous strain through a local defect fraction, f, and the strain hardening exponent, n. The strain hardening exponent used is that determined using the Hollomon relationship [112]. By using a constitutive model to relate the microporosity to the stress state and the strain hardening exponent, Lee et al. related the microporosity to the tensile properties [113]. This work does not account for grain size however, which Lee attempts to relate to microporosity, and in turn elongation. Lee et al. found that with increasing grain size, the elongation decreases for a given microporosity level [114], however the

causes for this have not been fully explained. This work has been adapted by Weiler and Wood for use in describing the ductility of AM60. [103] They base their model on work from Ghosh where failure of strain hardening materials occurs due to instabilities at the maximum load, similar to the approach of Lee and Gokhale [111,115] Weiler and Wood have proposed modifications to account for location of the pores on the fracture surface (relative to the specimen surfaces) as well as using the large pore as the predominant failure point [103] The maximum strain to failure occurs when the pore is at the mid-point of the specimen, minimizing surface effects and strain localizations causing failure. They find a correlation between predicted elongations and porosity area fraction as well.

Quality mapping is another approach used to capture the distribution of ductility in larger cast components in Mg and Al alloys [78]. This approach is empirical and used to capture spatial property variation within a casting using highly calibrated casting simulation parameters [78,116,117]. The quality-mapping approach is not physics- based and thus it can be difficult to extrapolate results beyond the range of model calibration. This approach also requires a large quantity of experimental data and detailed casting simulations for calibrating the model parameters [78]. Similarly, numerical modeling has also used to predict and match tensile curves for die cast AM60 alloys [118]. The effect of pores on ductility has also been studied using FEA to model crack propagation paths and effect of skin on the failure mode [119]. However, this replicates experimental results without explaining the mechanisms by which failure occurs. Weak link modeling gives regimes for where different microstructural parameters are dominant. Dominant microstructural features can be determined using the same methods Ceschini et al. used, where statistical correlations between known microstructural parameters and tensile properties were found [120]. Regression techniques can be used to identify the features with strong effects

on the tensile properties, particularly dendrite arm spacing and eutectic particle size in the die cast aluminum alloys. A similar approach can be used in Mg alloys.

1.7 Research Objectives and Approach

The use of die cast Mg alloys in production parts is limited by a poor understanding of the mechanical behavior and the high variability in ductility. The current understanding of the yield strength and ductility is still limited. The current investigation explores the use of alloying and processing to isolate the effects of solute content, eutectic phases, and casting defects on the tensile behavior.

The objectives of this research are to quantify the microstructural features and tensile behavior for a range of aluminum contents and plate thicknesses in ideal high pressure die cast plates. The focus is on using very high quality and well characterized castings and on statistically significant data sets. By quantifying these effects, key factors affecting yield strength, ductility and strain hardening behavior are identified. The effects of β-phase and shrinkage porosity can be isolated using processing techniques. Solution treatment is used to reduce or eliminate the β-$Mg_{17}Al_{12}$ eutectic phase, and HIP to reduce or eliminate shrinkage porosity in the castings. By isolating these features, an analytical model for the yield strength and ductility of these alloys is developed. The model for yield strength is based on linear superposition of the different components of strengthening with an exceptional degree of quantification of the relevant microstructural features. The model for ductility is based on the Ghosh model to determine the efficacy of this approach for describing the observed behavior.

Chapter 2 describes the experimental procedures used in this work. Chapter 3 discusses the effects of aluminum content and thickness on the as cast tensile behavior of the AM alloy series,

and develops a model for yield strength in these alloys. In chapter 4, the effects of alloying and processing on the microstructure and yield strength are quantified. It also extends the analysis to a beyond the AM series alloys, using a wider range of Mg-Al binary alloys. Chapter 5 explores the effects of aluminum content and different microstructural features on the ductility and strain hardening behavior in these alloys. Chapter 6 details the major conclusions from this work and provides recommendations for future work. Chapters 3, 4, and 5 are presented as stand-alone manuscripts as submitted to scientific journals, noted at the start of each chapter.

References

[1] W.J. Joost: *JOM*, 2012, vol. 64, pp. 1032–38.
[2] M.K. Kulekci: *Int. J. Adv. Manuf. Technol.*, 2008, vol. 39, pp. 851–65.
[3] A.A. Luo: *J. Magnes. Alloy.*, 2013, vol. 1, pp. 2–22.
[4] H.E. Friedrich and B.L. Mordike, eds.: *Magnesium Technology: Metallurgy, Design Data, Applications*, Springer, Berlin, 2006.
[5] J.H. Forsmark, J.W. Zindel, L. Godlewski, and A. Caliskan: *SAE Int.*, 2012, pp. 2–10.
[6] E. Aghion, B. Bronfin, Dan Eliezer, F. Von Buch, S. Schumann, and Horst E. Friedrich: *Mater. Sci. Forum*, 2003, vol. 419–422, pp. 407–18.
[7] R. Alain, T. Lawson, P. Katool, G. Wang, J. Jekl, R. Berkmortel, and L. Miller: *SAE Int.*, 2004, pp. 2004-01–0131.
[8] M.A. Easton, T. Abbott, and C.H. Cáceres: *Mater. Sci. Forum*, 2003, vol. 419–422, pp. 147–52.
[9] B.L. Mordike and T. Ebert: *Mater. Sci. Eng. A*, 2001, vol. 302, pp. 37–45.
[10] H.I. Laukli: Norwegian University of Science and Technology, 2004.
[11] M.M. Avedesian and H. Baker, eds.: *ASM Specialty Handbook - Magnesium and Magnesium Alloys*, ASM International, Metals Park, OH, 1999.
[12] Z. Brown, A.A. Luo, M. Musser, L.J. Ouimet, K. Sadayappan, J. Zindel, and R. Beals: *North Am. Die Cast. Assoc. Trans.*, 2009, vol. 13, pp. T09-43.
[13] A.A. Luo and A.K. Sachdev: *Int. J. Met.*, 2010, pp. 51–60.
[14] J. Miao, M. Li, and J.E. Allison: in *Mg2012 9th Int. Conf. Magnes. Alloy. Their Appl.*, 2012, pp. 493–98.
[15] M. Li, R. Zhang, and J.E. Allison: in *Magnes. Technol. 2010*, 2010, pp. 623–27.
[16] Y.N Wang and J.C Huang: *Mater. Chem. Phys.*, 2003, vol. 81, pp. 11–26.
[17] D.H. StJohn, A.K. Dahle, T. Abbott, M.D. Nave, and M. Qian: in *Magnes. Technol. 2003*, 2003, pp. 193–98.
[18] C. Dørum, O.S. Hopperstad, O.G. Lademo, and M. Langseth: *Int. J. Crashworthiness*, 2003, vol. 8, pp. 455–70.
[19] P. Sharifi, Y. Fan, H.B. Anaraki, A. Banerjee, K. Sadayappan, and J.T. Wood: *Metall. Mater. Trans. A*, 2016.
[20] A.V. Nagasekhar, M.A. Easton, and C.H. Cáceres: *Adv. Eng. Mater.*, 2009, vol. 11, pp. 912–19.
[21] D.H. StJohn, M. Qian, M.A. Easton, P. Cao, and Z. Hildebrand: *Metall. Mater. Trans. A*, 2005, vol. 36, pp. 1669–79.
[22] A.V. Nagasekhar, C.H. Cáceres, and M.A. Easton: in *Magnes. Technol. 2010*, 2010, pp. 373–76.
[23] A.L. Bowles, K. Nogita, M.S. Dargusch, and C.J. Davidson: *Mater. Trans*, 2004, vol. 45, pp. 3114–19.
[24] D. Rodrigo, M. T. Murray, and H. Mao: *SAE Int. Congr. Magnes. Sess.*, 1999.
[25] W.P. Sequeira, G.L. Dunlop, and M.T. Murray: in *Proc. Third Int. Magnes. Conf.*, 1996, pp. 63–73.
[26] A. Kielbus, T. Rzychon, and R Cibis: *J. Achiev. Mater. Manuf. Eng.*, 2006, vol. 18, pp. 135–38.
[27] A.K. Dahle, Y.C. Lee, M.D. Nave, P.L. Scha, and D.H. Stjohn: *J. Light Met.*, 2001, vol. 1, pp. 61–72.
[28] D.A. Porter and K.E. Easterling: *Phase Transformations in Metals and Alloys*, CRC Press,

2009.
[29] A. Nayeb-Hashemi: *Phase Diagrams of Binary Magnesium Alloys*, ASM International, Metals Park, 1988.
[30] H. Zhang, S.L. Shang, Y. Wang, A. Saengdeejing, L.Q. Chen, and Z.K. Liu: *Acta Mater.*, 2010, vol. 58, pp. 4012–18.
[31] S. Barbagallo, H.I. Laukli, O. Lohne, and E. Cerri: *J. Alloys Compd.*, 2004, vol. 378, pp. 226–32.
[32] M.S. Dargusch, M. Nave, S.D. McDonald, and D.H. StJohn: *J. Alloys Compd.*, 2010, vol. 492, pp. L64–68.
[33] M.D. Nave, A.K. Dahle, and D.H. StJohn: in *Magnes. Technol. 2000*, H.I. Kaplan, J. Hryn, and B. Clow, eds., The Minerals, Metals & Materials Society, 2000, pp. 233–42.
[34] L.-Y. Wei and R. Warren: *Mater. Sci. Technol.*, 2007, vol. 23, pp. 745–52.
[35] A.V. Nagasekhar, C.H. Cáceres, and C. Kong: *Mater. Charact.*, 2010, vol. 61, pp. 1035–42.
[36] G. Song, A. Atrens, and M.S. Dargusch: *Corros. Sci.*, 1999, vol. 41, pp. 138–62.
[37] D.G. Leo Prakash and Doris Regener: *J. Alloys Compd.*, 2008, vol. 461, pp. 139–46.
[38] R.M. Wang, a. Eliezer, and E.M. Gutman: *Mater. Sci. Eng. A*, 2003, vol. 355, pp. 201–7.
[39] J. Miao, E. Marquis, M. Li, and J.E. Allison: *Metall. Mater. Trans. A*, 2013.
[40] L.-Y. Wei, H. Westengen, T.K. Aune, and D. Albright: in *Magnes. Technol. 2000*, TMS, Warrendale, 2000, pp. 153–60.
[41] A.K. Dahle, S. Sannes, D.H. StJohn, and H. Westengen: *J. Light Met.*, 2001, vol. 1, pp. 99–103.
[42] S. Otarawanna, C.M. Gourlay, H.I. Laukli, and A.K. Dahle: *Mater. Charact.*, 2009, vol. 60, pp. 1432–41.
[43] C.M. Gourlay, H.I. Laukli, and A.K. Dahle: *Metall. Mater. Trans. A*, 2007, vol. 38, pp. 1833–44.
[44] K. Vanna Yang, C.H. Cáceres, and M.A. Easton: *Mater. Sci. Eng. A*, 2013, vol. 580, pp. 355–61.
[45] J.P. Weiler, J.T. Wood, R.J. Klassen, R. Berkmortel, and G. Wang: *Mater. Sci. Eng. A*, 2006, vol. 419, pp. 297–305.
[46] K. Vanna Yang, M.A. Easton, and C.H. Cáceres: *Mater. Sci. Eng. A*, 2013, vol. 580, pp. 191–95.
[47] P. Sharifi, Y. Fan, J.P. Weiler, and J.T. Wood: *J. Alloys Compd.*, 2014.
[48] P. Sharifi, Y. Fan, K. Sadayappan, G. Birsan, and J.T. Wood: in *Magnes. Technol. 2015*, 2015, pp. 351–56.
[49] H.I. Laukli, C.M. Gourlay, and A.K. Dahle: *Metall. Mater. Trans. A Phys. Metall. Mater. Sci.*, 2005, vol. 36, pp. 805–18.
[50] J.H. Forsmark, Z. Dowling, K. Gibson, C. Mueller, L. Godlewski, J.W. Zindel, and J.M. Boileau: *SAE Int. J. Mater. Manuf.*, 2015, vol. 8.
[51] K.V. Yang, C.H. Cáceres, and M.A. Easton: *Metall. Mater. Trans. A*, 2014, vol. 45, pp. 4117–28.
[52] T.D. Berman: Private communication, 2016.
[53] X. Li, S.M. Xiong, and Z. Guo: *J. Mater. Sci. Technol.*, 2016, vol. 32, pp. 54–61.
[54] S. Barbagallo: *Int. J. Cast Met. Res.*, 2004, vol. 17, pp. 364–69.
[55] J. Campbell: in *Complet. Cast. Handb.*, Elsevier Ltd, 2011, pp. 499–597.
[56] S.G. Lee and A.M. Gokhale: *Scr. Mater.*, 2006, vol. 55, pp. 387–90.

[57] J. Campbell: in *Shape Cast. John Campbell Symp.*, 2005, pp. 3–12.
[58] J. Campbell: *Metall. Mater. Trans. B Process Metall. Mater. Process. Sci.*, 2006, vol. 37, pp. 857–63.
[59] M. Tiryakioğlu, J. Campbell, and C. Nyahumwa: *Metall. Mater. Trans. B*, 2011, vol. 42, pp. 1098–1103.
[60] M. Tiryakioğlu: *Mater. Sci. Eng. A*, 2007, vol. 465, pp. 287–89.
[61] J.T. Staley, M. Tiryakioğlu, and J. Campbell: *Mater. Sci. Eng. A*, 2007, vol. 465, pp. 136–45.
[62] T.K. Aune, H. Westengen, and T. Ruden: *SAE Tech.*, 1993, pp. 51–57.
[63] P. Bakke, K. Pettersen, and H. Westengen: *JOM*, 2003, pp. 46–51.
[64] T. Abbott, M.A. Easton, and W. Song: *Mater. Sci. Forum*, 2003, vol. 419–422, pp. 141–46.
[65] T.K. Aune, H. Westengen, and T. Ruden: *SAE Tech.*, 1994, pp. 65–69.
[66] K. Vanna Yang, C.H. Cáceres, A.V. Nagasekhar, and M.A. Easton: *Mater. Sci. Eng. A*, 2012, vol. 542, pp. 49–55.
[67] N. Tahreen, D.L. Chen, M. Nouri, and D.Y. Li: *Mater. Sci. Eng. A*, 2014, vol. 594, pp. 235–45.
[68] C.H. Cáceres and D.M. Rovera: *J. Light Met.*, 2001, vol. 1, pp. 151–56.
[69] C.H. Cáceres, W.J. Poole, A.L. Bowles, and C.J. Davidson: *Mater. Sci. Eng. A*, 2005, vol. 402, pp. 269–77.
[70] M. Wu and S. Xiong: *IOP Conf. Ser. Mater. Sci. Eng.*, 2012, vol. 33, p. 12078.
[71] Y. Ma, J. Zhang, and M. Yang: *J. Alloys Compd.*, 2009, vol. 470, pp. 515–21.
[72] E.I. Barker, K.S. Choi, X. Sun, E. Deda, J. Allison, M. Li, J. Forsmark, J. Zindel, and L. Godlewski: *Comput. Mater. Sci.*, 2014, vol. 92, pp. 353–61.
[73] B. Zhang, A.V. Nagasekhar, X. Tao, Y. Ouyang, C.H. Cáceres, and M.A. Easton: *Mater. Sci. Eng. A*, 2014, vol. 599, pp. 204–11.
[74] J. Song, S. Xiong, M. Li, and J.E. Allison: *J. Alloys Compd.*, 2009, vol. 477, pp. 863–69.
[75] J. Song, S. Xiong, M. Li, and J.E. Allison: *Mater. Sci. Eng. A*, 2009, vol. 520, pp. 197–201.
[76] M. Zhou, N.Y. Li, and H. Hu: *Mater. Sci. Forum*, 2005, vol. 475–479, pp. 463–68.
[77] E. Aghion, N. Moscovitch, and A. Arnon: *Mater. Sci. Eng. A*, 2007, vol. 447, pp. 341–46.
[78] J.H. Forsmark, J.W. Zindel, L. Godlewski, J. Zheng, J.E. Allison, and M. Li: *Integr. Mater. Manuf. Innov.*, 2015, vol. 4.
[79] K. Sadayappan, W. Kasprzak, Z. Brown, L. Ouimet, and A.A. Luo: *Mater. Sci. Forum*, 2009, vol. 618–619, pp. 381–86.
[80] J.F. Nie: *Metall. Mater. Trans. A*, 2012, vol. 43, pp. 3891–3939.
[81] L. Han, H. Hu, and D. Northwood: in *Magnes. Technol. 2008*, TMS, 2008, pp. 361–64.
[82] T. Zhu, Z.W. Chan, and W. Gao: *J. Mater. Eng. Perform.*, 2010, vol. 19, pp. 860–67.
[83] L. Yang, Y. Wei, and L. Hou: *J. Mater. Sci.*, 2010, vol. 45, pp. 3626–34.
[84] Th. Schubert, P. Kumar, and B. Kieback: in *Mg2012 9th Int. Conf. Magnes. Alloy. Their Appl.*, 2012, pp. 1223–28.
[85] J.T. Staley, M. Tiryakioğlu, and J. Campbell: *Mater. Sci. Eng. A*, 2007, vol. 460–461, pp. 324–34.
[86] M. Ostermeier, M. Brummer, and E. Werner: *Int. Foundry Res.*, 2009, vol. 61, pp. 2–7.
[87] M. Ostermeier: Technischen Universität München, 2009.
[88] E. Aghion, B. Bronfin, and D. Eliezer: *J. Mater. Process. Technol.*, 2001, vol. 117,

pp. 381–85.
[89] D. M. Stefanescu: *Int. J. Cast Met. Res.*, 2005, vol. 18, pp. 129–43.
[90] J.E. Allison, D. Backman, and L. Christodoulou: *J. Mater.*, 2006, pp. 25–27.
[91] J.E. Allison, B. Liu, K.P. Boyle, L. Hector Jr., and R.C. McCune: in *Magnes. Technol. 2010*, 2010, pp. 35–40.
[92] E.O. Hall: *Proc. Phys. Soc. A*, 1951, vol. 64, pp. 747–53.
[93] N.J. Petch: *J. Iron Steel Inst.*, 1953, vol. 174, pp. 25–28.
[94] J.A. Yasi, L.G. Hector, and D.R. Trinkle: *Acta Mater.*, 2010, vol. 58, pp. 5704–13.
[95] P. Lukáč and Z. Trojanová: *Mater. Eng.*, 2011, vol. 18, pp. 110–14.
[96] I. Toda-Caraballo, E.I. Galindo-Nava, and P.E.J. Rivera-Díaz-del-Castillo: *Acta Mater.*, 2014, vol. 75, pp. 287–96.
[97] K.J. Kurzydlowski and J.J. Bucki: *Acta Metall. Mater.*, 1993, vol. 41, pp. 3141–46.
[98] G. Chadha, J.E. Allison, and J.W. Jones: *Metall. Mater. Trans. A*, 2007, vol. 38, pp. 286–97.
[99] C.D. Lee and K.S. Shin: *Mater. Sci. Eng. A*, 2014, vol. 599, pp. 223–32.
[100] C.D. Lee, T.I. So, and K.S. Shin: *Mater. Sci. Eng. A*, 2014, vol. 599, pp. 28–37.
[101] C.H. Cáceres and B.I. Selling: *Mater. Sci. Eng. A*, 1996, vol. 220, pp. 109–16.
[102] J.P. Weiler and J.T. Wood: *Mater. Sci. Eng. A*, 2009, vol. 527, pp. 25–31.
[103] J.P. Weiler and J.T. Wood: *J. Alloys Compd.*, 2012, vol. 537, pp. 133–40.
[104] S.G. Lee, G.R. Patel, A.M. Gokhale, A. Sreeranganathan, and M.F. Horstemeyer: *Scr. Mater.*, 2005, vol. 53, pp. 851–56.
[105] L.M. Brown and J.D. Embury: in *Proc. Third Int. Conf. Microstruct. Des. Alloy.*, 1973, pp. 164–69.
[106] J. Y. Jung: *Philos. Mag. A*, 2002, vol. 82, pp. 2263–68.
[107] X. Li, S.M. Xiong, and Z. Guo: *Mater. Sci. Eng. A*, 2015, vol. 633, pp. 35–41.
[108] A.M. Gokhale and G.R. Patel: *Mater. Charact.*, 2005, vol. 54, pp. 13–20.
[109] J. Campbell: *Castings*, 3rd ed., Butterworth-Heineman, Oxford, 1991.
[110] J.P. Weiler, J.T. Wood, R.J. Klassen, E. Maire, R. Berkmortel, and G. Wang: *Mater. Sci. Eng. A*, 2005, vol. 395, pp. 315–22.
[111] A.K. Ghosh: *Acta Metall.*, 1977, vol. 25, pp. 1413–24.
[112] J. H. Hollomon: *Trans. Am. Inst. Mining, Metall. Pet. Eng.*, 1945, vol. 162, pp. 268–89.
[113] C.D. Lee: *J. Mater. Sci.*, 2007, vol. 42, pp. 10032–39.
[114] C.D. Lee: *Mater. Sci. Eng. A*, 2007, vol. 454–455, pp. 575–80.
[115] A Gokhale: in *Magnes. Technol. 2001*, 2001, pp. 195–99.
[116] S. Sannes, H. Gjestland, and H. Westengen: *SAE Tech. Pap. Ser.*, 2005, vol. 2005-01–03, p. 7.
[117] U. Weiss and A. Bach: *La Metall. Ital.*, 2011, vol. 11–12, pp. 31–39.
[118] C. Dørum, O.S. Hopperstad, T. Berstad, and D. Dispinar: *Eng. Fract. Mech.*, 2009, vol. 76, pp. 2232–48.
[119] K.S. Choi, D. Li, X. Sun, M. Li, and J.E. Allison: *SAE Int.*, 2013, pp. 3–10.
[120] L. Ceschini, Alessandro Morri, Andrea Morri, and G. Pivetti: *Mater. Des.*, 2011, vol. 32, pp. 1367–75.
[121] E.J. Vinarcik: *High Integrity Die Casting Processes*, John Wiley & Sons, Inc., New York, NY, 2002.

Figures

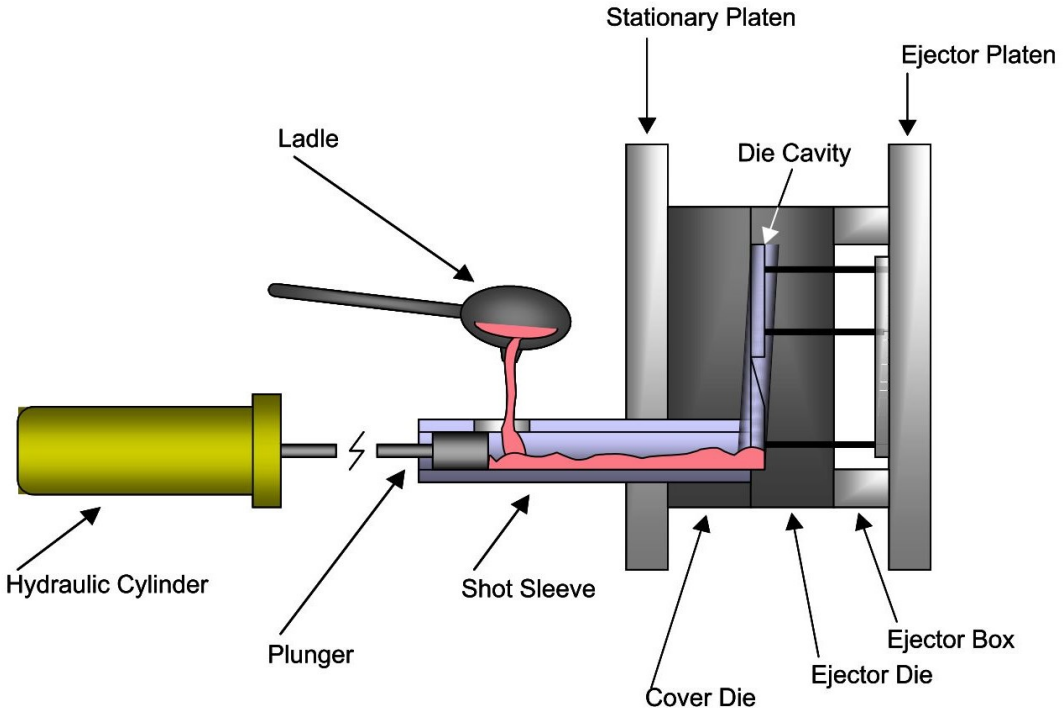

Figure 1.1: Schematic of the cold chamber high pressure die casting process *[121]*

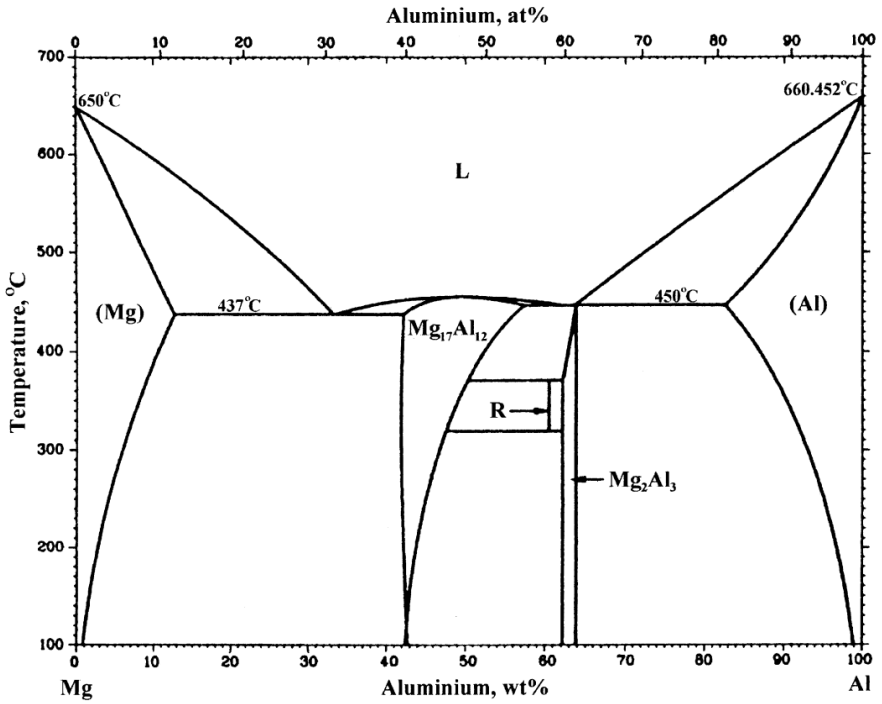

Figure 1.2: Mg-Al phase diagram, as adapted from *[11,27]*

Chapter 2

Experimental Approach

This chapter presents the experimental procedures used to produce and quantify the microstructure and mechanical behavior of these materials. The super vacuum die casting (SVDC) process is described, as well as further processing techniques used to isolate different microstructural features in the castings. The techniques used to quantify the microstructural features and the mechanical behavior are described.

2.1 Material Production and Processing

Magnesium-Aluminum-Manganese plates were SVDC by Ford Research and Innovation Center at MagTech Corporation using a Prince 836 HPDC machine with a Binary IIM shot system, and an additional vacuum pump. Plates are of dimensions 12“x5”, and were cast in two thicknesses, 2.5 and 5mm, and four aluminum contents. The plate geometry is shown in Figure 2.1, where the metal flows in through the top, and exits through the outlet at the bottom of the image. The plates had a nominally constant manganese fraction of 0.45 wt.%. These plates will be referred to as AM40, AM50, AM60 and AM70, where the compositions are detailed in Table 2.1, as determined by Optical Emissions Spectroscopy (OES) at Ford Research and Innovation Center. The target melt temperature was 675°C, and sulfur hexafluoride, SF_6, was used as the cover gas for the molten metal to prevent oxidation. The metal was transferred to the shot sleeve using a

Metamag auger type pump. A vacuum was applied to minimize porosity in the die using Busch 2 stage vacuum pump, reaching 15 mb at the pump inlet, and is likely higher in the die cavity. The additional vacuum pump results in lower observed gas entrapment in the parts, as compared to typical high pressure die cast components. In addition, binary Mg-Al plates were also cast using this procedure at MagTech. The compositions are also listed in Table 2.1.

Solution heat treatment (ST) and hot isostatic pressing (HIP) were used to isolate various microstructural features in the AM series plates. Solution heat treatment was conducted in a Carbolite open-air box furnace for 2.25 hours at 413°C. Temperature was monitored every 10 seconds using a J-type thermocouple embedded in a sample, accurate to ± 2°C. Solution treated samples were water quenched.

HIP was completed at Bodycote in Princeton, KY in a 17" diameter chamber. Plates were processed for 2.25 hours at 410°C and 100 MPa. An Ar cover gas was used to achieve pressure at temperature without oxidation. Plates were laid flat for processing in order to prevent creep and distortion during heating and cooling processes. Temperature was measured using thermocouples placed radially and vertically in the chamber. Plates were slowly cooled due to the depressurization process of the chamber used for HIP.

2.2 Microstructural Characterization

Optical microscopy and scanning electron microscopy (SEM) were used to quantify the microstructure of each condition. The sample preparation and analysis techniques are detailed in this section.

2.2.1 Sample Preparation

Metallographic specimens were mounted using Lapmaster slow cure epoxy resin in 1.25" diameter mounts. Specimens were prepared using a Buehler Ecomet 250 with the following settings: 150 RPM base speed, 60 RPM head speed in complementary rotation, at 25N force. Samples were polished to 1 μm final finish. In order to avoid oxidation effects, no water is used once the polishing procedure is started, and samples are prepared immediately prior to examination. In order to best reveal the grain structure and β-$Mg_{17}Al_{12}$, metallographic samples were etched for 3-5 s in a 5°C solution composed of 60 mL ethanol, 20 mL water, 15 mL glacial acetic acid, and 5 mL nitric acid. This solution is referred to as the acetic nitric etchant.

2.2.2 Optical Microscopy

Optical microscopy was completed using a Zeiss AXIO X2 inverted microscope equipped with a digital camera.

2.2.3 Scanning Electron Microscopy

SEM examination was completed with a Philips XL30 Field Emission Gun (FEG) SEM and a Tescan Mira 3 FEG microscope. Both microscopes are equipped with a backscatter electron (BSE) detector, an EDAX energy dispersive spectroscopy (EDS) detector, and an EDAX electron backscatter diffraction (EBSD) camera. EDAX TSL OIM data collection and analysis software was used on both microscopes. Each of these detectors was used to characterize different microstructural features.

Volume fraction of microstructural features

The volume fraction of porosity was determined using the BSE images on as polished specimens. Typical operating conditions were an accelerating voltage of 30 keV and a working distance of 15-20mm. At least 5 images per condition were used, comprising an area of 3 mm^2.

The volume fraction of the β phase was determined using the BSE images on the XL30 FEG SEM, and secondary electron (SE) images on the Tescan Mira SEM. Both images give similar results after processing. Images were thresholded using a script developed in MATLAB. Images were processed in MATLAB using smoothing functions to normalize the brightness and contrast for all images, and to remove effects from charging at pore boundaries. At least 10 images in a given location were used to determine the average area fraction of β phase. Images were taken in the within 300 μm of the casting surface, and in the center of the casting. An example of the thresholding process is shown in Figure 2.2.

Grain size quantification using Electron Backscatter Diffraction (EBSD)

Grain size was quantified through electron backscatter diffraction (EBSD). For EBSD orientation imaging maps (OIM), a step size of 0.5 μm and a scan area comprised of at least 1000 grains were used. General operating conditions for EBSD were a 20mm working distance, an accelerating voltage of 30 keV, and a beam intensity of 18. The general digital image processing (cleaning) procedure applied to the maps was (1) neighbor orientation correlation, (2) single iteration of grain dilation, and (3) grain confidence index (CI) standardization. After cleaning, only points with a CI > 0.1 were retained. Low confidence points appear black in the EBSD maps, indicating regions of secondary phases, grain boundaries, oxide films, or porosity. The minimum grain size retained after cleaning was set to 3 μm grain diameter.

The grain size distribution for each location and condition were found using the EBSD data. After the cleaning procedure, the minimum grain size was set to be at least 10 points, and to contain multiple rows. A misorientation of greater than 5° was used to define a boundary. The grain file was exported from the OIM analysis software, and analyzed in MATLAB for area average grain diameter, ESC area average, and area fraction of each type of grain. Operationally,

ESCs are defined as α-Mg grains that are greater than 30 μm in diameter. At least 500 grains for each location were used to generate the grain size distribution plots.

2.2.4 X-Ray Diffraction (XRD)

Secondary phase identification and quantification from SEM was validated using x-ray diffraction (XRD). A Rigaku rotating anode Cu k-α x-ray diffractometer was used in the scanning θ - 2θ mode. Bragg peaks were determined between 30° and 45°, with a resolution of 0.05° and a rate of 0.5°/min. Data was analyzed using MDI Jade to complete whole pattern fitting using ICD crystal database reference spectra for pure Mg and β-$Mg_{17}Al_{12}$ phases to quantify the phase fraction of the β-$Mg_{17}Al_{12}$ phase.

2.2.5 Electron Probe Microanalysis (EPMA)

Electron Probe Microanalysis (EPMA) was used to determine through-thickness composition, and was contributed by Dr. Tracy Berman. EPMA was performed using a Cameca SX-100 electron microprobe equipped with wavelength-dispersive spectrometers. The accelerating voltage and beam current were 15 kV and 10 nA, respectively. Standards of at least 99.9% pure Al, Mg, and Mn were used for calibration. Compositions are given as the average of at least 200-point measurements. Further details on the instrument settings and data analysis are reported in Berman et al. [1].

2.3 Mechanical Testing

In order to characterize the mechanical behavior of these alloys, three types of mechanical tests were used. These were tensile, microtensile, and microhardness tests.

2.3.1 Tensile Testing

Tensile specimens with a gauge length of 25.4 mm and a width of 6.4 mm were machined from the as cast plates in accordance to ASTM E8/B557. The specimen design is shown in Figure 2.3. The specimen thickness was equal to the plate thickness, nominally 2.5 or 5mm. Tensile testing was completed for at least 28 samples per condition, with ten tensile bars machined from each plate in the direction of metal flow, at least 12 mm from the plate edge, shown in Figure 2.4. Tensile testing was conducted on a hydraulic MTS load frame with a 25mm extensometer at room temperature. Tests were conducted at an initial strain rate of $10^{-3}\ s^{-1}$, and a constant displacement rate of 2 mm/min until specimen failure. These tests were used to analyze yield strength, ductility, and strain hardening exponent. Yield strength was calculated using the 0.2% offset method.

2.3.2 Microtensile testing

Microtensile testing was conducted on the Kammrath and Weiss tensile stage shown in Figure 2.5. A nominal strain rate of 5 x 10^{-4} s^{-1}, at a constant displacement of 0.6 mm/min (10 μm/sec) was used for all samples. Load was monitored using a 5 kN load cell, and displacement with an LVDT sensor with a resolution of 1 μm. Strain was approximated using the bulk displacement measured using the LVDT. Dogbone-shaped samples were cut to the dimensions shown in Figure 2.6 with Electrical Discharge Machining (EDM) from the center of the plates, parallel to the flow direction of the plates. Samples had a nominal gauge length of 18 mm and width of 4.4 mm. These samples were then wired into slices approximately 800 μm thick through the thickness of the plate as shown in Figure 2.6, along the dashed lines. Samples were polished to a final thickness between 300 and 500 μm with a 1 μm mirror finish on one side. If samples were considered skin, the surface of the casting was left in the as cast condition, with no machining

or polishing. If samples were from the core of the plate, one side was ground to 1200 grit SiC using the procedure defined in Appendix A.

Interrupted testing was also used with the stage in-situ in the Tescan SEM. Samples were tested after etching for 4 seconds using acetic nitric etchant to reveal grain structure and secondary phases. Loading was interrupted at pre-determined nominal strains of 1%, 2%, 4%, 8%, in increments of 4% as needed beyond. Images were taken at specific locations to observe any microstructural changes. Fracture surfaces were imaged to identify any trends for failure in the microstructure.

2.3.3 Hardness testing

Vickers microhardness testing was completed at Ford Research and Innovation Center on a LECO AMH 43 automated microhardness system. Testing was completed on AM40 and AM70 aluminum content alloys for the as cast condition, and in addition, AM70 for the solution treated, and HIP conditions. Indents were made at 50 grams force with a dwell time of 13 seconds. Indents were made at a spacing of 100 μm through the thickness of the plate. Column spacing was 100-200 μm depending on the size on the sample, accounting for at least 5mm across the sample.

Bibliography

[1] T.D. Berman: University of Michigan, Ann Arbor, MI, unpublished research, 2016.

Composition	AM40	AM50	AM60	AM70	Mg-3Al	Mg-5Al	Mg-9Al	Mg-12Al
Al (Wt. %)	3.8	4.6	6.0	7.0	3.12	4.8	8.99	11.35
Mn (Wt.%)	0.55	0.4	0.44	0.44	0.09	0.09	0.11	0.10
Zn (Wt.%)	0	0	0	0	0.06	0.06	0.05	0.11

Table 2.1: Aluminum and manganese compositions for each AM series and binary composition as measured by optical emission spectroscopy

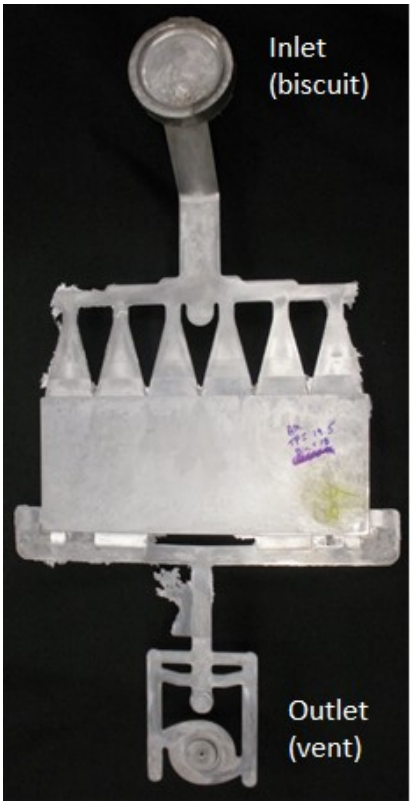

Figure 2.1: Plate casting geometry, where the metal enters the die at the top, and exits at the bottom. This includes the biscuit and vacuum structure.

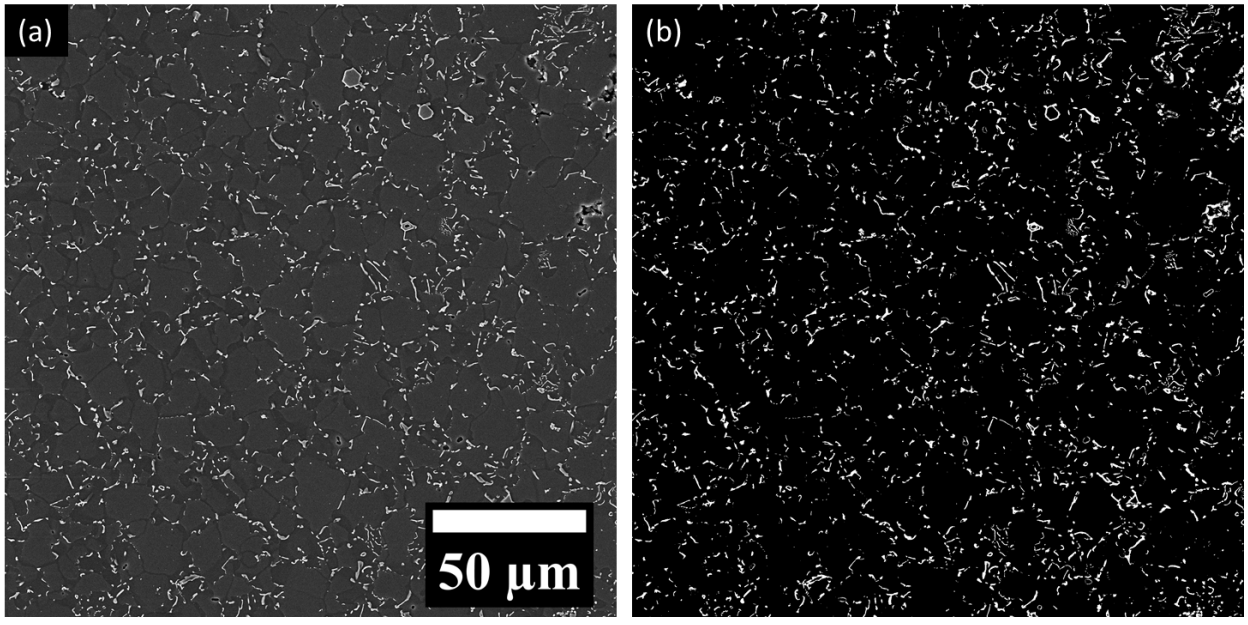

Figure 2.2: (a) SE image used for determination of eutectic phase volume fraction in different regions. This particular image is from the near edge of the AM70 2.5mm HIP condition. (b) Image resulting from the thresholding process such that the eutectic phases are

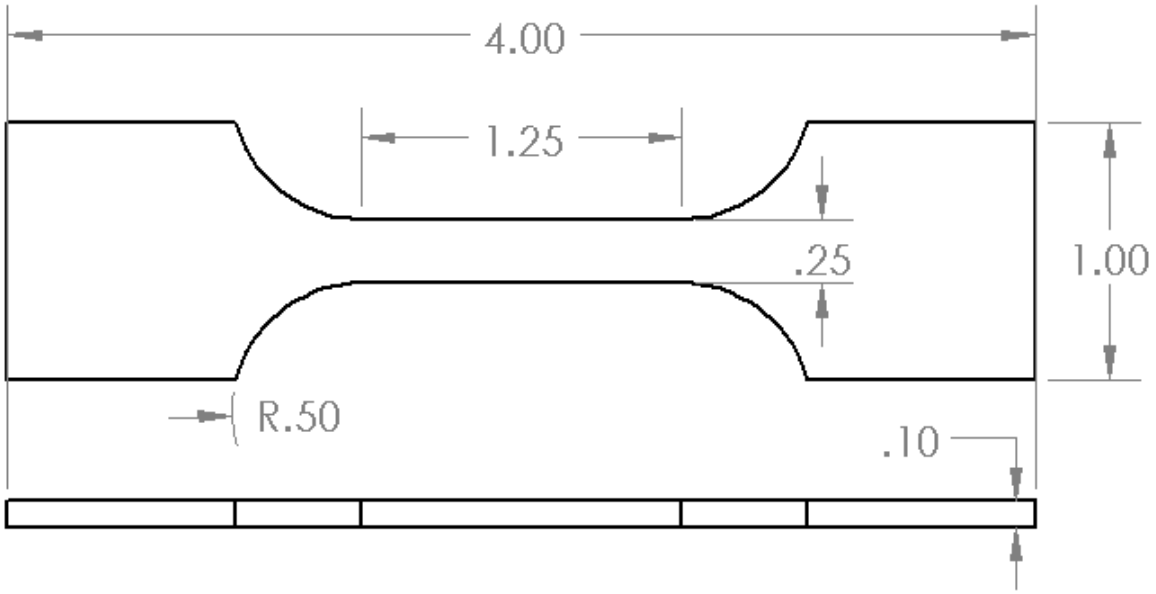

Figure 2.3: Bulk tensile dimensions given in inches, shown for the 2.5mm (0.10”) thick plate.

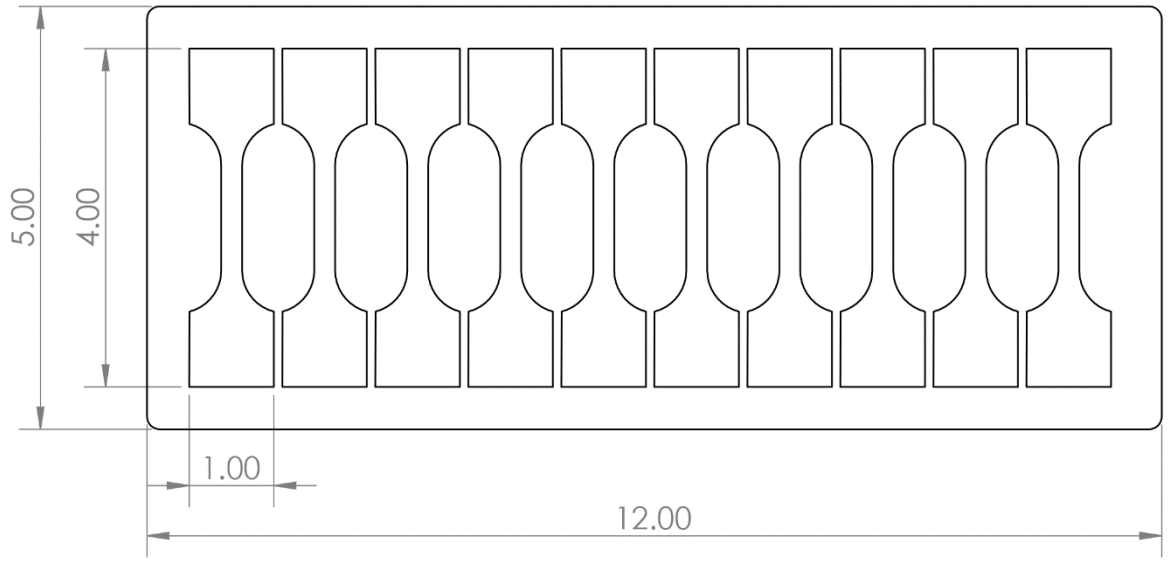

Figure 2.4: Layout of the tensile sample locations from each plate, where the casting flow direction is along the vertical axis.

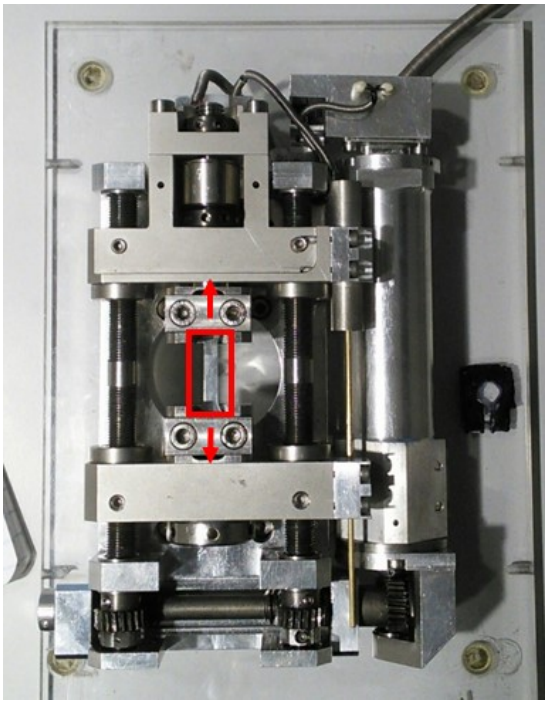

Figure 2.5: Kammrath and Weiss load frame used for microtensile experiments, using a 5 kN load cell. Sample and loading direction are marked.

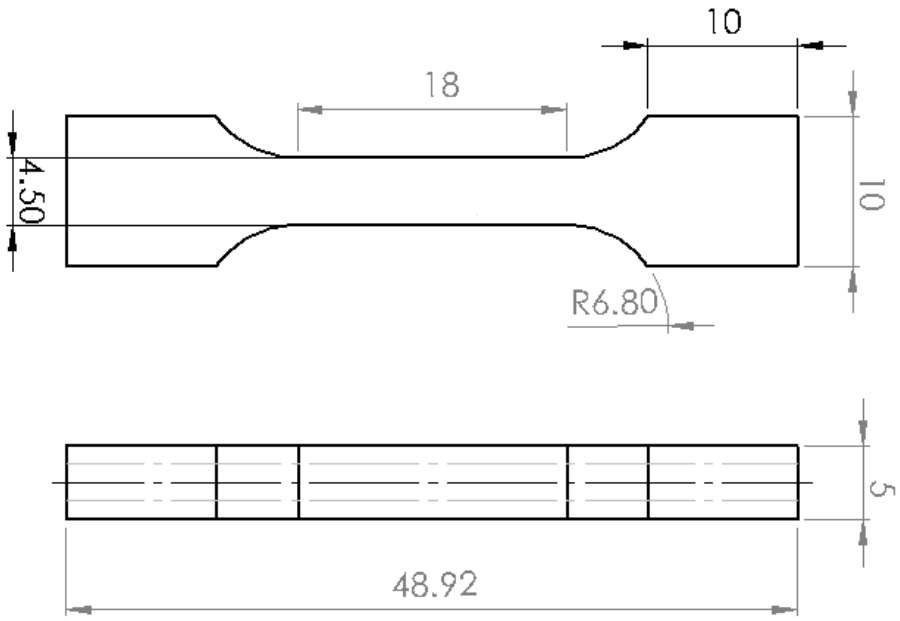

Figure 2.6: Microtensile sample dimensions as machined, with dimensions given in mm. Top layout is as machined for the 2.5 and 5mm plates. Bottom shows the through thickness slices of approximately 800 µm thick using dashed lines. Microtensile samples are cut from the center of the plate along the flow direction.

Chapter 3

The influence of Al content and thickness on the microstructure and tensile properties in high pressure die cast magnesium alloys

Abstract

The influence of Al content and section thickness on the microstructural features and tensile properties of high pressure die cast AM series magnesium alloys is quantified in order to better understand the relationship between microstructure and tensile properties. It is found that with increasing aluminum content, the yield strength increases and the ductility decreases. Increasing the plate thickness results in a decrease in both the yield strength and ductility. The grain size, β-$Mg_{17}Al_{12}$ phase volume fraction, and solute content are all quantified through the thickness of the plates. It is found that the plates have a skin with increased hardness, due to a fine grain structure. The primary factors affecting strengthening in these alloys, including microstructural variations through the thickness, is accounted for using a linear superposition model. We conclude that yield strength is dominated by grain boundary strengthening and solid solution strengthening effects. The through-thickness grain size and solute concentration were quantified and these variations were found to play an important role in controlling the yield strength of these alloys.

3.1 Introduction

Due to their high specific strength and good castability, magnesium alloys are desirable for use in weight reduction strategies for automotive applications [1,2]. Over 95% of magnesium parts for structural applications are manufactured using the high pressure die casting process [3,4]. High pressure die casting (HPDC) allows large, thin-walled components to be mass-produced rapidly and economically. In HPDC, highly turbulent molten metal flows into the shaped die cavity, generating a broad distribution of microstructures through the thickness and in different regions of a single casting [5,6]. The heterogeneity observed in the microstructure of cast components leads to increased variability in the observed tensile properties as shown by Forsmark et al. [7].

The use of magnesium alloy die castings is limited partially by the variability in mechanical properties observed in HPDC components [8]. This variability necessitates conservatively designed HPDC parts and limits the ability to use HPDC components in crash sensitive applications where ductility and deformation behavior are especially important. It is commonly believed that these properties, particularly the ductility, strongly depend on porosity levels [9–11]. For this reason, super vacuum die casting (SVDC) technology is being explored to minimize the presence of gas porosity and in turn, improve the mechanical properties [3]. To take full advantage of the property improvements provided by SVDC, there is a need for improved predictability of properties.

In order to better predict location dependent properties in castings, integrated computational materials engineering (ICME) approaches are under development [12]. Currently, two approaches exist to capture and reduce variations in properties – “quality mapping” statistical approaches and deterministic physics-based structure-property relationships. Quality mapping is an empirical approach currently used to capture spatial property variation within a casting using

highly calibrated parameters [13–15]. Since the quality-mapping approach is not physics- based it can be difficult to extrapolate results beyond the range of model calibration. This approach also requires a large quantity of experimental data. Thus further study of the fundamental effects of microstructure on the tensile properties is needed to develop physics-based models for use in more refined ICME tools. Recently, deterministic yield strength models have been developed by Yang et al., Sharifi et al., and Toda-Carabello et al. [16–18]. These models incorporate known strengthening mechanisms, specifically grain boundary, solid solution, and dispersion strengthening, but use different methods to calculate each strength component [19].

To better understand the mechanical properties, it is important to understand both intrinsic and extrinsic microstructural features throughout the entire casting [20]. Intrinsic microstructural features are those that are related to the composition of the alloy, such as composition variation and formation of eutectic phases. Extrinsic features are those that are related to the manufacturing process. These features are produced and controlled by the casting process, including shrinkage- and micro-porosity, inhomogeneous microstructures (e.g., externally solidified crystals), casting defects (e.g., oxide films, hot tearing), and the development of skin and core microstructures. Of particular importance is the occurrence of externally solidified crystals (ESCs) in the core, which are coarse, dendritic grains that solidify before entering the die cavity.

Tensile properties appear to be a function of a hierarchy of effects from the different microstructural features. For example, there is an observed dependence of the mechanical behavior on intrinsic features due to alloying effects as observed by Aune [21]. The most deleterious features tend to be oxide films and large pores which result in a significant reduction of the ductility [22], while β-$Mg_{17}Al_{12}$ volume fraction and morphology is likely to only have a minor impact on mechanical properties [23]. Characterizing critical microstructural features as inputs

to current and future models for the tensile properties is an important step to refining prediction of the yield strength and in the future, ductility.

In this study, we quantify the influence of Al content and plate thickness on the microstructural features and tensile properties of a series of SVDC aluminum-manganese (AM-type) magnesium alloys. SVDC was used to reduce the influence of extrinsic microstructural feature such as entrapped gas porosity. These results are used to evaluate the efficacy of an improved analytical model for strength. The results from this investigation were designed as inputs to parallel investigations using crystal plasticity and continuum mechanics simulations of microstructural influences on the ductility [11,24,25].

3.2 Experimental

Mg-Al-Mn alloy (AM series magnesium alloys) plates were super vacuum die cast by Ford Research and Innovation Center at MagTech Corporation. Plates of nominal dimensions 305mm x 130mm (12-inch x 5-inch) were cast in two thicknesses, 2.5 and 5mm, and four Al alloy compositions with a nominally constant Mn content as detailed in Table 3.1. These will be referred to as AM40, AM50, AM60, and AM70, respectively. The composition of the melt was determined by Optical Emissions Spectroscopy (OES) at Ford Research and Innovation Center, and will be referred to as the alloy composition. The target melt temperature was 948 K (675℃). Sulfur hexafluoride, SF_6, was used as the cover gas to prevent oxidation.

Tensile specimens with a gage length of 25.4 mm and a width of 6.4 mm were machined from the as-cast plates in accordance to ASTM E8/B557. The specimen thickness was equal to the plate thickness, 2.5 or 5mm. Tensile testing was completed for 18 samples per condition, with nine

tensile bars machined from each plate, at least 12 mm from the plate edge. Tensile testing was conducted on a hydraulic MTS load frame with a 25mm extensometer at room temperature. Tests were conducted at an initial strain rate of 1 x 10^{-3} s^{-1}, and a constant displacement rate of 2 mm/min until sample failure. These tests were used to analyze yield strength, ductility, and strain hardening exponent. Yield strength was calculated using the 0.2% offset method.

Metallographic samples were sectioned from the grip section of the tensile bars, and characterized for porosity, β-$Mg_{17}Al_{12}$, and grain size. Samples were prepared using standard techniques, with a final polish using 1 μm diamond paste. Buehler MetaDi fluid was used as a polishing lubricant in place of water. To characterize grain size, samples were etched for 3 seconds in a 278 K (5℃) acetic nitric solution (5 mL nitric acid, 15 mL glacial acetic acid, 20 mL water, 60 mL ethanol).

Microhardness mapping was completed using an automated Vickers microhardness system with a load of 50 grams force and a dwell time of 13 seconds. Based on previous work by Yang et al. [26], in accordance with ASTM E384 standard, the spacing between measurements should be at least 2.5 times the length of the indentation diagonal. For these samples, indents were placed using a 100 μm spacing through the casting thickness.

The nominal area fraction of porosity was quantified using backscatter electron (BSE) SEM images. The nominal area fraction of porosity was determined using at least 10 images. The area fraction of β-$Mg_{17}Al_{12}$ was quantified using both image analysis of BSE SEM images and x-ray diffraction (XRD). β-$Mg_{17}Al_{12}$ phase fraction and distribution were quantified on as-polished specimens. XRD was conducted on polished, through thickness specimens placed in a Rigaku Rotating Anode X-Ray Diffractometer.

Electron Probe Microanalysis (EPMA) was used to determine through-thickness composition. EPMA was performed using a Cameca SX-100 electron microprobe equipped with wavelength-dispersive spectrometers. The accelerating voltage and beam current were 15 kV and 10 nA, respectively. Standards of at least 99.9% pure Al, Mg, and Mn were used for calibration. Compositions are given as the average of at least 200-point measurements. Further details on the instrument settings and data analysis are reported in Berman et al. [27].

Grain size was quantified through electron backscatter diffraction (EBSD). For EBSD orientation imaging maps (OIM), a step size of 0.5 um and a scan area comprised of at least 1000 grains were used. The general digital image processing (cleaning) procedure applied to the maps was (1) neighbor orientation correlation, (2) single iteration of grain dilation, and (3) grain confidence index (CI) standardization. After cleaning, only points with a CI > 0.1 were retained. Low confidence points appear black in the EBSD maps, indicating regions of secondary phases, grain boundaries, oxide films, or porosity. The minimum grain size retained after cleaning was set to 3 μm grain diameter. All experimental data, including tensile data and reference images, is archived for future use on the Materials Commons, an information repository maintained by University of Michigan [28,29].

3.3 Results

3.3.1 Microstructural Characterization

The microstructure of the HPDC plates consists of fine, in-mold α-Mg cells (darker grey), large α-Mg externally solidified crystals (ESCs), β-$Mg_{17}Al_{12}$ eutectic particles (light grey) and AlMn intermetallics (white), shown for each condition in Figure 3.1. The exact composition of the AlMn intermetallic phases is not determined in this work, but can be of the form Al_8Mn_5,

$AlMn_4$, and $Al_{11}Mn_4$ as predicted by ThermoCalc using the TCMG4 database, and by previous work in AM series alloys [30,31]. Examples of ESCs (large, dendritic structures in the core of the castings) are circled in Figure 3.2, which is a cross-section of a cast plate in the etched condition. Shrinkage porosity can be observed approximately 600 μm from the casting surface. Microstructural characterization of in-mold grain size, ESC size, ESC area fraction, eutectic phase β-$Mg_{17}Al_{12}$, and casting defects was completed for all conditions, and in multiple regions through the thickness of the plates. Quantitative microstructural characteristics are tabulated in Table 3.2, with the mean and standard deviation given for each characteristic.

Grain Size

An important microstructural feature in die cast alloys is the variation in grain size that can be observed through the thickness of the casting. Grains are divided into two groups: grains that are formed in the die, termed in-mold α-Mg grains and externally solidified grains or crystals (ESCs) that formed in the shot sleeve before being injected into the die. Cast plates show two distinct regions, hereafter referred to as the skin and the core, shown in Figure 3.3, for a) 2.5mm AM50 and b) 5mm AM50. The skin is the fine grained region adjacent to the casting surface, and the core is the bulk of the material in the center through thickness. To determine the average in-mold grain diameter, EBSD data was partitioned to include only grains less than 30 μm in diameter. The in-mold α-Mg grain size is independent of Al content and thickness, and averages between 12-20 μm in grain diameter as shown in Figure 3.4. The in-mold α-Mg grain size did not vary through the thickness; grains near the casting surface and in the core have the same average in-mold grain diameter. When comparing the in-mold grain size area fraction histograms for all Al contents in the skin and core, the histograms have the same peak value and distribution. Thus the in-mold grain size is considered the same for all plates.

The precise characteristics of ESCs are difficult to quantify and include solute (Al) content, fractal geometry and size. Operationally in this investigation, ESCs were defined as α-Mg grains which are greater than 30 μm in diameter [32]. ESC size can vary up to an order of magnitude, ranging from the operational minimum of 30 μm up to approximately 300 μm in diameter. The area average ESC size is approximately 50-80 μm in diameter. Values for the average ESC size and area fraction are given in Table 3.2. The area average ESC size for all eight conditions is similar, despite the wide range of ESC sizes that were observed. The area fraction of ESCs did depend on location through the thickness, with a higher fraction observed in the core regions of the castings.

Based on the consistent in-mold and ESC grain sizes shown in Table 3.2, the grain size data for all aluminum contents of each thickness are compiled into one data set for each location (skin or core), and an area average in-mold grain size, ESC size and area fraction for the skin and the core of each plate thickness is found. The area fraction grain size distribution for all grains in the skin and in the core is shown in Figure 3.5. Figure 3.5 shows that the area fraction of ESCS is higher in the core than in the skin. The ESCs in the core are surrounded by the fine in-mold α-Mg grains. The in-mold grain size in the core is slightly larger than in the skin, but the in-mold grains occupy a much smaller fraction of the area. The measured area fraction of ESCs in the core was determined to be approximately 45% of the area of the core, with values ranging from 30 to 60% of the area. This was the same for both the 2.5 and 5mm thick plates. Very few ESCs were observed in the near surface region in the 2.5mm plates, but large grains (ESCs) were frequently observed in the near surface region of the 5mm plates, leading to the weakened in-mold peak for the skin region of the 5mm plates. A decrease in peak height is reflective of a decrease in the total area fraction of grains of a given size, in this case the in-mold grains in the skin of the 5mm plates. This

was dependent on sampling location along the edge of the casting, but typically ranged from 30-45% area fraction.

Using the through thickness EBSD scans shown in Figure 3.3, the grain size data is partitioned into bins 50 μm wide. There is a homogeneous fine grain size observed in the skin region of the 2.5mm plates. Grains greater than 30 μm in diameter first occur at a distance of approximately 600 μm from the casting surface in the 2.5mm plates. The through thickness microstructure in the 5mm plates is more complex and there is significant plate-to-plate variability although casting conditions remained constant. The microstructure in the 5mm thick plates typically formed with three distinct bands of grains. Immediately beneath the casting surface, bands of large α-Mg grains were frequently observed. Adjacent to this layer, a region of fine grains, and then in the core of the casting, ESCs were observed. An example of this is seen in Figure 3.3(b). The area fraction of grains greater than 30 μm observed at the surface was 20% for the 5mm plates, while no ESCs were observed in skin of the 2.5mm plates.

Factors affected by aluminum content

The aluminum and manganese content was quantitatively characterized in both the skin and core regions for all four alloys using EPMA. The skin content was measured in a region ~200 to 400 μm from the casting surface and the core content was measured at mid-thickness. As the electron interaction volume is of comparable size (~4 μm) to the in-mold grain diameter (12-20 μm), it is difficult to isolate only the solute content of the matrix for the in-mold grains. For the purposes of this work, the concentration of solute in solid solution is approximated as the mean of all composition measurements. For this set of castings, it is observed that as the Al alloy composition increases, the Mn content of the solid solution decreased, as shown in Figure 3.6.

The primary eutectic phase in AM series alloys is the β-$Mg_{17}Al_{12}$ phase. The β-phase fraction was quantified using both XRD and SEM. Using XRD, the overall β-$Mg_{17}Al_{12}$ phase fraction was determined by measuring relative peak intensity between the α- and β- phases. The intensity of the β-$Mg_{17}Al_{12}$ peaks increased with increasing Al in the alloy, indicating an increase in the phase fraction. The average (through-thickness) β-phase volume fraction measurements from SEM BSE image analysis were very similar values to XRD measurements as shown in Figure 3.7. As expected, increasing Al alloy content, led to an increase in the amount of β-phase. Higher volume fractions of β-phase were measured in the 2.5mm plates when compared to the 5mm plates as shown in Figure 3.7 and in Table 3.2. The amount of β-phase as measured using BSE imaging, was observed to vary through the thickness of the plate. The skin is observed to have a higher β-phase fraction than the core, and this effect is pronounced in the 2.5mm thick castings. In the 5mm plates, there is minimal variation in the volume fraction of β-phase as a function of through thickness location. In contrast, in the 2.5mm thick plates for the alloys containing higher Al contents a significant change in the β-phase was observed depending on the through-thickness location with a maximum β-phase fraction observed approximately 250 μm from the casting surface.

Coincident with the through thickness variation in the volume fraction of β-phase, there is also a change in the particle shape and degree of interconnection of the β-phase. Isolated β-phase particles are found in both the skin and core regions of the AM40 plates (Figure 3.1). As the alloy Al concentration increases, the volume of point particles in the skin increases and the β-phase in the core region becomes increasingly interconnected. This can be seen in Figure 3.1, where the β-phase network in the core of the 2.5 mm thick AM70 forms a more complete network than in that of the AM40 2.5mm core. This trend is similar in the 5mm thick plates, although the frequency of

the larger, networked β-phase particles is lower due to the lower overall volume fraction of β-phase observed.

Shrinkage Porosity

In addition to externally solidified grains, other extrinsic microstructural features were observed, specifically, pores, pore bands and oxide films. The SVDC process used for casting in this study reduced the amount of porosity within the plates compared to that generally observed in high pressure die castings [32]. The microporosity that was observed was typically shrinkage porosity, with minimal gas entrapment, as observed in Figure 3.2. Typical levels of porosity measured on polished surfaces were less than 2% area fraction, independent of Al content (Figure 3.8). The shrinkage porosity was frequently observed in a "defect band" structure that was highly variable from casting to casting and location to location.

Typical of the chaotic molten metal flow produced by HPDC, defect bands occurred in many, but not all of the castings. If present, they were observed approximately 500 μm from the surface of the casting in the 2.5mm plates, and between 1000 and 2000 μm from the surface in the 5mm plates. The defect bands varied in width, and while there was no discernable band structure in some samples, there were multiple bands in others. This is comparable to previous work by Gourlay et al., where defect band appearance varied from casting to casting [33]. Oxide films were also observed in many castings. There was a wide range of oxide sizes observed, from approximately 30-100 μm, however they were not quantified in this study.

3.3.2 Mechanical Behavior

Hardness Testing

The through-thickness spatial variation in microhardness was measured for the 4 and 7 wt. % Al in both the 2.5 and 5mm plates. The resulting microhardness maps are shown in Figure 3.9. Porosity bands are observed in sub-surface in the 5mm plates in Figure 3.9(c) and (d). Automated regular measurement grids were used with a spacing of 100 μm. Locations with a measured hardness above 100 Vickers hardness were locations where indents were placed on either oxide films or large AlMn intermetallic particles. The formation of a high hardness skin region was observed in the 2.5mm plates. This skin is approximately 600 μm thick. This is consistent with the first observance of ESCs at approximately 600 μm subsurface as observed in the 2.5mm plates. In the 5mm plates, the thickness of the higher hardness skin was somewhat variable, but had a nominal thickness of approximately 1100 μm. Defect bands were observed in the core regions of the 5mm plates, and some regions of higher hardness in the core. This is consistent with the grain size distributions observed, as the formation of large grains was also observed in the skin regions of the 5mm plates.

Tensile Testing

Representative tensile curves for each of the eight conditions of the as cast plates are shown in Figure 3.10. Table 3.3 summarizes the tensile properties for each condition, including the average and standard deviation for each property. In general, with increasing Al content, an increase in yield strength and a decrease in ductility, fracture strength and strain hardening exponent was observed as shown in Figure 3.11 and Figure 3.12.

In Figure 3.11(a), yield strength was observed to increase linearly with increasing Al content of the alloys. As the Al content increases from 3.8 to 7 wt. %, there is an increase in yield

strength from 109 to 127 MPa and from 81 to 105 MPa in the 2.5 and 5.0 mm thick plates, respectively. This is an increase in yield strength of 16.5% for the 2.5 mm thick plates and 29.6% for the 5.mm thick plates. The yield strength of the 5mm plates was consistently between 20 and 30 MPa lower than in the 2.5mm plates.

Elongation to failure tended to decrease with increasing Al content and thickness, Figure 3.11(b). The elongation to failure between the least and most ductile specimens ranged up to 11% within a single condition. The highest value was 18.4% for the AM40 2.5mm thick plates, the lowest value was 3.1% for the AM70 2.5mm thick plates. Overall, the 2.5mm plates tended to have higher ductility, although the ductility was similar for both plate thicknesses of AM70.

The samples did not exhibit necking, so the strength at fracture is determined rather than the ultimate tensile strength. It appears that fracture strength of the 5mm plate castings is weakly dependent on Al content as shown in Figure 3.11(a). The 5mm plates have a slightly lower fracture strength than the 2.5mm plates. Compared with the yield strength, substantially more variability was observed for the fracture strength. The ranges observed in fracture strengths is likely tied to the variation in overall elongation as discussed above.

Strain hardening exponent can be calculated using various constitutive relationships. Two common methods of calculation, the Hollomon (Equation 3.1) and Ludwik (Equation 3.2) empirical models, were used to quantify the influence of Al content and plate thickness on work hardening. The strain hardening exponent, n_1, and strength coefficient, K_1, are found from a true stress – true strain curve for both equations. The Ludwik strain hardening parameters tend to be higher values than those determined using the Hollomon relationship. Consistent with the findings for yield strength, the strength coefficient, K, tends to increase with increasing Al content, while

the strain hardening exponent decreases. The strain hardening exponents in Table 3.3 are comparable to those measured at a similar strain rate in AZ series Mg alloys [34].

[3.1] $\sigma = K\varepsilon^{n}$
[3.2] $\sigma = \sigma_Y + K_1\varepsilon^{n_1}$

Within a single casting, variability of properties can be significant due to the stochastic nature of microstructures present in high pressure die castings. These large data populations allowed quantification of the statistical significance of the observed differences in the mean and standard deviation, as well as the level of significance of the scatter using the Coefficient of Variation (COV). Using an analysis of variance (ANOVA) the statistical significance of the differences depicted in Figure 3.11 and Figure 3.12 could be determined. For this purpose, a 2x4 factorial ANOVA was conducted using the open source software, R, which incorporated any random effects for each material property within a given plate. Based on this ANOVA, the observed effects (or lack of effects) of aluminum content and sample thickness on the tensile properties were determined to be statistically significant differences except for the 2.5mm AM40 and AM50 conditions. These conditions could not be statistically proven to be different populations; however, their behavior was consistent with the overall trends shown in Figure 3.11.

To quantitatively assess the variability between properties, the COV was calculated for each property and is listed in Table 3.4. The COV is found by dividing the standard deviation by the mean, and is a measure of the overall variability of a set of samples, independent of typical sample means or measurement units, so that we can compare variability between properties. A sample set with no variation in the mean has a COV of zero, while a COV greater than 10 indicates that the sample set has a high degree of variability or dispersion in the dataset.

Overall there was minimal scatter in the yield strength values for a given condition, with a maximum sample to sample scatter of 12 MPa for AM70 in the 2.5 mm plate condition. The yield strength COV was consistently low, between 1 and 3. In contrast, ductility had much higher variability with a maximum range of 11% elongation for a single condition. The COV for elongation to failure was particularly high, with a maximum of 24.5, which is typical for ductility in cast materials [32]. It is common to see outliers in the distribution of elongations for a given condition. These outliers are more than 1.5 times the standard deviation. Qualitative fractography reveals that the outlier samples with low ductility typically have a large defect on the fracture surface, either an oxide film or porosity. Figure 3.11(b) shows the range of ductility observed for each condition. The COV for fracture strength and the Hollomon strain hardening exponent indicated that these properties were reasonably well behaved, exhibiting values that were low to moderate, as show in Table 3.4.

3.4 Discussion

3.4.1 Microstructure discussion

Quantitative characterization of microstructural features has been limited in previous research on HPDC AM series alloys and thus a major contribution of the current study is the quantitative microstructural information coupled with statistically significant mechanical behavior datasets.

In-mold and ESC grains are the major microstructural features which are dependent on the through-thickness location. In-mold grain size was found to be independent of Al content and plate thickness. This is consistent with previous observations made by Bowles et al. [35]. The in-mold grain size is very fine immediately adjacent to the casting surface in the 2.5mm plates, but this rapidly cooled region is only 10-25 μm thick. The grain size quantified in the current study is

comparable with that reported in HPDC binary Mg-Al alloys in other studies [35,36]. By thresholding the data used to calculate the grain diameter for in-mold grains and ESCs separately, the in-mold grain size can be better defined. A similar fraction of ESCs was observed in both the 2.5mm and 5mm thick plates. ESC size and distribution have been shown previously to vary based on the HPDC gating systems, but plates in this study had gate inlets that were unrestricted (e.g. they were similar in thickness to the plate thickness). In addition, metallographic samples were taken from the same location in each plate in order to minimize any location effects [37]. Variation in the ESC fraction is likely a random effect due to variation within the casting parameters and sampling, leading to range in ESC fraction from 30 – 60%. This is similar to the range of ESC fractions observed by Laukli [38].

The die cast skin region can have an important influence on tensile properties [13,32,39]. There are a number of methods which have previously been used to define the skin thickness – defect band distance, microhardness, grain size variation, and microplasticity analysis [33,39–41]. In the current research, the skin was somewhat difficult to quantify. The transition from skin to core regions is defined using a combination of an increase in the area average grain diameter above 30 μm, and a decrease in the hardness in the core regions. Operationally, the skin was determined to be the region from the casting surface to approximately 600 μm in depth in the 2.5mm plates based on grain size and microhardness mapping. However, the 5mm plates did not show a consistent change in grain size and generally have a slightly larger grain size than the 2.5mm plates. There is a higher and somewhat variable hardness band which is approximately 1100 μm thick.

Microhardness mapping has shown that the skin layer is non-uniform through a casting, and that the difference in hardness increases between skin and core with Al content [16,26].

Microhardness mapping is utilized in this study in order to validate the skin thickness obtained from the average grain size. Microhardness results correspond well with previous work by Yang et al. for the 2.5mm plates. In the 5mm plates, the hardness is slightly higher in the skin than the core, and there is a significant decrease shown around defect bands. The overall hardness in the 5mm plates is lower than in the 2.5mm plates, likely due to the larger area average grain size through the thickness.

As expected for the non-equilibrium solidification conditions present in high pressure die castings, as the Al content increased, the β-phase volume fraction also increased [42,43]. As sample thickness increased, the amount of β-phase decreased, similar to behavior observed by Cáceres [19]. Total β-phase fraction through thickness as measured by XRD correlates well to previous work by Barbagallo [44]. In addition, the shape and distribution of the β-phase eutectics changed as a function of distance from the surface, as previously observed in AZ91 [45]. For AM40 and AM50, the β-phase is in the form of point particles through the full thickness. In AM60 and AM70, interconnected networks begin to form and increase in size with aluminum content. This change in β-phase structure was much stronger in the 2.5mm plates than the 5mm plates, similar to the grain size behavior.

The high cooling rates associated with high pressure die casting are not at equilibrium and lead to the partitioning of Al from the center of the α-Mg grains into the grain edges. This produces coring of the α-Mg cells, with a low Al content core to an Al-rich solid solution at the edges. Scheil solidification conditions are often used to model the microstructural development in non-equilibrium cooling [46], although it is not clear whether this is appropriate for the solidification conditions present in HPDC or SVDC [47]. Scheil-Gulliver solidification assumes no diffusion in the solid phases, no concentration gradients in the liquid, and that equilibrium exists at the

interface. In this investigation, the β-$Mg_{17}Al_{12}$ phase fraction was computed assuming Scheil solidification conditions using ThermoCalc, with the TCMG4 database, with the results shown in Figure 3.7. The amount of β-phase overall through the casting thickness can be compared to that predicted by the Scheil solidification model [46], and is lower than expected.

The plate castings used in this study were produced using SVDC and thus the porosity levels in these plates were significantly lower than that observed for typical HPDC components. This is consistent with previous observations in AZ91 that application of very high vacuum pressures results in lower levels of porosity [48,49]. In the current study, porosity levels were determined to be independent of Al content and thickness. Although some previous work has suggested that porosity increases with increasing plate thickness, this is not always the case [20,50]. In the current study, porosity was observed in the core of the plates, between dendrite arms of ESCs, which is similar to recent work by Li et al, where shrinkage porosity was imaged using X-ray tomography on a HPDC AM60 sample [51]. The defect band structure observed for all conditions is similar to that observed by Laukli in AM60, forming approximately 1000-2000 μm from the casting surface in the 5mm plates [37]. The defect bands are not present in all castings [33,52]. There is no consistent effect of Al content or thickness on the formation of defect bands, which is consistent with previous observations. Similarly, some macro-segregation of Al was observed in the near surface regions, comparable to that observed by Lee et al. [53]. This occurs in less than 1% of the area observed and is not considered significant.

3.4.2 Tensile properties

With increasing Al content, there is an increase in yield strength and decrease in ductility, strain hardening exponent and hardening coefficient. This is consistent with prior work from Aune et al. and Dargusch et al [21,54,55]. The general trend of increasing yield strength with Al content

is explored in detail in the following section. The reduction in ductility with Al content could be attributed to a number of different factors, in particular, to the increased strengthening from increased Al solute content, increasing β-phase fraction, or shrinkage porosity which leads to local cracks in the microstructure. Further study is needed to identify the dominant final fracture mechanisms in these SVDC alloys. The strain hardening exponent is a measure of the capability of a metal to deform before fracture. The decrease in strain hardening exponent reflects the decreased hardening capacity in the higher aluminum content alloys. This is comparable to previous work by Tahreen in the AZ series [56]. The Ludwik strain hardening exponent is computed in order to compare with previous work by Cheng et al. to determine material properties for use in a FEA model [57].

With increased section thickness, lower yield strength and ductility is observed. This is consistent with previous observations by a number of researchers [19,20,54,58–60]. Aghion et al. attributes the decreased yield strength with increased thickness to the increase in solidification time and in turn, the increased grain size [58]. However, average grain size is only slightly larger in the 5mm plates for the current results. Instead, we attribute this decrease to the increased grain size on the surface of the casting compared with the surface regions of the 2.5mm thick castings, and the increased ESC fraction, which significantly reduces the effect of grain boundary strengthening. This is further explored in the model development section below.

3.4.3 Yield strength model

By using measured microstructural features as input, physics-based models for yield strength can be developed. In general, linear superposition methods have been used to predict the contributions to yield strength from different strengthening mechanisms [61–63]. There are three primary strengthening mechanisms active for HPDC Mg alloys. These mechanisms are grain

boundary, σ_{gb}, solid solution, σ_{ss}, and, so-called, "dispersion" strengthening, σ_{disp} [19,64]. The overall strength can be predicted using linear superposition for these three mechanisms as shown in equation 3.3 [16,65].

[3.3] $\sigma_y = \sigma_{gb} + \sigma_{ss} + \sigma_{disp}$

Recent approaches to this linear superposition of mechanisms for cast Mg alloys have been proposed by Sharifi et al., Toda-Carabello et al., and Yang et al. [16–18]. These three models have been developed for use in multiple cast Mg alloys, including binary Mg-Al, AM60, and the AZ series. The key differences between each of these models are in the method of calculating each strengthening component, and the ability to extend to other major alloying elements, and the manner in which they deal with microstructural inhomogeneities that are commonly observed in HPDC materials. Using these models as a starting point, we have developed a linear superposition model that accounts for the three primary strengthening mechanisms, and also deals with microstructural inhomogeneities (skin and core) and the bimodal nature (in-mold grains vs ESCs) of HPDC microstructures. For a given region of the casting, σ_y is determined using the linear superposition model (Equation 3.3), with the relevant parameters given for the specific alloy/region under consideration. The manner of dealing with the specific mechanisms is described below.

The strengthening components used in Equation 3.4 are calculated for each region of uniform microstructure in the casting, specifically the skin and the core regions. By taking these regions of uniform microstructure into account, the yield strength can be estimated using a weighted or composite model as suggested by Yang [16]. For the castings investigated in this study, the fraction of material that is the skin, f_{skin}, is found by doubling the measured skin thickness, and dividing by the total plate thickness. As previously described, using hardness

mapping and the presence of ESCs, the skin thickness could be estimated to be 600 μm thick in the 2.5mm plates and 1100 μm thick in the 5mm plates. In more complex castings it is also likely related to the molten metal flow patterns and cooling rate variation [66]. Thus the skin fraction, f_{skin}, observed in this study is 0.45 for both the 2.5mm plates and the 5mm plates. Within both the skin and core regions, the specific microstructural features and strengthening elements are individually accounted for in our calculations.

[3.4] $\sigma_{y_{total}} = f_{skin}\sigma_{y_{skin}} + (1 - f_{skin})\sigma_{y_{core}}$

The solid solution strengthening term, σ_{ss}, accounts for strengthening due to solute atoms impeding dislocation motion, and is a function of the elastic and size misfits between solute and matrix atoms. In the AM-series alloys investigated here, solute strengthening arises from both Al and Mn in a Mg solid solution. We account for solid solution strengthening based on a first principles model developed by Yasi et al. [68]. The influence of solute elements on the critical resolved shear stress for dislocation motion on the basal plane has been modeled by Yasi et al. using density functional theory (DFT) [67]. Yasi et al. assume a dilute concentration, weak obstacle Fleischer approach for predicting the force necessary to move a dislocation and overcome solute drag [68]. This is given as a function of the atomic solute fraction, c, and a potency factor, M. The potency factor of Al and Mn was calculated by Yasi et al. as M_{Al} = 19.6 MPa and M_{Mn} = 120.8 MPa [67]. In order to determine the yield strength contribution from solid solution strengthening, the critical resolved shear stress is multiplied by the Taylor factor, m. A Taylor factor of 4.5 is used in this work, as calculated for pure, polycrystalline Mg with random texture [69,70]. The random texture is consistent with the HPDC materials investigated in this study. The atomic fraction of Al and Mn in solid solution in the skin and the core determined using EPMA provides the value for c_x in Equation 3.5.

[3.5] $\sigma_{SS} = m * \sum M_x c_x^{\frac{1}{2}}$

It is observed that for the particular alloys investigated in this study, as the amount of Al in solid solution within the α-Mg grains increases, the amount of Mn in solid solution was observed to decrease (Figure 3.6). Mn is known to be a very strong strengthening agent [68]; however, since the fraction of Mn in solid solution decreases with increasing Al content, there is also a decrease in Mn solid solution strengthening at higher Al contents for the conditions investigated. The net result is that the combined solid solution strengthening from both Al and Mn remains constant over the range of Mg-Al-Mn alloys investigated. These results can be compared to previous work by Toda-Carabello and Caceres, who predict solid solution strengthening using the Labusch model, with an experimental fitting parameter [18,71]. Both the Fleischer (n = ½) and Labusch (n = 2/3) models show similar and good agreement with solid solution strengthening in dilute Mg-Al alloys [71]. The amount of strengthening predicted for Al in solid solution is essentially equivalent for all of these models, as shown in Table 3.5, after adjusting for the Taylor factor. However, we prefer the approach provided by Yasi et al. since it also includes well defined solid solution strengthening parameters for all alloying elements in Mg and thus can be readily extended to other alloys.

In the present case, minimal variation in solid solution strengthening is predicted to occur between the skin and core of the plates. The skin has a higher fraction Al in solid solution than in the core, likely due to the high cooling rate. In addition, the core has a higher fraction of ESCs, which tend to have a lower Al solute content [16]. The solid solution strengthening component in the core consists of an average solute content for both the in-mold grains and ESCs due to measurement limitations. However, this change in Al is less than 1.5 wt.% Al, even in the most

concentrated alloys. While this is a measureable change, it has a relatively modest effect on solid solution strengthening. Since the solute variation through thickness is the same in both the 2.5 and the 5mm plates, this factor does not appear to be responsible for the decreased yield strength in the 5mm plates.

The influence of grain size on yield strength is given by the Hall-Petch relationship in Equation 3.6 [72,73]. The intrinsic stress term σ_0 in equation 3.6 is taken to be the CRSS of pure Mg with no influence of solute content. The intrinsic stress, σ_0, taken to be 4.5 MPa for all regions of the castings. This is based on single crystal studies of the CRSS of Mg, which typically find a value of 0.7-1MPa, and using the Taylor factor of 4.5 [74–77]. Previous work has used a CRSS of 12MPa, determined from extruded Mg, but this is expected to be lower for cast magnesium alloys which have random grain orientations [78,79].

Alloying has also been shown to effect the Hall-Petch parameters, specifically the locking parameter, k_y [71,79,80]. Different mechanistic rationales from this have been given varying from changes in shear modulus with solute content [18] to changes in slip transfer across or nucleation at grain boundaries [66]. The influence of solute on the Hall-Petch locking parameter is considered separately from the matrix solid solution strengthening component described above. Toda-Carabello et al. proposed that the influence of solute elements on k_y follows the form given in Equation 3.7, in which k_y is linearly proportional to the solute concentration multiplied by the proportion of the locking parameter that attributable to a specific element, $\Delta k_{y,x}$. As shown in Equation 3.7, this is then added to the locking parameter determined for pure Mg, $K_{y,mg.}$ In the current work, we estimate the locking parameter, k_y to vary from 0.27 to 0.33 MPa $\mu m^{1/2}$, depending on alloy composition. This was determined empirically by fitting the grain boundary component of the yield strength to the influence of solute content in Equation 3.7 [16,18]. The

locking parameter associated with pure Mg, $k_{y,Mg}$ has been determined to be 0.21-0.22 [78,79]. We have used a value of 0.21 in the current work. We conducted a linear regression for $\Delta k_{y,Al}$ to account for the influence of Al on the grain boundary strengthening, accounting for Al in atomic fraction, c_x. In this case, $k_{y,Al}$ is calculated to be 2.75 in these alloys using the area average in-mold and ESC grain sizes described in Section 3.1.1. Due to the low solubility of Mn in Mg and that it is nominally constant for the four alloys investigated, we assume that the effect of Mn on k_y is negligible and $\Delta k_{y,Mn} = 0$. Further work is needed to determine if this assumption is valid.

[3.6] $\sigma_{gb} = \sigma_0 + \mathrm{k_y} * \mathrm{d}^{-\frac{1}{2}}$

[3.7] $k_y = k_{y,Mg} + \sum c_x \Delta k_{y,x}$

The grain size effect on strength is further complicated by the presence of the fine grained skin and the relatively coarse grained core regions. In addition, within each of these regions there are often two types and sizes of grains, fine, in-mold grains and coarser ESCs. To account for this we used a bivariate grain size distribution to estimate the strengthening effects of the in mold grains and the ESCs using Equation 3.8 [81]. This allows for the estimating the influence of ESCs which, due to their low frequency, only slightly increase the number average, but which can occupy up to 50% of the area in the core of the castings, significantly reducing the overall strengthening effect. In addition to being coarser, ESCs are thought to be areas of low Al content [36], however this effect is not considered in the current study.

[3.8] $\sigma_{gb} = \sigma_0 + f_{ESC} * \left(\mathrm{k_y} * \mathrm{d}_{\mathrm{ESC}}^{-\frac{1}{2}} \right) + (1 - f_{ESC}) * \left(\mathrm{k_y} * \mathrm{d}_{\mathrm{in-mold}}^{-\frac{1}{2}} \right)$

The 5mm plates exhibited lower yield strengths in all of the alloys studied. The observation could be understood by accounting for the increased grain size in the skin region of the 5mm thick samples compared to the 2.5mm thick samples. This leads to a reduction in the strengthening

effects attributed to the die cast surface skin. When these factors were considered in the weighted model a good estimate of the strength of all conditions was achieved.

The final strengthening mechanism in the linear superposition model is so-called "dispersion" strengthening which occurs as a result of the β-$Mg_{17}Al_{12}$ particles in the material [19]. Since these particles are very coarse, strengthening occurs primarily through stress redistribution that occurs due to the modulus difference between the β-$Mg_{17}Al_{12}$ particles and the α-Mg matrix, so this is more appropriately termed composite or modulus mismatch hardening. Here we use the relationship in Equation 3.9 that was developed for this mechanism by Caceres et al. [16, 67] based on the work of Brown and Clarke [73] for disk shaped particles of β-phase. Overall, due to the low β-phase fraction measured in these alloys and their low modulus difference, this mechanism for strengthening was determined to be very low compared to solid solution and grain boundary strengthening mechanisms even in the most concentrated alloys. The average β-phase volume fraction through thickness is used in this calculation due to the minimal change through thickness.

[3.9] $\sigma_{disp} = 135 * f_{beta}$ [71]

The predicted values found using the weighted linear superposition model defined in Equation 3.4 and Equation 3.8 can be compared to the measured yield strength values. A summary of the constants used in the current linear superposition model for these Mg-Al-Mn alloys is provided in Table 3.5, along with a comparison to the values used by other recent investigations. As shown in Figure 3.13, the estimated values match the experimental tensile results for both the 2.5 and 5mm thick plates. The goodness of fit is computed using the coefficient of determination, R^2. The coefficient is 0.5 for the fit to both plate thicknesses, presumably due to the high intrinsic strength predicted by the $k_{y,Mg}$ coefficient, which is a constant set by the literature. This reduces the predicted slope by lowering the fit value of $k_{y,Al}$. In general, the grain boundary strengthening

contributes approximately 60-65% of overall strengthening, 30-35% solid solution and 1-5% dispersion in the 2.5mm plates. Based on the skin thickness measurements, the skin and core are almost equal weights. For the overall grain boundary strengthening in the 2.5mm plates, the skin is responsible for 55%, as compared to the core. This is similar in the 5mm plates. The yield strength of the 5mm plates is predicted to be lower due to the higher ESC fractions observed in the core of the plates, and increased grain size at the surface. There is a proportional decrease in both solid solution and dispersion hardening in the 5mm plates, but a greater decrease in the grain boundary strengthening, accounting for the lower overall strength.

There is typically a range of measured values associated with yield strength for any given material. This variation can be ascribed to variations in local microstructures. This is likely related to the grain size distribution changes based on ESC occurrence and cooling rate effects in different locations. Grain boundary strengthening is the strongest strengthening mechanism in these alloys, due to the fine primary α-Mg grain size. However, significant variability is introduced due to the occurrence of ESCs in the core. A broad distribution in ESC sizes is observed, with ESCs ranging from 30 to 200 μm in diameter. The variation in ESC size and area fraction observed within a given casting could have a significant effect on the yield strength. By varying the ESC size and area fraction, a range of strengths on the order of 5-10MPa is observed. This is determined by assuming different levels of ESC fractions and average sizes. Accurate characterization of the size and fraction of ESCs generated by a given casting process is particularly important for an accurate representation of the overall grain boundary strengthening component.

Skin thickness has been shown to influence the overall yield strength [41]. However, a precise method of determining skin thickness is still unavailable. Good correlation is observed between hardness and grain size in the 2.5mm plates, but not in the 5mm plates. In these castings,

there is a band of higher hardness at the surface, however it is thicker than that observed by Yang et al. for similar compositions and thicknesses [40,82]. A model comparing the relative hardening of the skin and core was assessed by Yang et al. [82], which predicts a skin fraction of approximately 0.10 when applied to Mg alloys with 1-6 wt.% Al. Sharifi et al. predicts a skin thickness using heat transfer rates and cooling rate-grain size relationships of 400 μm thick in a 2.6mm thick casting, leading to an equivalent skin fraction of 0.3. The skin thickness is assumed to be the same for the 5mm plates, but is complicated by the large grains frequently observed in the skin region. Significant variation in the yield strength is observed, likely due to the stochastic distribution of grain sizes observed due to the high pressure die casting.

3.5 Conclusions

Quantitative characterization of microstructure and tensile behavior has been conducted for Super Vacuum Die Cast Mg-Al-Mn alloys with a range of Al contents and two thicknesses. Based on these results, a physics-based model has been developed for predicting alloy and plate thickness effects on yield strength. This model takes in to account microstructure gradients within the die casting that exist in the skin and core regions of high pressure die castings. It also takes into account the bimodal nature of the grain structure in high pressure die castings. The most significant effects on strength are observed to be grain boundary and solid solution strengthening. Dispersion strengthening due to the presence of β-$Mg_{17}Al_{12}$ particles is estimated to provide only a minimal increase in the strength.

Specific findings were:

- With increasing alloy Al content, there is an increase in the β phase fraction. This increase is lower than that predicted by a Scheil solidification model.
- In-mold grain size is independent of alloy Al content.

- Large externally solidified crystals (ESCs) were observed predominately in the interior regions of castings. However, in the 5mm plates, some ESCs were observed near the casting surface.
- The tensile properties were dependent on the Al content of the alloys. With increasing Al content, the yield strength increased while both strain hardening exponent and ductility decreased.
- A physics based yield strength model has been parameterized and predicts the experimental results reasonably well. Key features that impact the yield strength are the size and area fraction of ESCs, the solute effects on the Hall-Petch locking parameter, k_y and solid solution strengthening.
- The yield strength was 20-30 MPa lower in the thicker plates. This can be quantitatively attributed to the increased area fraction of ESCs observed near the casting surface, and a slight increase in the in-mold grain size.

Note: All experimental data from this investigation is available via the Materials Commons at: https://materialscommons.org/mcpub/#/details/238117f2-6066-4a78-a6f0-e2afdf664625

Acknowledgements:

The authors are grateful to Xin Sun, Mei Li, and Joy Forsmark for many helpful discussions. Thanks to Larry Godlewski and Jacob Zindel at Ford Motor Company for providing the SVDC cast plates. The authors gratefully acknowledge funding for this project from the Department of Energy Office of Vehicle Technologies under the Automotive Lightweighting Materials Program managed by Dr. Will Joost, via subcontract with Pacific Northwest National Laboratory. The use of the Materials Commons to archive the data presented in this paper is appreciated. Funding for Materials Commons is from the U.S. Department of Energy, Office of Basic Energy Sciences, Division of Materials Sciences and Engineering under Award #DE-SC0008637 as part of the Center for PRedictive Integrated Structural Materials Science (PRISMS Center) at University of Michigan.

References

[1] B.L. Mordike and T. Ebert: *Mater. Sci. Eng. A*, 2001, vol. 302, pp. 37–45.
[2] A.L. Bowles, Q. Han, and J.A. Horton: in *Essent. Readings Magnes. Technol.*, 2014, pp. 197–202.
[3] A.A. Luo: *J. Magnes. Alloy.*, 2013, vol. 1, pp. 2–22.
[4] M.M. Avedesian and H. Baker, eds.: *ASM Specialty Handbook - Magnesium and Magnesium Alloys*, ASM International, Metals Park, OH, 1999.
[5] K.V. Yang, M.A. Easton, and C.H. Cáceres: *Adv. Eng. Mater.*, 2013, vol. 15, pp. 302–7.
[6] M .R. Barone and D. A. Caulk: *Int. J. Eng. Sci.*, 2000, vol. 38, pp. 1279–1302.
[7] J.H. Forsmark, J.W. Zindel, L. Godlewski, and A. Caliskan: *SAE Int.*, 2012, pp. 2–10.
[8] C. Dørum, O.S. Hopperstad, M. Langseth, O.-G. Lademo, and S. Sannes: *SAE Tech. Pap. Ser.*, 2005, vol. 2005-01–07, p. 8.
[9] J.P. Weiler, J.T. Wood, R.J. Klassen, E. Maire, R. Berkmortel, and G. Wang: *Mater. Sci. Eng. A*, 2005, vol. 395, pp. 315–22.
[10] C.D. Lee: *Mater. Sci. Eng. A*, 2007, vol. 454–455, pp. 575–80.
[11] K.S. Choi, D. Li, X. Sun, M. Li, and J.E. Allison: *SAE Int.*, 2013, pp. 3–10.
[12] J.E. Allison, D. Backman, and L. Christodoulou: *J. Mater.*, 2006, pp. 25–27.
[13] S. Sannes, H. Gjestland, and H. Westengen: *SAE Tech. Pap. Ser.*, 2005, vol. 2005-01–03, p. 7.
[14] J.H. Forsmark, J.W. Zindel, L. Godlewski, J. Zheng, J.E. Allison, and M. Li: *Integr. Mater. Manuf. Innov.*, 2015, vol. 4.
[15] U. Weiss and A. Bach: *La Metall. Ital.*, 2011, vol. 11–12, pp. 31–39.
[16] K.V. Yang, C.H. Cáceres, and M.A. Easton: *Metall. Mater. Trans. A*, 2014, vol. 45, pp. 4117–28.
[17] P. Sharifi, Y. Fan, K. Sadayappan, G. Birsan, and J.T. Wood: in *Magnes. Technol. 2015*, 2015, pp. 351–56.
[18] I. Toda-Caraballo, E.I. Galindo-Nava, and P.E.J. Rivera-Díaz-del-Castillo: *Acta Mater.*, 2014, vol. 75, pp. 287–96.
[19] C.H. Cáceres, W.J. Poole, A.L. Bowles, and C.J. Davidson: *Mater. Sci. Eng. A*, 2005, vol. 402, pp. 269–77.
[20] D. Rodrigo, M. T. Murray, and H. Mao: *SAE Int. Congr. Magnes. Sess.*, 1999.
[21] T.K. Aune, H. Westengen, and T. Ruden: *SAE Tech.*, 1993, pp. 51–57.
[22] C.H. Cáceres and B.I. Selling: *Mater. Sci. Eng. A*, 1996, vol. 220, pp. 109–16.
[23] Tracy D. Berman, Tresa M. Pollock, and J. Wayne Jones: *Metall. Mater. Trans. A*, 2015, vol. 46, pp. 2986–98.
[24] E.I. Barker, K.S. Choi, X. Sun, E. Deda, J. Allison, M. Li, J. Forsmark, J. Zindel, and L. Godlewski: *Comput. Mater. Sci.*, 2014, vol. 92, pp. 353–61.
[25] K.S. Choi, E.I. Barker, G. Cheng, X. Sun, J. Forsmark, and M. Li: *SAE Int. J. Mater. Manuf.*, 2016, vol. 9, pp. 2016-01–0290.
[26] K. Vanna Yang, M.A. Easton, and C.H. Cáceres: *Mater. Sci. Eng. A*, 2013, vol. 580, pp. 191–95.
[27] T.D. Berman: University of Michigan, Ann Arbor, MI, unpublished research, 2016.
[28] Materials Commons, http://materialscommons.org. Accessed 20 Aug 2016.
[29] B. Puchala, G. Tarcea, E.A. Marquis, M. Hedstrom, H.V. Jagadish, and J.E. Allison: *Jom*, 2016, vol. 68, pp. 2035–44.

[30] L.-Y. Wei and R. Warren: *Mater. Sci. Technol.*, 2007, vol. 23, pp. 745–52.
[31] V.Y. Gertsman, J. Li, S. Xu, J.P. Thomson, and M. Sahoo: *Metall. Mater. Trans. A*, 2005, vol. 36, pp. 1989–97.
[32] J.H. Forsmark, Z. Dowling, K. Gibson, C. Mueller, L. Godlewski, J.W. Zindel, and J.M. Boileau: *SAE Int. J. Mater. Manuf.*, 2015, vol. 8.
[33] C.M. Gourlay, H.I. Laukli, and A.K. Dahle: *Metall. Mater. Trans. A*, 2007, vol. 38, pp. 1833–44.
[34] N. Tahreen, D.L. Chen, M. Nouri, and D.Y. Li: *J. Alloys Compd.*, 2015, vol. 623, pp. 15–23.
[35] A.L. Bowles, K. Nogita, M.S. Dargusch, and C.J. Davidson: *Mater. Trans*, 2004, vol. 45, pp. 3114–19.
[36] A.V. Nagasekhar, M.A. Easton, and C.H. Cáceres: *Adv. Eng. Mater.*, 2009, vol. 11, pp. 912–19.
[37] Hans Ivar Laukli: 2004.
[38] H.I. Laukli, C.M. Gourlay, and A.K. Dahle: *Metall. Mater. Trans. A Phys. Metall. Mater. Sci.*, 2005, vol. 36, pp. 805–18.
[39] A.L. Bowles, J.R. Griffiths, and C.J. Davidson: in *Magnes. Technol. 2001*, 2001, pp. 161–68.
[40] K. Vanna Yang, C.H. Cáceres, and M.A. Easton: *Mater. Sci. Eng. A*, 2013, vol. 580, pp. 355–61.
[41] J.P. Weiler, J.T. Wood, R.J. Klassen, R. Berkmortel, and G. Wang: *Mater. Sci. Eng. A*, 2006, vol. 419, pp. 297–305.
[42] H. Cao and M. Wessén: *Metall. Mater. Trans. A*, 2004, vol. 35, pp. 309–19.
[43] M.S. Dargusch, M. Nave, S.D. McDonald, and D.H. StJohn: *J. Alloys Compd.*, 2010, vol. 492, pp. L64–68.
[44] S. Barbagallo, H.I. Laukli, O. Lohne, and E. Cerri: *J. Alloys Compd.*, 2004, vol. 378, pp. 226–32.
[45] W.P. Sequeira, G.L. Dunlop, and M.T. Murray: in *Proc. Third Int. Magnes. Conf.*, 1996, pp. 63–73.
[46] D.J. Sakkinen: *SAE Tech. Pap.*, 1994, pp. 558–69.
[47] D. Mirković and R. Schmid-Fetzer: *Metall. Mater. Trans. A Phys. Metall. Mater. Sci.*, 2009, vol. 40, pp. 974–81.
[48] X.J. Wang, S.M. Zhu, M.A. Easton, M.A. Gibson, and G. Savage: *Int. J. Cast Met. Res.*, 2014, vol. 27, pp. 161–66.
[49] K. Sadayappan, W. Kasprzak, Z. Brown, L. Ouimet, and A.A. Luo: *Mater. Sci. Forum*, 2009, vol. 618–619, pp. 381–86.
[50] M. Zhou, A. Yu, N. Li, H. Hu, and R. Bowers: in *Magnes. Technol. 2006*, 2006, pp. 121–27.
[51] X. Li, S.M. Xiong, and Z. Guo: *Mater. Sci. Eng. A*, 2015, vol. 633, pp. 35–41.
[52] S. Otarawanna, C.M. Gourlay, H.I. Laukli, and A.K. Dahle: *Mater. Charact.*, 2009, vol. 60, pp. 1432–41.
[53] S.G. Lee, G.R. Patel, and A.M Gokhale: *Scr. Mater.*, 2005, vol. 52, pp. 1063–68.
[54] M.S. Dargusch, K. Pettersen, K. Nogita, M.D. Nave, and G.L. Dunlop: *Mater. Trans.*, 2006, vol. 47, pp. 977–82.
[55] P. Bakke, K. Pettersen, and H. Westengen: in *Magnes. Technol. 2003*, 2003, pp. 171–76.
[56] N. Tahreen, D.L. Chen, M. Nouri, and D.Y. Li: *Mater. Sci. Eng. A*, 2014, vol. 594,

pp. 235–45.
[57] G. Cheng, E.I. Barker, E.V. Stephens, K.S. Choi, and X. Sun: *MRS Adv.*, 2016, pp. 1–12.
[58] E. Aghion, N. Moscovitch, and A. Arnon: *Mater. Sci. Eng. A*, 2007, vol. 447, pp. 341–46.
[59] W.P. Sequeira, G.L. Dunlop, and M.T. Murray: in 1996, pp. 63–73.
[60] D.G. Leo Prakash and D. Regener: *J. Alloys Compd.*, 2008, vol. 464, pp. 133–37.
[61] T.N. Baker: in *Yield, Flow Fract. Polycrystals*, 1982, pp. 235–73.
[62] A.J. Ardell: *Metall. Trans. A*, 1985, vol. 16A, pp. 2131–65.
[63] S. C. Weakley-Bollin, W. Donlon, W. Donlon, C. Wolverton, J. E. Allison, and J. W. Jones: *Metall. Mater. Trans. A*, 2004, vol. 35, pp. 2407–18.
[64] C.H. Cáceres, C.J. Davidson, J.R. Griffiths, and C.L. Newton: *Mater. Sci. Eng. A*, 2002, vol. 325, pp. 344–55.
[65] T.N. Baker, ed.: *Yield, Flow, and Fracture of Polycrystals*, 1983.
[66] P. Sharifi, Y. Fan, H.B. Anaraki, A. Banerjee, K. Sadayappan, and J.T. Wood: *Metall. Mater. Trans. A*, 2016.
[67] J.A. Yasi, L.G. Hector, and D.R. Trinkle: *Acta Mater.*, 2010, vol. 58, pp. 5704–13.
[68] R.L. Fleischer: in *Strength. Met.*, D. Peckner, ed., 1964, pp. 93–140.
[69] C. H. Caceres and P. Lukac: *Philos. Mag.*, 2008, vol. 88, pp. 977–89.
[70] J. H. Shen, Y. L. Li, and Q. Wei: *Mater. Sci. Eng. A*, 2013, vol. 582, pp. 270–75.
[71] C.H. Cáceres and D.M. Rovera: *J. Light Met.*, 2001, vol. 1, pp. 151–56.
[72] E.O. Hall: *Proc. Phys. Soc. A*, 1951, vol. 64, pp. 747–53.
[73] N.J. Petch: *J. Iron Steel Inst.*, 1953, vol. 174, pp. 25–28.
[74] A. Akhtar and E. Teghtsoonian: *Acta Metall.*, 1969, vol. 17, pp. 1339–49.
[75] W. B. Hutchinson and M. R. Barnett: *Scr. Mater.*, 2010, vol. 63, pp. 737–40.
[76] K. Fukuda, Y. Koyanagi, M. Tsushida, H. Kitahara, T. Mayama, and S. Ando: in *9th Pacific Rim Int. Conf. Adv. Mater. Process.*, 2016, pp. 794–96.
[77] J. Zhang and S.P. Joshi: *J. Mech. Phys. Solids*, 2012, vol. 60, pp. 945–72.
[78] F.E. Hauser, P.R. Landon, and J.E. Dorn: *Trans. Am. Inst. Mining, Metall. Pet. Eng. Inc.*, 1956, vol. 206, pp. 589–93.
[79] C.H. Cáceres, G.E. Mann, and J.R. Griffiths: *Metall. Mater. Trans. A*, 2011, vol. 42, pp. 1950–59.
[80] P. Sharifi, Y. Fan, J.P. Weiler, and J.T. Wood: *J. Alloys Compd.*, 2014, vol. 605, pp. 237–43.
[81] K.J. Kurzydlowski and J.J. Bucki: *Acta Metall. Mater.*, 1993, vol. 41, pp. 3141–46.
[82] K. Vanna Yang, C.H. Cáceres, A.V. Nagasekhar, and M.A. Easton: *Mater. Sci. Eng. A*, 2012, vol. 542, pp. 49–55.
[83] A. Akhtar and E. Teghtsoonian: *Acta Metall.*, 1969, vol. 17, pp. 1351–56.

Composition	AM40	AM50	AM60	AM70
Al (wt. %)	3.8	4.6	6.0	7.0
Mn (wt. %)	0.55	0.4	0.44	0.44

Table 3.1: Al and Mn alloy compositions for each condition as measured by optical emission spectroscopy.

	AM40 2.5mm	AM50 2.5mm	AM60 2.5mm	AM70 2.5mm	AM40 5mm	AM50 5mm	AM60 5mm	AM70 5mm
In mold Grain skin (μm)	12 ± 3	13 ± 4	12 ± 3	14 ± 3	14 ± 5	20 ± 6	15 ± 4	17 ± 5
In mold core (μm)	16 ± 4	18 ± 5	16 ± 5	17 ± 5	18 ± 5	17 ± 5	17 ± 5	16 ± 5
ESC diameter core (μm)	79 ± 24	70 ± 21	66 ± 18	58 ± 15	64 ± 18	71 ± 22	78 ± 24	75 ± 23
ESC area fraction in skin (%)	0	0	2	5	10	42	13	49
ESC area fraction in core (%)	55	48	46	32	53	61	50	40
β SEM Vol. %	1.4 ± 0.3	1.4 ± 0.3	3.3 ± 1.0	4.9 ± 0.9	0.5 ± 0.1	0.8 ± 0.1	1.4 ± 0.3	2.4 ± 0.4
B XRD Vol. %	0.7	1.0	2.5	3.8	0.3	0.8	1.5	2.5
Porosity area (%)	0.3	0.7	0.9	0.7	0.6	0.7	1.1	0.8

Table 3.2: Microstructure summary for each of the key features, including area average grain diameter for in-mold grains and ESCs, ESC area fraction, β-phase fraction, and porosity levels.

	AM40 2.5mm	AM50 2.5mm	AM60 2.5mm	AM70 2.5mm	AM40 5mm	AM50 5mm	AM60 5mm	AM70 5mm
Yield Strength (MPa)	107 ± 2	109 ± 2	120 ± 3	127 ± 3	82 ± 2	87 ± 2	102 ± 3	105 ± 1
Elongation (%)	14.4 ± 2.9	13.3 ± 2.4	10.5 ± 2.2	5.1 ±1.1	9.6 ± 2.3	7.5 ± 1.5	8.3 ± 1.4	6.2 ± 1.0
Fracture strength (MPa)	229 ± 9	233 ± 12	241 ± 10	208 ± 12	185 ± 18	180 ± 15	209 ± 11	197 ± 11
n Hollomon	.35 ± .002	.354 ± .01	.321 ± .01	.26 ± .02	.38 ± .03	.35 ± .02	.34 ± .01	.30 ± .01
K Hollomon	543 ± 6	558 ± 19	558 ± 13	475 ± 28	512 ± 52	491 ± 36	528 ± 21	489 ± 27
n_1 Ludwik	.81 ± .04	.81 ± .03	.77 ± .04	.75 ± .03	.81 ± .04	.80 ± .02	.78 ± .03	.72 ± .01
K_1 Ludwik	877 ± 105	915 ± 88	900 ± 74	883 ± 45	912 ± 100	909 ± 38	921 ± 54	830 ± 25

Table 3.3: Tensile property summary – mean ± standard deviation for the yield strength, total elongation to failure, fracture strength, and strain hardening parameters (Hollomon and Ludwik) for each condition.

COV (%)	AM40 2.5mm	AM50 2.5mm	AM60 2.5mm	AM70 2.5mm	AM40 5mm	AM50 5mm	AM60 5mm	AM70 5mm
Yield	1.9	2.1	2.7	2.5	2.3	2.7	2.5	1.3
Elongation	19.9	18.1	20.7	21.1	24.5	20.5	16.3	15.6
Fracture Strength	3.7	5.0	4.3	5.8	9.6	8.2	5.4	5.7
n Hollomon	0.6	3.3	2.5	6.3	8.8	5.7	3.3	5.0

Table 3.4: Tensile property coefficient of variation for the yield strength, total elongation, fracture strength, and the Hollomon strain hardening exponent for each condition.

Model	Material	σ_0 (MPa)	K_y (MPa $m^{1/2}$ $at.^{-1}$)	B_{Al} (MPa $at.^{-n}$)	F_{skin} (sample thickness)
Current Work	AM40-AM70	4.5	0.21+.2.75(X_{Al})	20, n = ½	0.45(2.5mm and 5mm)
Sharifi [17,80]	AM60	62.1	0.153	-	0.30 (2.6mm)
Toda [18]	Mg alloys	10	0.21 + 2(X_{Al})	26.7, n = 2/3	-
Yang [16]	Mg-Al	12	0.22 to 0.30	21.2, n = ½ 39.5, n = 2/3 [71,83]	0.10 (3mm)

Table 3.5: Model coefficients from current work and previous work

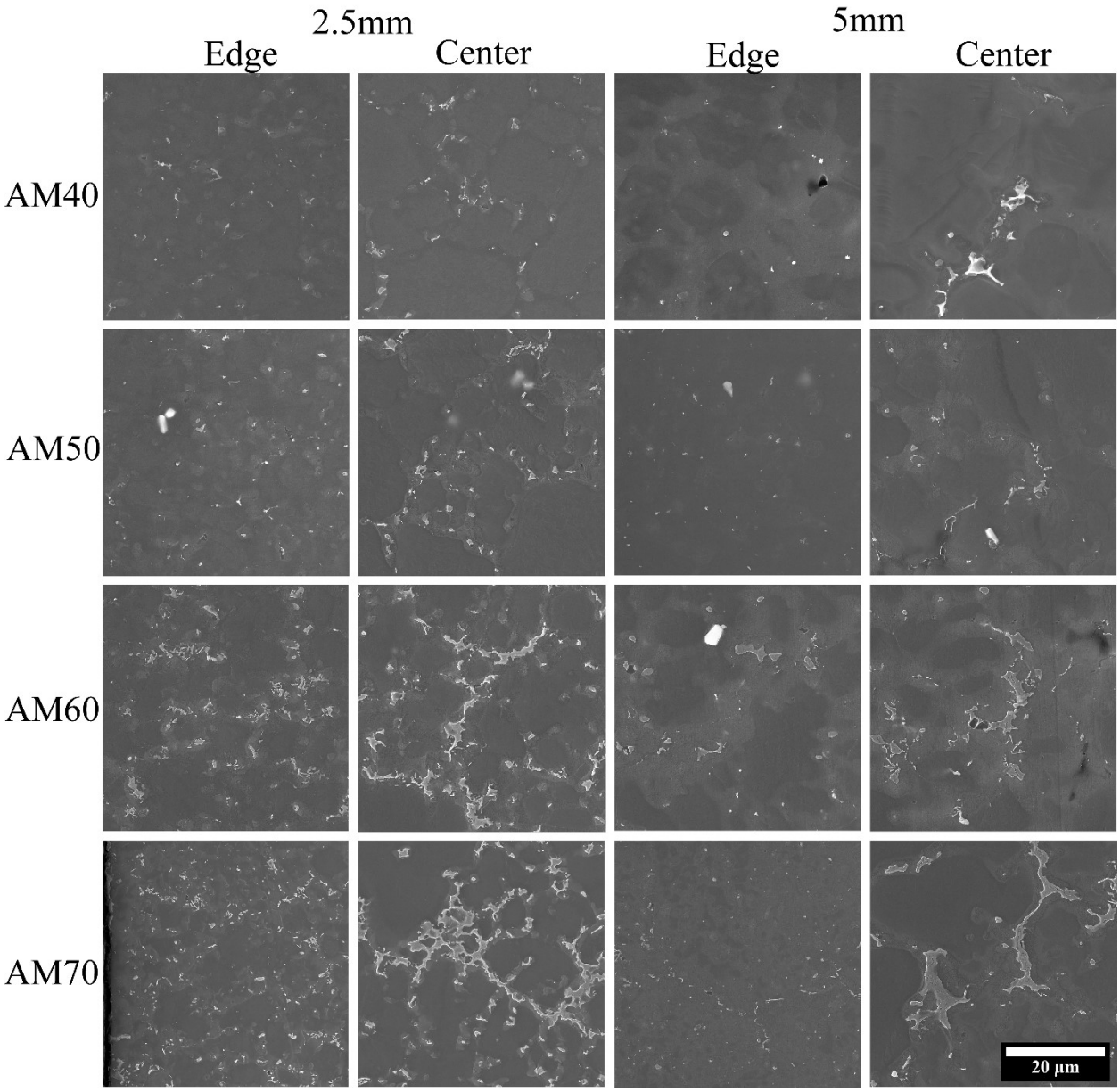

Figure 3.1: The microstructure of the as-cast plates is comprised of fine α-Mg grains (darker grey), surrounded by β-Mg17Al12 eutectic particles (light grey), with randomly distributed Al4Mn particles (white) for each condition.

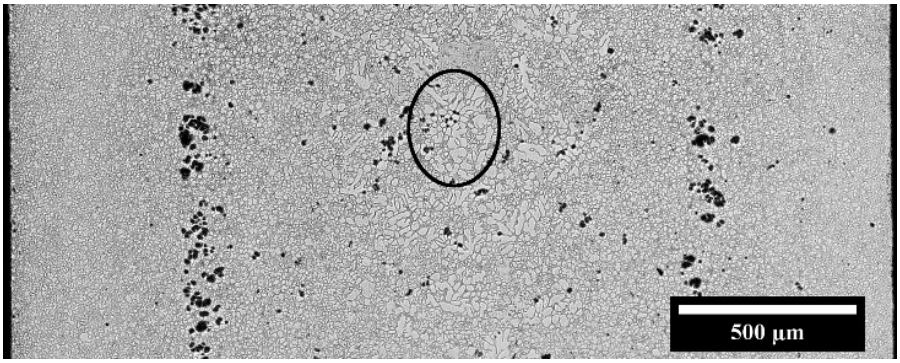

Figure 3.2: Representative image of porosity through the thickness of the plate, where the left and right sides are the casting surface. Image is an optical micrograph of an AM50 2.5mm thick plate. Externally Solidified Crystals (ESCs) (an example is circled) are evident in the core of the plate. Also notable in this image are pore bands roughly 600 µm from the casting surface.

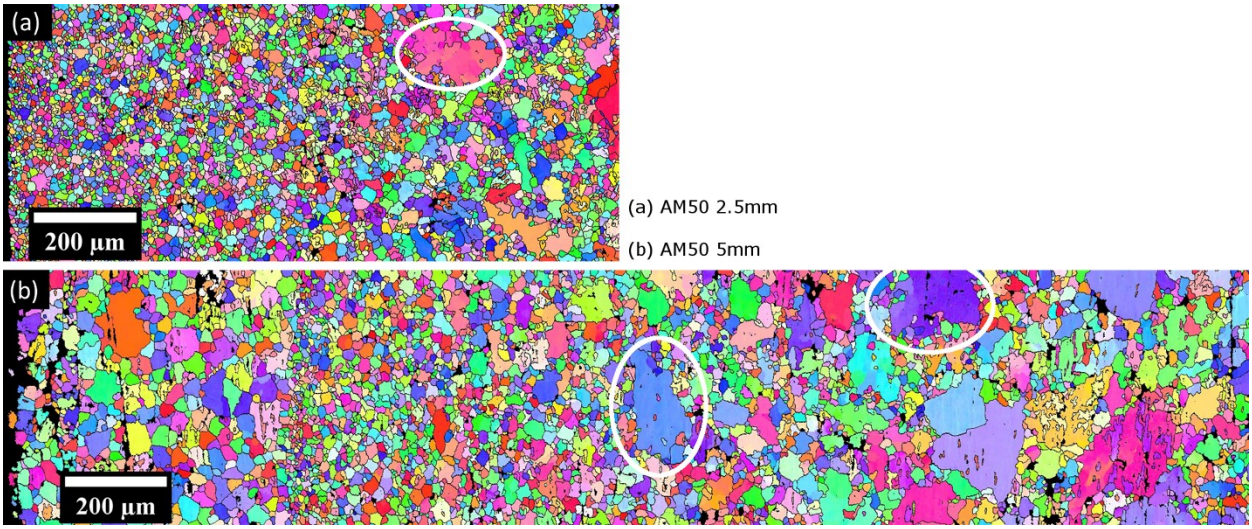

Figure 3.3: Through thickness microstructural variation as characterized using EBSD for a) 2.5mm plate, b) 5mm plate. Note white circles showing large grains associated with externally solidified crystals (ESCs). The as-cast plate surface is on the left of the image.

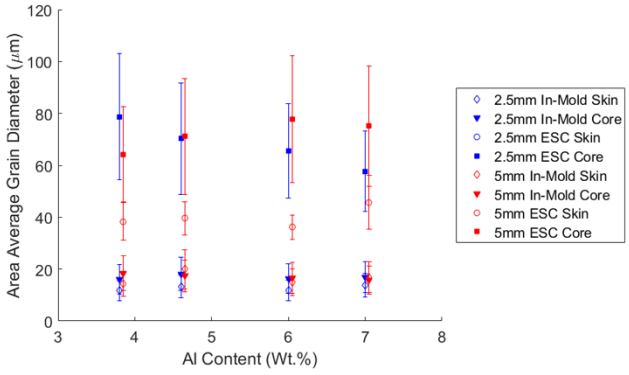

Figure 3.4: Area average grain diameter for in-mold α-Mg grains and Externally Solidified Crystals (ESCs) from each condition and location. Note that ESCs are substantially larger than in-mold grains.

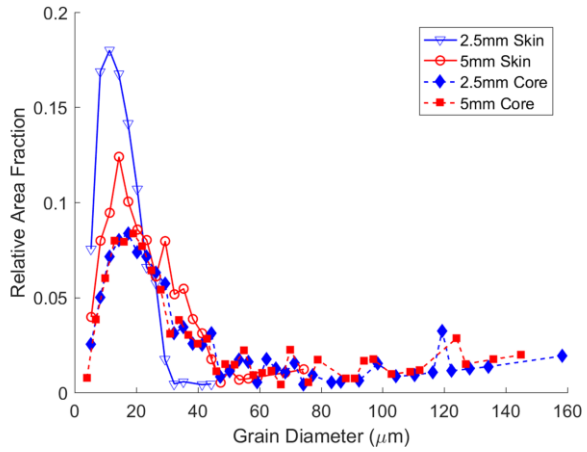

Figure 3.5: Area fraction histogram for the grain size in the skin (solid) and the core (dashed). Large grains are observed in both regions of the 5mm thick plates.

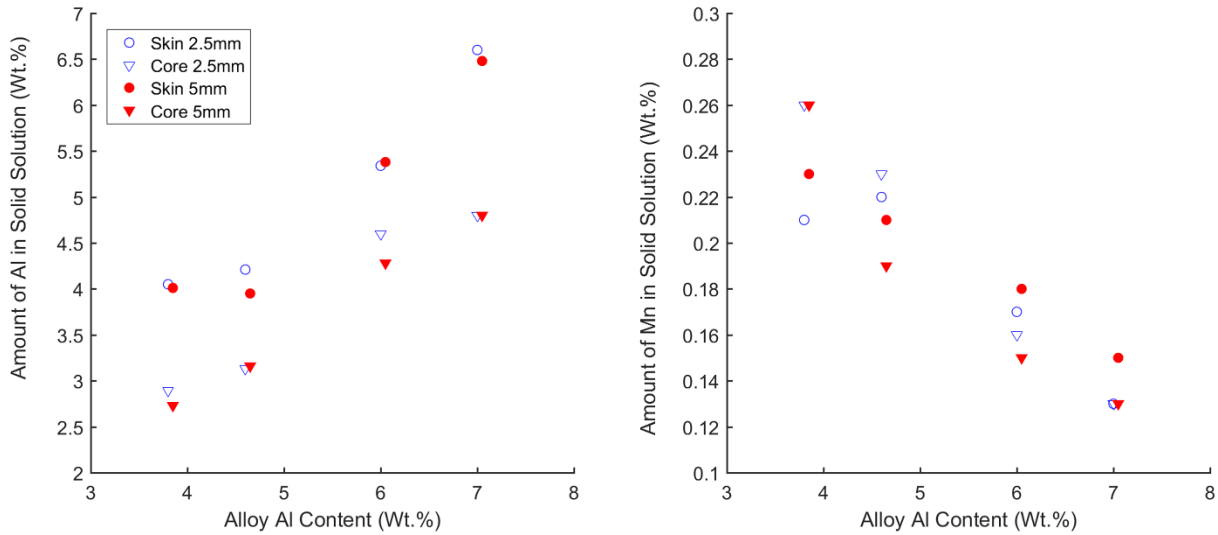

Figure 3.6: Local composition measured by EPMA. As alloy Al content increases, the amount of Al which remains in solid solution increases, while the Mn fraction in solid solution decreases. The amount of Al in solid solution is higher in the skin than in the core, while there is no change in the Mn in solid solution.

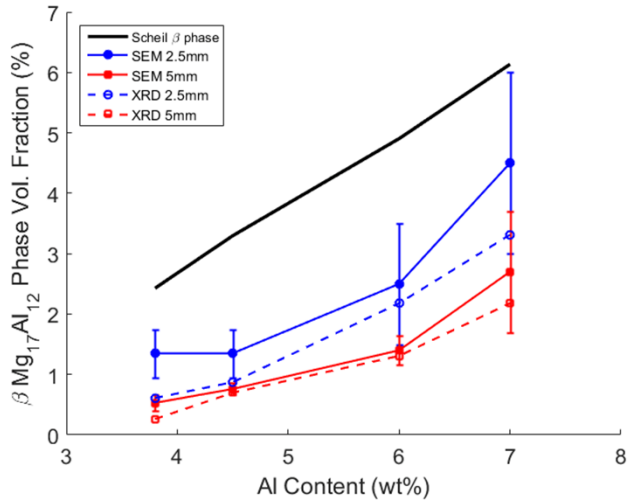

Figure 3.7: β-phase volume fraction versus alloy Al content as measured by SEM (closed symbols) and XRD peak fitting (open symbols). The Scheil curve is a theoretical curve for the β-phase fraction predicted under Scheil solidification conditions using ThermoCalc.

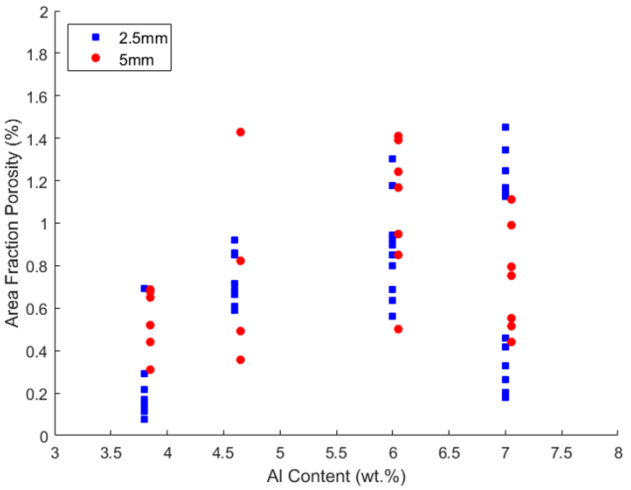

Figure 3.8: Area fraction of porosity measured from at least 5 locations for each condition using SEM back scattered electron (BSE) imaging. There is no statistically significant observable dependence of porosity on Al content or thickness.

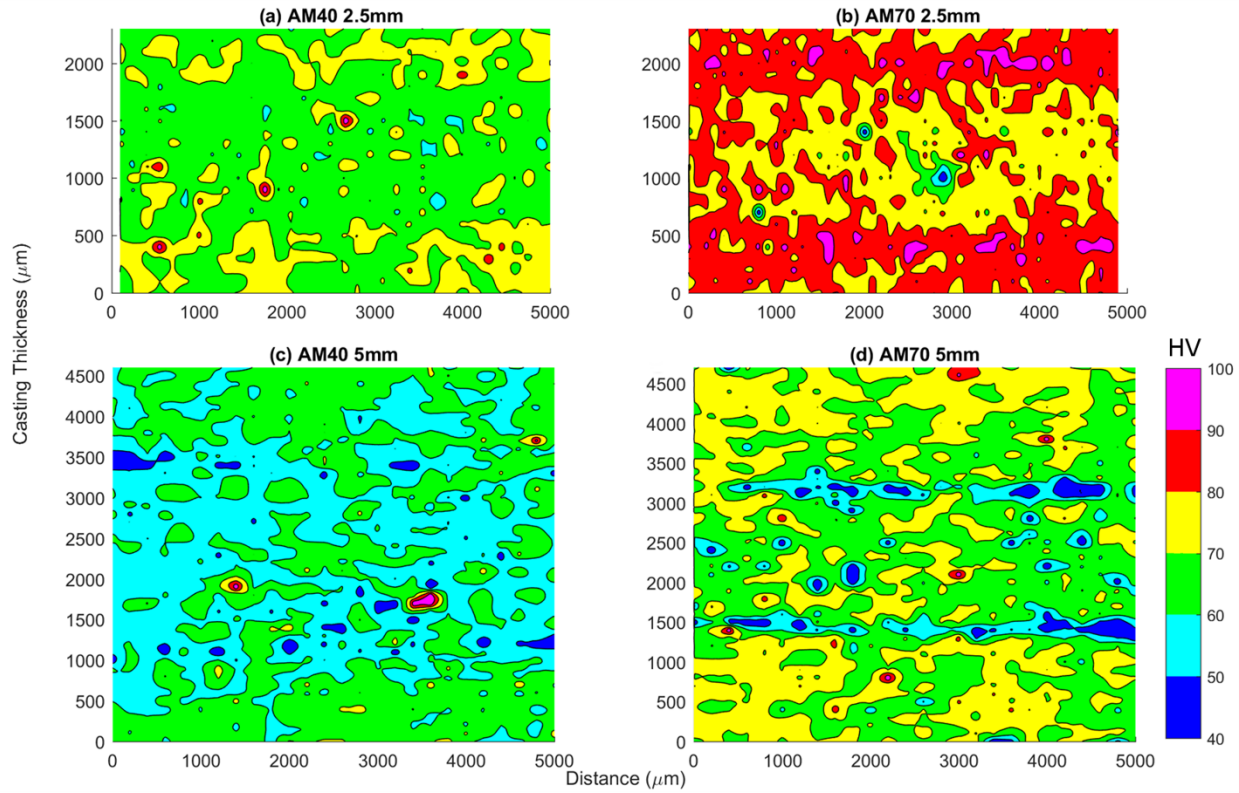

Figure 3.9: Map of Vickers microhardness through the sample thickness for (a) AM40 2.5mm, (b) AM70 2.5mm, (c) AM40 5mm, and (d) AM70 5mm.

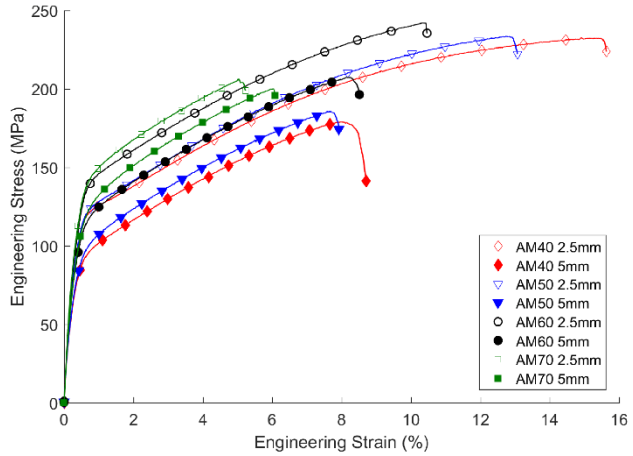

Figure 3.10: Representative tensile curves from each of the eight experimental conditions. 2.5mm plates are shown using open symbols, and the 5mm plates are shown using filled symbols.

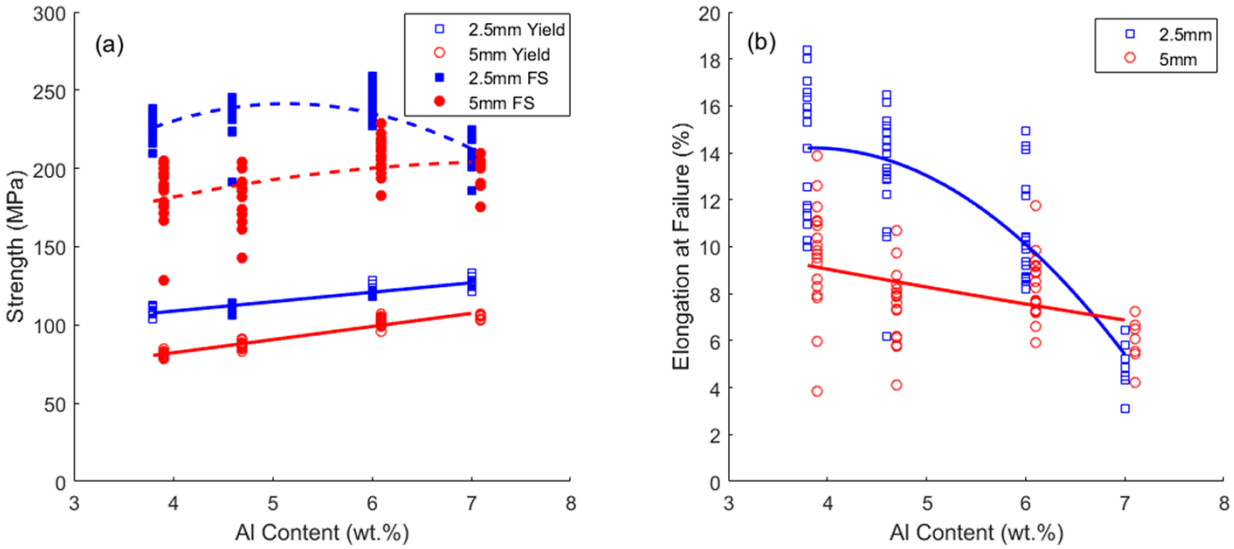

Figure 3.11: (a) Yield strength (solid line) increases with Al content for both the 2.5 and 5mm plates. Fracture strength (dashed line) increases with aluminum content, then decreases as elongation significantly decreases. (b) Elongation decreases with increasing Al content. The effect of aluminum content is more pronounced in the 2.5mm plates.

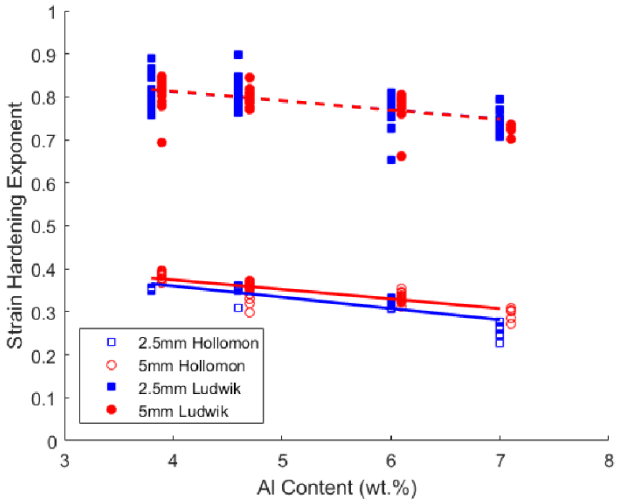

Figure 3.12: Strain hardening exponent decreases for both Ludwik (dashed line) and Hollomon (solid line) constitutive relationships.

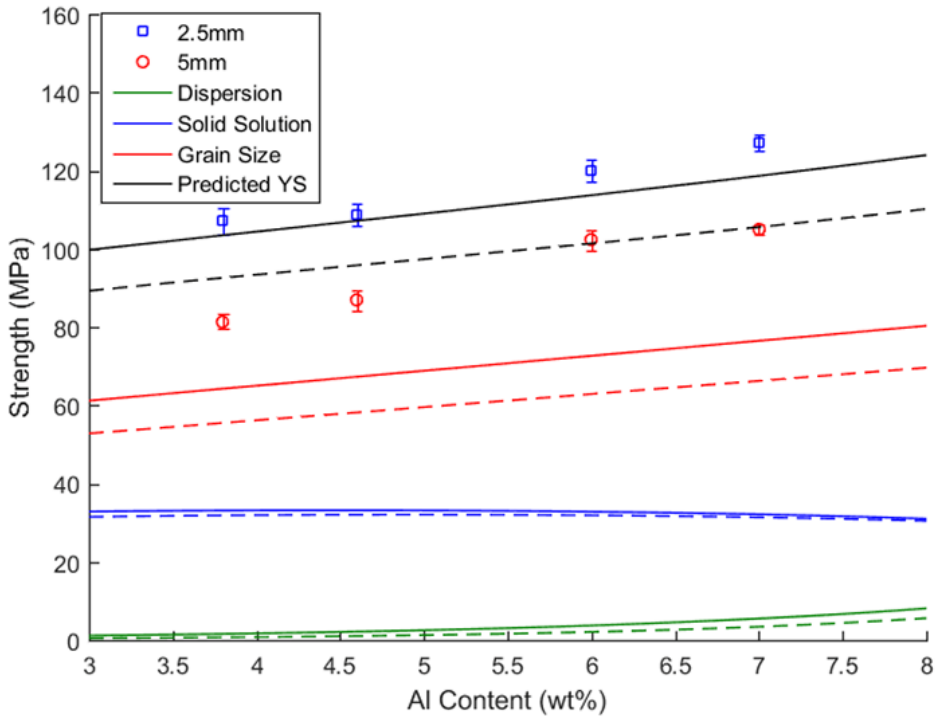

Figure 3.13: The influence of alloy Al content on yield strength. The predicted yield strength from the linear superposition model is compared to the experimental data for both plate thicknesses. Predicted values for the 2.5mm plates are shown using solid lines, and 5mm plates using dashed lines.

Chapter 4

A linear superposition model for predicting the influence of alloy and casting geometry on yield strength of high pressure die cast magnesium alloys

The effect of alloying and precess variables on the yield strength of high pressure die cast Mg alloys is investigated. A range of aluminum content and plate thicknesses were studied in binary Mg-Al and ternary Mg-Al-Mn (AM series) alloys. Solution heat treatment and hot isostatic pressing were used to isolate the effects of β-$Mg_{17}Al_{12}$ phase and shrinkage porosity on the yield strength of AM series castings, and the binary and ternary alloys were compared to determine the effects of Al and Mn on solid solution strengthening. It is found that the yield strength is independent of Al content after either solution treatment or hot isostatic pressing. Microtensile testing was utilized to determine the difference in the yield strength between the skin and the core of castings, and validated the use of a skin/core composite yield strength model. These results are well predicted by a linear superposition model for yield strength. We conclude that yield strength is primarily controlled by grain size distribution and the influence that solutes have on the locking parameter, k_y in the Hall-Petch relationship.

4.1 Introduction

High Pressure Die Cast (HPDC) Mg alloys are frequently used as important elements in weight reduction strategies for automotive applications [1,2]. This is due to their high specific

strength and low density relative to Al and steels. The most common method of manufacturing production parts is HPDC [3]. HPDC generates a broad distribution of microstructural features dependent on casting process variables such as gating structure and flow patterns of the molten metal. These features can have a strong effect on the local mechanical properties, which affect the component level behaviors [4]. The local yield strength can vary up to 40 MPa between different locations in the same casting [5]. In the absence of methods for predicting these location dependent mechanical properties, this variability can significantly limit the usage of Mg alloy parts in production [6].

Yield strength has been shown to depend on local microstructural features [7,26]. The turbulent flow process associated with HPDC can strongly impact the yield strength. This is due to the generation of inhomogeneous microstructures, such as grain size and β-phase, which vary with location within a casting and through the thickness of the part. Previous work in HPDC materials shows the formation of a skin and core microstructure through the thickness of the part [8,9, 26]. A uniform, fine-grain structure forms adjacent to the surface of the casting and is identified as the skin; a bimodal grain structure forms in the interior region and is identified as the core [10, 26]. The core microstructure consists of fine α-Mg grains and externally solidified crystals (ESCs), which are large, dendritic α-Mg grains that form in the shot sleeve. This formation of a fine grained skin at the surface is predicted to improve both yield strength and ductility [6,7,11, 26], but these predictions have not previously been validated. In addition, near the α-Mg grain boundaries, there is a eutectic Al-rich Mg solid solution, and the precipitation of β-$Mg_{17}Al_{12}$ eutectic phase [12–14]. These eutectic phases are predicted to affect the work hardening behavior and the ductility in these alloys [15].

Yield strength models have been developed for die cast Mg alloys [7,16,17, 26]. In these linear-superposition models, yield strength is predicted to be a function of solid solution, grain size, and composite hardening [26] (sometimes referred to as dispersion hardening [18]) due to the presence of the high modulus β-phase in the lower modulus α-Mg matrix.. In order to account for the variation in microstructure through the thickness of the plate, the material is treated as a composite material comprised of a skin and a core region [7]. This separation is based on the changes observed in grain size, solute content, and secondary phase formation through the plate thickness.

A linear superposition model has previously been proposed [26]. In the present study, in order to validate predictions from this model, a broad range of alloying and processing are used to quantify the influence of different microstructural features. Solid solution strengthening effects are characterized by comparing binary Mg-Al and ternary Mg-Al-Mn alloys. Mn is typically added to Mg die castings to remove Fe from the melt and improve corrosion resistance [19]. Mn has been predicted to be a potent solid solution strengthening factor in Mg, but low solubility limits its use for that purpose [20]. Heat treatment is only recently applicable to die cast alloys due to refinements in the casting process such as so-called super vacuum die casting which reduces the level of porosity [21], allowing castings to be heat treated without blistering or hot cracking. Solution treatment results in the dissolution of the β-phase. By using solution heat treatment, the effects of the eutectic β-phase can be isolated by comparing the mechanical properties of the as cast material to the solution treated.

Hot isostatic pressing (HIP) is used to densify the castings, by compressing and "welding" the vacuum filled shrinkage porosity associated with the high cooling rates in HPDC parts. There are relatively few investigations into the effects of HIP on the microstructure and tensile properties

of Mg die castings [22–24], but it has been shown that shrinkage porosity can be significantly reduced by HIP. In addition, the fraction of β-phase is significantly reduced due to pressing near the solution treatment temperature. Using HIP, the combined effects of shrinkage porosity and eutectic dissolution on yield strength can be quantified.

The yield strength of the core has previously been shown to be lower than the bulk using microtensile testing [25]. These microtensile tests have not yet been conducted for the skin however. In order to quantify the difference between the skin and core, microtensile samples were machined from each region of the plate castings. By isolating these metallurgical variables and comparing the effects of each on the model parameters, we can use grain size, solute segregation and eutectic phases to predict the overall yield strength using a linear superposition model.

4.2 Experimental

Mg-Al-Mn alloy (AM series magnesium alloys) plates were super vacuum die cast by Ford Research and Innovation Center at MagTech Corporation. Complete details on the casting process can be found in ref. [26]. Plates of dimensions 305mm x 130mm (12 inch x 5 inch) were cast in two thicknesses, 2.5 and 5mm, and four Al alloy compositions with a nominally constant Mn content. In addition, four binary Mg-Al plates were also cast using the same casting procedure. These have nominal Al composition of 3, 5, 9 and 12 wt.%. All nominal casting compositions are listed in Table 4.1, as measured by optical emissions spectroscopy, including those elements with a composition greater than 0.1 wt.%.

Solution heat treatment (ST) and hot isostatic pressing (HIP) were used to isolate various microstructural features in the AM series plates. Solution heat treatment was conducted in a Carbolite open-air box furnace for 2.25 hours at 413°C. Temperature was monitored every 10

seconds using a J-type thermocouple embedded in a sample, accurate to ±2°C. Solution treated samples were water quenched. HIP was completed at Bodycote in Princeton, KY in a 17" diameter chamber. Plates were processed for 2.25 hours at 410°C and 100 MPa. Argon gas was used to achieve the isostatic pressure at temperature and samples subject to this HIP process did not exhibit any oxidation. Plates were laid flat for processing in order to prevent creep and distortion during heating and cooling processes. Temperature was monitored using thermocouples placed radially and vertically in the chamber. The chamber had a heat up time of 1 hour and plates were furnace cooled due to the depressurization process of the chamber used for HIP. The furnace cooling occurred at a rate of approximately 0.1°C/s.

Tensile specimens with a gage length of 25.4 mm and a width of 6.4 mm were machined from the as- cast plates in accordance to ASTM E8/B557. The specimen thickness was equal to the plate thickness, 2.5 or 5mm and samples were tested with the cast surface present on both parallel surfaces. Tensile testing was completed for at least 27 samples per condition, with ten tensile bars machined from each plate, at least 12 mm from the plate edge. Tensile testing was conducted on a hydraulic MTS load frame with a 25mm extensometer at room temperature. Tests were conducted at an initial strain rate of 1×10^{-3} s^{-1}, and a constant displacement rate of 2 mm/min until sample failure. These tests were used to analyze yield strength, ductility, and strain hardening exponent.

Microtensile dogbone-shaped specimens were cut to the dimensions shown in Figure 4.1 with electrical discharge machining (EDM) from the center of the plates, parallel to the casting flow direction. Specimens had a nominal gauge length of 18 mm and width of 4.4 mm. The specimens were fabricated by wire EDM into slices approximately 800 μm thick through the thickness of the plate as shown in Figure 4.1. Specimens were ground to a final thickness of

approximately 400 $\pm$ 100 μm with a 1 μm mirror finish on one side. If samples were from the skin, the casting surface was left in the as cast condition. Microtensile testing was conducted on a Kammrath and Weiss tensile stage. Load was monitored using a 5 kN load cell, and displacement with an LVDT sensor with a resolution of 1 μm. A nominal strain rate of 5 x 10^{-4} s^{-1} at a constant displacement of 0.6 mm/min (10 μm/sec) was used for all samples. Strain was approximated using the bulk displacement measured using the LVDT.

Metallographic specimens were prepared from the grip section of the tensile specimens, polished to a 1 μm finish, and etched using a 5°C acetic nitric etchant. Scanning electron microscopy was used to measure the porosity area fraction, eutectic phase fraction, and grain size, using secondary electron imaging and electron backscatter diffraction respectively. Electron probe microanalysis was used to quantify the solute concentration through the thickness of the plates. Full details on microstructure quantification and microhardness mapping procedures can be found in previous work [26]. All data generated for this paper is archived on Materials Commons.

4.3 Results

4.3.1 Microstructure Quantification

The microstructural features quantified in this study include the grain size, eutectic phase fraction, and porosity levels for each of the processing conditions, through the plate thickness. In addition, solute content was quantified for each alloy. The processing conditions are denoted as-cast (AC), solution treated (ST) and hot isostatically pressed (HIP).

Grain Size and Skin Thickness

The grain size is quantified for representative samples from each processing condition using EBSD. Due to the high pressure die casting process, a bimodal microstructure is observed.

This grain structure is composed of fine α-Mg grains, and large, dendritic externally solidified crystals (ESCs). ESCs are generally significantly larger than in-mold grains and have a distinctive dendritic shape. In order to account for this distribution in grain size, grains are separated into two groups – α-Mg grains, and ESCs, which are defined operationally to be those dendritic α-Mg grains are greater than 30 μm in diameter. It has been found previously that in these HPDC AM series alloys there is no change in area average in-mold or ESC grain diameter with increasing Al content. This was confirmed in the current investigation by characterizing grain sizes in the low and high Al content alloys for each condition and by comparing the grain size distribution for AM40 and AM70 in each processing condition.

The area average grain diameter in the skin and the core can be compared for each processing condition, as well as for the binary Mg-Al alloys. This data is summarized in Table 4.2. After ST, it is observed that the area average of the in-mold α-Mg grains slightly increases, by 1-2 μm. This increase is statistically significant, with a t-test at the 1% significance level showing an increase in the mean from the as-cast condition to both the ST and HIP. The grain size in the ST and HIP are not statistically significantly different from each other, with a sample size greater than 1500 grains. This is shown graphically in Figure 4.2, where the peak shift to the right can be observed, indicating an increase in the average grain size. This increase is the same for both the ST and HIP processing conditions. This change in grain size can also be seen in Figure 4.3, which has examples from the AM70 2.5mm plates in the as-cast, ST and HIP conditions. It is observed that the binary alloys tend to have a finer grain size than the AM series, with an average of approximately 10 μm in diameter. The in-mold α-Mg peak is much sharper in the binary plates compared with the grain size distribution in the AM series plates. There is a change in grain size with Al content in the binary Mg-Al alloys. A decrease in grain size with increased Al content is

observed from Mg-3Al to Mg-12Al. This difference is less than 2 μm in diameter and within statistical error so an average grain size of 8 μm is used in further analysis for all compositions.

In addition, there is an increase of 20-40 μm in the ESC area average grain diameter after ST and HIP, compared with the as-cast conditions. An increase in the overall area fraction of ESCs is also observed, which is consistent with an increased diameter when considering these large grains. There does not appear to be in an increase in the total number of ESCs, but an increase in the average diameter as observed by the peak shift for the grain data from the core of the plates.

Skin thickness is observed to remain the same for all processing conditions, based on through thickness EBSD scans indicating a similar location threshold for the first observation of ESCs as a function of distance from the casting surface. This skin thickness is 600 μm for the 2.5mm plates, and 1100 μm for the 5mm plates, which correlates with a relative area fraction of 0.45 in both conditions. No change in skin thickness is observed in the ST and HIP conditions. A similar trend is observed in the binary plates, and a constant skin fraction is assumed.

Eutectic phases

The primary eutectic phases in AM series alloys are the β-$Mg_{17}Al_{12}$ phase (light grey) (referred to as the β phase hereafter) and AlMn intermetallic phases (white), shown in Figure 4.4. The β-phase tends to form at the grain boundaries, while the AlMn phases are evenly dispersed. AlMn is the first to solidify due to the high melting point, and are evenly dispersed in the molten metal. This results in a homogenous distribution through the thickness. AlMn particles were substantially reduced in the binary alloys due to the very low Mn content.

After solution treatment, the β-phase is fully dissolved. No change was observed in the AlMn particles. Two morphologies of AlMn particles were observed –fine flower shaped particles,

and larger faceted particles. After HIP, a small area fraction of β-phase remains. The β-phase is observed as fine particles along the grain boundaries. The amount of eutectic phases overall is significantly less in the HIP conditions, especially in the core regions. The β-phase fraction in each of these conditions is quantified in Figure 4.5. The β-phase fraction in the binary Mg-Al and AM series alloys follows the same trend regardless of Mn content. Data from both the binary and the AM series are used in constructing a best fit line for the β-phase fraction as a function of Al alloy content in the as-cast condition.

Solute content

The amount of solute in solid solution was quantified using electron probe microanalysis (EPMA) for Al and Mn for all relevant conditions. The solute fraction was quantified separately for both the skin and core regions. The skin for this purpose is defined as the first 300 μm adjacent to the casting surface. The amount of solute in solid solution is assumed to be similar for both the ST and HIP conditions, based on use of the same temperature and duration for processing. This was validated on the AM70 conditions and it was observed that there is no statistically significant difference between the AM70 ST and HIP conditions. Based on this, the same solute fraction measurements from the ST plates are used for the HIP conditions in development of the strength model.

The amount of Al in solid solution is observed to be higher in the skin than in the core, shown in Figure 4.6(a) and (b). The increased Al content in the skin remains increased after heat treatment in the 2.5mm plates, but not in the 5mm. After heat treatment, there is an increase in the amount of solute measured in both the skin and the core. The amount of Al in solid solution in the binary plates follows the same trend as the as-cast AM series plates. Data for the binary plates in

the as-cast condition are overlaid with the AM series, and show the same dependence of Al solute content on Al alloy content.

In the AM series plates, there is a decrease in Mn solute content with Al alloy content, shown in Figure 4.6(c). There is no change in this decrease with plate thickness, or with heat treatment. There is also no change with location in the near edge or center. The amount of Mn in the binary plates is less than 0.11 Wt.% for all conditions. Based on these measurements, the Mn was not considered significant for the binary alloys and thus was not taken into account for calculation of solute effects on strength.

There is assumed to be no variation in porosity levels with Al content. After ST, there is no change in the overall area fraction of porosity. Slightly less porosity was observed in the binary alloys compared to the as-cast AM series alloys. The amount of porosity is significantly reduced after HIP.

4.3.2 Mechanical Properties

Microhardness mapping

Microhardness mapping was completed for the AM70 as-cast and HIP conditions in both the 2.5 and 5mm thicknesses, Figure 4.7. The skin thickness is comparable, with a high hardness band near the casting surface in both the as-cast and HIP conditions. Based on these maps and the grain size data, the high hardness band is 600 μm in the 2.5mm castings and 1100 μm thick in the 5mm castings.

The range of hardness values observed in the HIP condition is smaller than in the as-cast plates. This is due to the increase in grain size after HIP, which results in a lower hardness, and the reduction of the porosity, removing the very low hardness regions. Based on the EBSD results,

the ST hardness map is assumed to be a composite of the as-cast and HIP, in that it would have a similar hardness as the HIP, with the inclusion of the porosity bands.

Tensile Testing

The tensile properties have been characterized for each condition. Representative curves for the extreme Al contents are shown in Figure 4.8(a) and (b) for the 2.5mm plates. The 5mm plates show the same trends. Stress strain curves for the Mg-Al binary alloys follow the same trends as the AM series in the as-cast condition, showing an increase in the yield strength, and a decrease in the overall elongation with increasing Al content. In the current work, only the yield strengths are discussed in detail. Yield strength is measured using the 0.2% offset method. This data is summarized in Table 4.3 and Table 4.4.

In general, there is an increase in yield strength with increasing Al content in the as cast condition for both the 2.5 and 5mm thick plates for both the binary and AM series alloys. The trends in the yield strength are shown in Figure 4.9. There is an increase in yield strength of 7 MPa per wt.% Al in the 2.5mm AM series and binary alloys. The yield strength is lower in the 5mm thick plates in the as cast condition by about 15 MPa for both the AM series and binary alloys, but follows a similar increase of 8.5 MPa per wt.% Al in the 5mm plates. There is a decrease in the intrinsic strength from 85 MPa in the 2.5mm plates to 60 MPa in the 5mm plates.

After solution treatment, it is observed that there is no variation in yield strength with the alloy Al content. The yield strength is on average 112 MPa for the ST condition in the 2.5mm thick plates, and 98 MPa in the 5mm thick plates. HIP also removes the variation with Al content. There is no change in yield strength with Al content after HIP, and the yield strength is observed to be 120 MPa in the 2.5mm thick plates and 109 MPa in the 5mm thick plates. In general, the difference

between the ST and HIP plates is approximately 10 MPa in the 2.5mm and the 5mm plates, with HIP conditions exhibiting approximately a 10% increase in yield strength.

Microtensile Testing

Microtensile samples were prepared from AM70 5mm plates for the as-cast conditions. These samples were excised from the skin and the core of the plates. Skin samples were left with the casting surface intact on one side, in order to measure the effect of the die cast skin. In general, measured yield strengths from the microtensile tests were less than that of the standard tensile yield strength. They tended to be lower, due to the high compliance levels in the stage, inaccuracies in the LVDT displacement measurements. Therefore, these yield strengths should not be considered absolute, but rather a representation of relative differences between the skin and core regions. The skin had a nominal yield strength of 105 MPa, and the core a yield strength of 84 MPa, shown in the stress-apparent strain curves in Figure 4.10.

4.4 Discussion

4.4.1 Microstructure

By processing the plates from the as-cast condition, the β-phase and shrinkage porosity were controlled to evaluate their effects on the tensile behavior. After ST, the β-phase is fully dissolved, and after HIP, the porosity is fused. The effects of ST and HIP on the grain size, β-phase, and solute content are quantified. Grain size is an important microstructural variable in HPDC Mg alloys. In this work the effect that alloying has on the grain size was quantified for both the binary and AM series castings. In the AM series alloys, it has previously been observed that there is no change in grain size with Al content [26]. In the binary Mg-Al alloys it is found that there is a decrease in grain size with increasing Al content, which is consistent with previous work [8,27]. We attribute this decrease in grain size with increasing Al content to the decrease in

liquidus temperature with increasing Al content [28]. In other words, in the low Al alloys solidification begins at higher temperatures during the casting process, and thus the area fraction of ESCs is larger. This difference is not observed in the AM series, presumably due to the much smaller range of Al contents. Even using Al contents from 3 to 12 wt.% Al, there is only an associated decrease of 2 μm in area average grain diameter. This is comparable with previous work which shows the effects of Al solutes as a growth restriction factor in Mg alloys [29,30]. The relative difference between the grain sizes in the binary and AM series alloys is likely specific to changes in the casting process.

After processing, there are subtle changes in grain size in both the ST and HP conditions. While the average in-mold grain size is not significantly affected, there is a broadening in the grain size distribution and a slight shift in the peak for the HIP and ST conditions, as shown in Figure 4.2. This is consistent with previous work studying the effect of ST in AZ91 castings, where grain growth was observed after solution treatment [31]. There is no statistically significant difference between the ST and HIP conditions, confirming that there is no additional change in grain size with the added pressure in HIP. This slight increase in α-Mg area average grain diameter can be attributed to the solution heat treatment process, and the dissolution of the β-phase at the grain boundaries. Due to the limited duration of solution heat treatment to that necessary to dissolve the β-phase, there are minimal changes to the grain size, allowing comparison with the as cast mechanical properties There is limited work with which to compare the effects of ST on grain size in die cast Mg alloys [32–35], and no previous work on the effect of HIP [36–38]. This dissolution of the β-phase leads to a more regular grain shape, and a slight increase in the overall α-Mg grain size.

The skin thickness is quantified for all conditions using a combination of thickness of the uniform grain size band at the casting surface, and microhardness mapping. For both the as-cast and HIP conditions, microhardness shows a band of increased hardness at the surface, though the effect is weakened after HIP. Both suggest a skin thickness of 600 μm for the 2.5mm plates, and 1100 μm for the 5mm plates in all processing conditions. This leads to a skin fraction of 0.45 for all conditions.

The β-phase structure is also quantified with processing and alloy composition. There is no change in the overall eutectic phase fraction between the AM series alloys and the binary alloys. As shown in Figure 4.5, the eutectic area fraction remains nominally linear for both the AM series and binary alloys, so they are treated as the same for all plates in the as-cast condition. After ST, the β-phase is fully dissolved. The only remaining secondary phases are the AlMn eutectic phases, shown in Figure 4.4. HIP processing results in fine precipitation of β-phase particles along the grain boundaries, Figure 4.4. This is due to the effects of furnace cooling that occurs following the HIP process, in which the slow cooling rate results in fine precipitation of β-phase particles along the grain boundaries, as cooling rate can significantly impact β-phase formation [39]. This has been observed previously in AZ91 die castings, where the slow cooling process after HIP results in precipitation of the β-phase [24]. This precipitation of β-phase was replicated by solution treating samples from the one plate for the same temperature and duration, and comparing the results of a water quench with a furnace cool. Without quenching the samples after solution treatment, precipitation of solute elements is observed. This confirms that the slow cooling process of nominally 0.1°K/s is responsible for the fine precipitates in the HIP condition. That is much slower than the cooling rate associated with HPDC of over 100 K/s, and similar for a water quench [40,41].

Solute content in each location is measured for each condition. The solute content in both the skin and the core increases with Al content for both the AM series and binary Mg-Al samples. This shows that the addition of Mn does not affect the amount of Al which remains in solid solution. The same trend is observed for all as-cast alloys, and as such are plotted together in Figure 4.6 (a) and (b). In the AM series, there is no change in the Mn solute content with location or plate thickness, Figure 4.6(c). This is as expected with the high melting temperature of Mn relative to Al and Mg, resulting in early solidification of AlMn eutectic phases [42]. The amount of Al in solid solution is higher in the skin than in the core, which has also been observed previously in AZ91 [43]. This change in Al with distance from the surface is likely due to solute trapping associated with the faster solidification with contact to the cold die walls [44]. The Al solute content in the 5mm overall is lower than in the 2.5mm. This variation is consistent in both the binary and the AM series alloys, and is likely due to the changes in cooling rate between the two plates.

After ST and HIP, redistribution of Al content was observed. The difference between the skin and the core is 0.7 to 2 wt.% Al with increasing alloy Al content, which is less than that in the as-cast condition of 1 to 4 wt.% Al. In addition, Al rich regions within the α-Mg grains are no longer observed after heat treatment. Due to the fine grain size in these alloys, this difference between the as cast and ST samples cannot be directly measured, but is inferred from EPMA measurements taken by traversing across ESCs by Berman [44]. These composition profiles indicated that there is a change in solute content across ESCs with the center of these grains having lower Al contents than the grain boundaries. Microsegregation of Al across α-Mg grains has previously been shown to occur [45], and is assumed to be the case in the as-cast condition of the present investigation.

4.4.2 Tensile behavior

Overall there are some substantial changes in the tensile behavior that occur after processing. In the as-cast condition, there is an increase in yield strength with Al content, which is consistent with observations from many previous studies [7,26,46,47]. This increase with Al content is similar in both the binary Mg-Al and ternary AM series alloys. Previous work in binary Mg-Al alloys has shown grain size and solid solution strengthening to be the primary factors influencing yield strength [26, 47]. There is an increase in yield strength in the binary Mg-Al alloys relative to the AM series. This increase in yield strength in the as-cast condition is attributed to the finer grain size and decrease in ESC fraction observed in the binary alloys. The finer grain size accounts for an increase in strength of approximately 20 MPa. It is observed that with increasing section thickness, the yield strength tends to decrease. There is some disagreement in previous investigations about the impact of section thickness on the yield strength, where in some studies it remains nominally constant and in others decreases. [25,48–50]. It is consistently observed in the alloys tested in this work, that the 5mm plates have a lower yield strength than the 2.5mm plates. This is attributed to the increase in ESC fraction and α-Mg area average grain size, as detailed previously.

The use of microtensile testing of samples extracted from both the sample skin and core was useful in validating the concept that the fine grained skin region had higher strength compared to the core. In the current work the yield strength of the skin regions was approximately 20 MPa higher compared to the core region. This can be attributed to the smaller average grain size in the skin region and the low ESC fractions as noted in Table 4.2. Previously the only reported results on through thickness variation in yield strength of castings have been done by the removal of the skin which allowed characterization of the yield strength of the core only [25]. This resulted in a

decrease of 25 MPa of the yield strength in a die cast AZ91 alloy, consistent with the differences observed in these alloys.

After ST and HIP, the influence of Al alloy content on yield strength is minimal. This has not been observed previously in Mg alloys. Previous work on the effects of heat treatment on yield strength of HPDC Mg have been focused primarily on AZ91, and one study on AM series castings [51–53]. It has been reported that after ST, the yield strength decreases in AZ91, which is attributed to the increase in grain size [52]. In the current study, a similar decrease in strength after ST is observed for the AM70 condition however no change in grain size was observed. This is in contrast to the AM40 samples, which show an increase in yield strength with ST. Across the alloy compositions from 3.8 to 7 Wt.% Al in AM alloys, after solution treatment, the yield strength appears independent of Al concentration. This is discussed in more detail in section 4.3, however we attribute this to the redistribution of solute in the matrix and its influence on solid solution strengthening and the Hall-Petch locking parameter.

Similar trends are observed after HIP in the AM series alloys, where there is an overall increase in yield strength compared to the solution treated conditions. As observed in the solution treated condition, the yield strength in the HIP condition is independent of Al content. This general increase in yield strength in the HIP condition compared to the ST condition may be attributed to a reduction in porosity, or a slight increase in the effects of dispersion strengthening. Using vacuum pressure to reduce porosity during the casting process of AZ91 has previously been reported to increase the yield strength slightly [52]. In the current investigation, the low levels of porosity that were observed in the SVDC castings should minimize the relative change in effective cross sectional area, and any resulting effects on yield strength. Porosity in these castings ranges from 1-2% area fraction, and an effective reduction of 2% in the cross sectional area would be expected

to result in a 5 MPa increase in yield strength. There is no change in average plate thickness after HIP, so it would have to be treated as a change in density, and a reduction in the effective cross sectional area in the AC and ST conditions, with the HIP as considered to be fully densified. More likely is the effect of solute diffusion and precipitation along the grain boundaries, resulting in an increase in strength of the boundaries.

4.4.3 Validating the yield strength model

Grain size, β-phase, and solute distribution have all been shown to play an important role in determining the yield strength of Mg alloys [7,16,18, 26]. By varying the microstructure using HIP and ST, we have varied these features independently to ascertain the relative effects of each of these microstructural features. This resulting quantitative microstructure and yield strength information has provided a means to validate the components of a linear superposition yield strength model previously proposed by the authors [26]. Using this linear superposition model (Equation 4.1) the individual components of grain size σ_{gb}, solid solution σ_{ss}, and composite strengthening σ_{comp} are accounted for. Each of these microstructural features is quantified for the skin and the core, and are combined using a composite model shown in Equation 4.2.

[4.1] $\sigma_y = \sigma_{gb} + \sigma_{ss} + \sigma_{comp} =$

$$\left(m * \sum M_x c_x^{\frac{1}{2}}\right) + \sigma_0 + \left[f_{ESC} * \left(\mathrm{k_y} * \mathrm{d}_{\mathrm{ESC}}^{-\frac{1}{2}}\right) + (1 - f_{ESC}) * \left(\mathrm{k_y} * \mathrm{d}_{\mathrm{in-mold}}^{-\frac{1}{2}}\right)\right] +$$

$(135 * f_{beta})$

[4.2] $\sigma_{y_{total}} = f_{skin}\sigma_{y_{skin}} + (1 - f_{skin})\sigma_{y_{core}}$

A best fit trend line for the β-phase fraction, solute concentration of Al and Mn, and grain size of α-Mg and ESCs are found for the skin and the core. The area fraction of skin used is 0.45

for all conditions. The constants used in Equations 4.1 and 4.2 are summarized in Table 4.5. These fits are used in Equation 4.1 to predict the effects of processing on the yield strength. By comparing the as -cast AM series with the binary Mg-Al, we can isolate the effects of the Al and Mn solute contributions to the solid solution strengthening component. ST results in the removal of the dispersion hardening component and allows quantification of the relative impact of the β-phase. HIP results in the weakening of the dispersion and grain size hardening components, and allows determination of the nominal effect porosity has on the yield strength.

The strongest factor influencing the yield strength dependence on Al content in the as-cast condition is the locking parameter, k_y. The locking parameter has been shown to be affected by alloying in multiple alloys of different crystal structures [18,54,55]. The locking parameter is a means of quantifying the effect of solute atoms on the grain size effect. In the case of the as-cast condition, it appears to be capturing the concentration of Al near the grain boundaries in these alloys, which adds resistance to dislocation flow through the grain boundaries. In both the binary Mg-Al and ternary Mg-Al-Mn alloys, a linear increase in yield strength was observed as Al content was increased. This appears to confirm our previous hypothesis [26] that Mn does not have a significant effect on k_y. This is again due to the formation of AlMn particles during casting and the random distribution of Mn through the matrix compared to the enrichment of Al solute atoms near the grain boundaries.

[4.3] $k_y = k_{y,Mg} + \sum c_x \Delta k_{y,x}$

The binary alloys are significantly stronger than the AM series alloys. This is attributed to changes in the grain size observed in the binary alloys compared with the AM series alloys. The grain size is much finer in the binary alloys, with a smaller ESC fraction compared to the AM

series alloys. The yield strength is predicted using a constant grain size, independent of Al content. The Mg-3Al is slightly over predicted, while the Mg-12 is slightly under predicted using an average grain size due to grain refinement with increasing Al content [27,56]. The effect of solid solution is lower in the binary alloys than the AM series. This is due to the removal of Mn, which is a very potent solid solution strengthener based on work by Yasi et al. [20]. The fraction of strengthening contributed in the Mg-Al by solid solution is 20%, which is lower than the 30% contributed by solid solution in the AM series.

The difference in yield strength between the skin and the core was qualitatively confirmed from the results from the microtensile tests conducted in each region. Based on the predicted grain sizes, solid solution and composite strengthening in each region, we would expect an increase of 15 MPa in the predicted strengths from the core to the skin. This matches well with the observed differences in the yield strengths measured using the microtensile tests of 20 MPa (Figure 4.10). Predictions of the relative yield strength of the skin and core of 5mm AM samples are provided in Figure 4.12 and compared with the results of tensile from the as-cast samples. The combined strength of the skin-core is predicted, and shown in the dotted line. The combined prediction matches well with the experimental values. The core of the 5mm plates has more weight due to the skin fraction and large ESC volume fraction.

The effects of ST and HIP are less well defined by this model however. After ST and HIP, there is no dependence of yield strength on Al. When using the k_y defined in Equation 4.3, the predicted yield strength is much lower the measured value, especially in the lower Al contents. It appears that yield strength is actually independent of Al and a constant value of $k_y = 0.34$ independent of alloy content results in the best fit of the yield strength in the ST condition. This is potentially due to the homogenization of the solute through the matrix, with the removal of Al

enrichment at the grain boundaries. When applying a constant value of $k_y = 0.34$ to the HIP condition, the yield strength is still severely under predicted. The model assumes an approximate defect level in the castings, which means that after HIP we have a densified material with minimized porosity. Currently the model assumes some intrinsic defect level, resulting in an under prediction of the HIP behavior. If a reduced cross sectional area is used, an increase in the yield strength is expected. By reducing the effective cross sectional area by 2%, the predicted yield strength increases by approximately 5 MPa, which accounts for some of the strength increase with HIP. The low corrosion resistance of HPDC Mg-Al-X alloys has been attributed to the presence of β-phase at grain boundaries, and the difference in corrosion potential [57,58]. Since the solution treatment eliminates this phase and has only a modest effect on yield strength SVDC coupled with solution treatment may be an effective way to improve corrosion and maintain strength levels.

4.5 Conclusions

In this study we have quantitatively characterized local microstructures, composition and yield strengths of a wide range of Mg-Al and Mg-Al-Mn alloys in high pressure die cast samples. Increasing Al content leads to increasing strength. The effects of ST and HIP on the grain size, β-phase formation, and solute redistribution have been quantified, as well as the bulk tensile properties. It is observed that after either solution treatment or HIP, yield strengths are independent of alloy Al content. This is attributed to the homogenization of the local microstructure which reduces or eliminates the solute rich regions near the grain boundaries. Yield strength was not significantly reduced by solution treatment.

The quantitative microstructures determined in this study were used to validate a linear superposition model for strength that considers solute content, grain size and β-phase content. The model also accounts for the differences in these metallurgical variables that exist between the die

casting skin and its core regions. This composite, skin-core linear superposition model accurately predicts the influence of alloy content and casting thickness on the measured yield strength. The linear superposition model is further validated by predicting the results of both solution treatment and hot isostatic pressing on yield strengths of the Mg-Al-Mn binary alloys.

Acknowledgements:

The authors are grateful to Xin Sun, Mei Li, and Joy Forsmark for many helpful discussions. Thanks to Larry Godlewski and Jacob Zindel at Ford Motor Company for providing the SVDC cast plates. Thanks to Mason Bennett for assistance in metallographic preparation and analysis. The authors gratefully acknowledge funding for this project from the Department of Energy Office of Vehicle Technologies under the Automotive Lightweighting Materials Program managed by Dr. Will Joost, via subcontract with Pacific Northwest National Laboratory. The use of the Materials Commons to archive the data presented in this paper is appreciated. Funding for Materials Commons is from the U.S. Department of Energy, Office of Basic Energy Sciences, Division of Materials Sciences and Engineering under Award #DE-SC0008637 as part of the Center for PRedictive Integrated Structural Materials Science (PRISMS Center) at University of Michigan.

References:

[1] B.L. Mordike and T. Ebert: *Mater. Sci. Eng. A*, 2001, vol. 302, pp. 37–45.
[2] W.J. Joost and P.E. Krajewski: *Scr. Mater.*, 2016, vol. 128, pp. 107–12.
[3] A.A. Luo: *J. Magnes. Alloy.*, 2013, vol. 1, pp. 2–22.
[4] J.H. Forsmark, J.W. Zindel, L. Godlewski, and A. Caliskan: *SAE Int.*, 2012, pp. 2–10.
[5] J.H. Forsmark, J.W. Zindel, L. Godlewski, J. Zheng, J.E. Allison, and M. Li: *Integr. Mater. Manuf. Innov.*, 2015, vol. 4.
[6] R. Alain, T. Lawson, P. Katool, G. Wang, J. Jekl, R. Berkmortel, and L. Miller: *SAE Int.*, 2004, pp. 2004-01–0131.
[7] K.V. Yang, C.H. Cáceres, and M.A. Easton: *Metall. Mater. Trans. A*, 2014, vol. 45, pp. 4117–28.
[8] A.L. Bowles, K. Nogita, M.S. Dargusch, and C.J. Davidson: *Mater. Trans*, 2004, vol. 45, pp. 3114–19.
[9] J.H. Forsmark, Z. Dowling, K. Gibson, C. Mueller, L. Godlewski, J.W. Zindel, and J.M. Boileau: *SAE Int. J. Mater. Manuf.*, 2015, vol. 8.
[10] K. Vanna Yang, M.A. Easton, and C.H. Cáceres: *Mater. Sci. Eng. A*, 2013, vol. 580, pp. 191–95.
[11] K. Vanna Yang, C.H. Cáceres, A.V. Nagasekhar, and M.A. Easton: *Mater. Sci. Eng. A*, 2012, vol. 542, pp. 49–55.
[12] S. Barbagallo, H.I. Laukli, O. Lohne, and E. Cerri: *J. Alloys Compd.*, 2004, vol. 378, pp. 226–32.
[13] M.D. Nave, A.K. Dahle, and D.H. StJohn: in *Magnes. Technol. 2000*, H.I. Kaplan, J. Hryn, and B. Clow, eds., The Minerals, Metals & Materials Society, 2000, pp. 233–42.
[14] M.S. Dargusch, M. Nave, S.D. McDonald, and D.H. StJohn: *J. Alloys Compd.*, 2010, vol. 492, pp. L64–68.
[15] E.I. Barker, K.S. Choi, X. Sun, E. Deda, J. Allison, M. Li, J. Forsmark, J. Zindel, and L. Godlewski: *Comput. Mater. Sci.*, 2014, vol. 92, pp. 353–61.
[16] I. Toda-Caraballo, E.I. Galindo-Nava, and P.E.J. Rivera-Díaz-del-Castillo: *Acta Mater.*, 2014, vol. 75, pp. 287–96.
[17] P. Sharifi, Y. Fan, H.B. Anaraki, A. Banerjee, K. Sadayappan, and J.T. Wood: *Metall. Mater. Trans. A*, 2016.
[18] C.H. Cáceres and D.M. Rovera: *J. Light Met.*, 2001, vol. 1, pp. 151–56.
[19] M.S. Dargusch, K. Pettersen, K. Nogita, M.D. Nave, and G.L. Dunlop: *Mater. Trans.*, 2006, vol. 47, pp. 977–82.
[20] J.A. Yasi, L.G. Hector, and D.R. Trinkle: *Acta Mater.*, 2010, vol. 58, pp. 5704–13.
[21] A. Luo and M.O. Pekguleryuz: *J. Mater. Sci.*, 1994, vol. 29, pp. 5259–71.
[22] M. Ostermeier: Technischen Universität München, 2009.
[23] M. Ostermeier, M. Brummer, and E. Werner: *Int. Foundry Res.*, 2009, vol. 61, pp. 2–7.
[24] Th. Schubert, P. Kumar, and B. Kieback: in *Mg2012 9th Int. Conf. Magnes. Alloy. Their Appl.*, 2012, pp. 1223–28.
[25] W.P. Sequeira, G.L. Dunlop, and M.T. Murray: in *Proc. Third Int. Magnes. Conf.*, 1996, pp. 63–73.
[26] E. Deda, T.D. Berman, and J.E. Allison: *Metall. Mater. Trans. A* Accepted Manuscript.
[27] A.V. Nagasekhar, M.A. Easton, and C.H. Cáceres: *Adv. Eng. Mater.*, 2009, vol. 11, pp. 912–19.
[28] Y. Zhong, M. Yang, and Z.K. Liu: *Calphad*, 2005, vol. 29, pp. 303–11.

[29] D.H. StJohn, M. Qian, M.A. Easton, P. Cao, and Z. Hildebrand: *Metall. Mater. Trans. A*, 2005, vol. 36, pp. 1669–79.
[30] A.V. Nagasekhar, C.H. Cáceres, and M.A. Easton: in *Magnes. Technol. 2010*, 2010, pp. 373–76.
[31] L. Yang, Y. Wei, and L. Hou: *J. Mater. Sci.*, 2010, vol. 45, pp. 3626–34.
[32] H. Yamada, M. Furui, S. Ikeno, Y. Sanpei, K. Sakakibara, and S. Saikawa: *Mater. Sci. Forum*, 2010, vol. 654–656, pp. 679–82.
[33] M. Mokhtarishirazabad, M. Azadi, G. Hossein Farrahi, G. Winter, and W. Eichlseder: *Mater. Sci. Eng. A*, 2013, vol. 588, pp. 357–65.
[34] L. Čížek, M. Greger, L. Pawlica, L.A. Dobrzański, and T. Tański: *J. Mater. Process. Technol.*, 2004, vol. 157–158, pp. 466–71.
[35] K. Sadayappan, W. Kasprzak, Z. Brown, L. Ouimet, and A.A. Luo: *Mater. Sci. Forum*, 2009, vol. 618–619, pp. 381–86.
[36] L.A. Dobrzański, T. Tański, and L. Čížek: *J. Achiev. Mater. Manuf. Eng.*, 2007, vol. 20, pp. 431–34.
[37] J. Miao, M. Li, and J.E. Allison: in *Mg2012 9th Int. Conf. Magnes. Alloy. Their Appl.*, 2012, pp. 493–98.
[38] T. Zhu, Z.W. Chan, and W. Gao: *J. Mater. Eng. Perform.*, 2010, vol. 19, pp. 860–67.
[39] T. Zhu, Z.W. Chen, and W. Gao: *J. Alloys Compd.*, 2010, vol. 501, pp. 291–96.
[40] Hans Ivar Laukli: Norwegian University of Science and Technology, 2004.
[41] M.M. Avedesian and H. Baker, eds.: *ASM Specialty Handbook - Magnesium and Magnesium Alloys*, ASM International, Metals Park, OH, 1999.
[42] V.Y. Gertsman, J. Li, S. Xu, J.P. Thomson, and M. Sahoo: *Metall. Mater. Trans. A*, 2005, vol. 36, pp. 1989–97.
[43] L. Hu, S. Chen, Y. Miao, and Q. Meng: *Appl. Surf. Sci.*, 2012, vol. 261, pp. 851–56.
[44] T.D. Berman: Private communication, 2016.
[45] L.-Y. Wei and R. Warren: *Mater. Sci. Technol.*, 2007, vol. 23, pp. 745–52.
[46] T.K. Aune, H. Westengen, and T. Ruden: *SAE Tech.*, 1993, pp. 51–57.
[47] H. Cao and M. Wessén: *Metall. Mater. Trans. A*, 2004, vol. 35, pp. 309–19.
[48] T. Abbott, M.A. Easton, and W. Song: *Mater. Sci. Forum*, 2003, vol. 419–422, pp. 141–46.
[49] D. Rodrigo, M. T. Murray, and H. Mao: *SAE Int. Congr. Magnes. Sess.*, 1999.
[50] G. Chadha, J.E. Allison, and J.W. Jones: *Metall. Mater. Trans. A*, 2007, vol. 38, pp. 286–97.
[51] A.A. Luo and A.K. Sachdev: *Int. J. Met.*, 2010, pp. 51–60.
[52] X.J. Wang, S.M. Zhu, M.A. Easton, M.A. Gibson, and G. Savage: *Int. J. Cast Met. Res.*, 2014, vol. 27, pp. 161–66.
[53] S. Celotto: *Acta Mater.*, 2000, vol. 48, pp. 1775–87.
[54] C.H. Cáceres, G.E. Mann, and J.R. Griffiths: *Metall. Mater. Trans. A*, 2011, vol. 42, pp. 1950–59.
[55] P. Sharifi, Y. Fan, J.P. Weiler, and J.T. Wood: *J. Alloys Compd.*, 2014, vol. 605, pp. 237–43.
[56] D.H. StJohn, M.A. Easton, M. Qian, and J.A. Taylor: *Metall. Mater. Trans. A*, 2012, vol. 44, pp. 2935–49.
[57] A. Atrens, G. Song, F. Cao, Z. Shi, and P.K. Bowen: *J. Magnes. Alloy.*, 2013.
[58] G. Song, A. Atrens, and M.S. Dargusch: *Corros. Sci.*, 1999, vol. 41, pp. 138–62.

Tables:

	Composition (Wt.%)			
Condition	Al	Mn	Zn	Mg
AM40	3.80	0.55	0	Bal.
AM50	4.60	0.41	0	Bal.
AM60	6.05	0.44	0	Bal.
AM70	7.05	0.44	0	Bal.
Mg-3Al	3.12	0.09	0.06	Bal.
Mg-5Al	4.80	0.09	0.06	Bal.
Mg-9Al	8.99	0.11	0.05	Bal.
Mg-12Al	11.35	0.10	0.11	Bal.

Table 4.1: Composition of each casting condition as measured by optical Emissions spectroscopy.

Condition	α-Mg area average grain diameter skin (μm)	α-Mg area average grain diameter Core (μm)	ESC area average grain diameter skin (μm)	ESC skin area fraction	ESC area average grain diameter core (μm)	ESC area fraction
AM AC 2.5mm	13.3 ± 4	16.9 ± 6	37	0.02	73 ± 22	0.46
AM AC 5mm	16.3 ± 6	16.7 ± 6	73	0.45	73 ± 22	0.52
AM ST 2.5mm	15.5 ± 5	18.0 ± 6	44	0.07	82 ± 26	0.52
AM ST 5mm	17.2 ± 6	19.1 ± 7	39	0.27	113 ± 29	0.64
AM HIP 2.5mm	15.8 ± 5	16.6 ± 6	40	0.07	120 ± 36	0.43
AM HIP 5mm	18.3 ± 7	19.2 ± 7	38	0.31	99 ± 27	0.54
Binary 2.5mm	9.6 ± 3	11.7 ± 4	41	0.06	52 ± 12	0.25
Binary 5mm	10.5 ± 3	14.3 ± 5	32	0.01	51 ± 12	0.35

Table 4.2: Area average grain diameter data for each processing condition. Values have been averaged across Al contents.

Condition	As Cast Yield Strength (MPa)	ST Yield Strength (MPa)	HIP Yield Strength (MPa)
AM40 2.5mm	108.9 ± 3.1	111.8 ± 2.3	117.5 ± 3.4
AM50 2.5mm	109.7 ± 2.6	-	119.3 ± 2.1
AM60 2.5mm	122.1 ± 3.7	-	122.0 ± 2.3
AM70 2.5mm	127.4 ± 3.4	111.7 ± 4.5	124.4 ± 3.8
AM40 5mm	83.7 ± 3.5	95.2 ± 2.3	110.2 ± 1.7
AM50 5mm	87.8 ± 2.9	-	108.6 ± 2.5
AM60 5mm	103.1 ± 2.5	-	110.5 ± 2.9
AM70 5mm	109.3 ± 3.2	100.2 ± 2.0	108.5 ± 4.0

Table 4.3: Yield strengths tabulated for each composition, processing, and plate thickness.

Binary Condition	Binary Yield Strength (MPa)
Mg-3Al 2.5mm	105.2 ± 2.4
Mg-5Al 2.5mm	124.8 ± 2.1
Mg-9Al 2.5mm	152.2 ± 2.6
Mg-12Al 2.5mm	173.4 ± 4.5
Mg-3Al 5mm	87.4 ± 2.6
Mg-5Al 5mm	106.3 ± 1.9
Mg-9Al 5mm	145.4 ± 2.9
Mg-12Al 5mm	161.8 ± 2.5

Table 4.4: Binary Yield strengths

m	M_{Al}	M_{Mn}	σ_0	$k_{y,Mg}$	$\Delta k_{y,Al}$	f_{skin}
4.5	19.6	120.8	4.5	0.21	2.75	0.45

Table 4.5: Constants used in the yield strength model.

Figures:

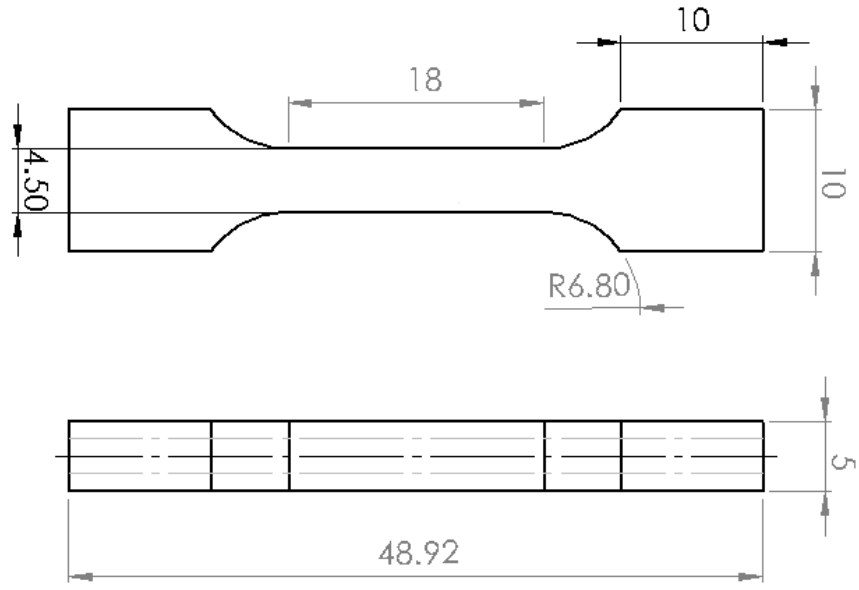

Figure 4.1: Microtensile specimen dimensions (mm) and location through the plate thickness.

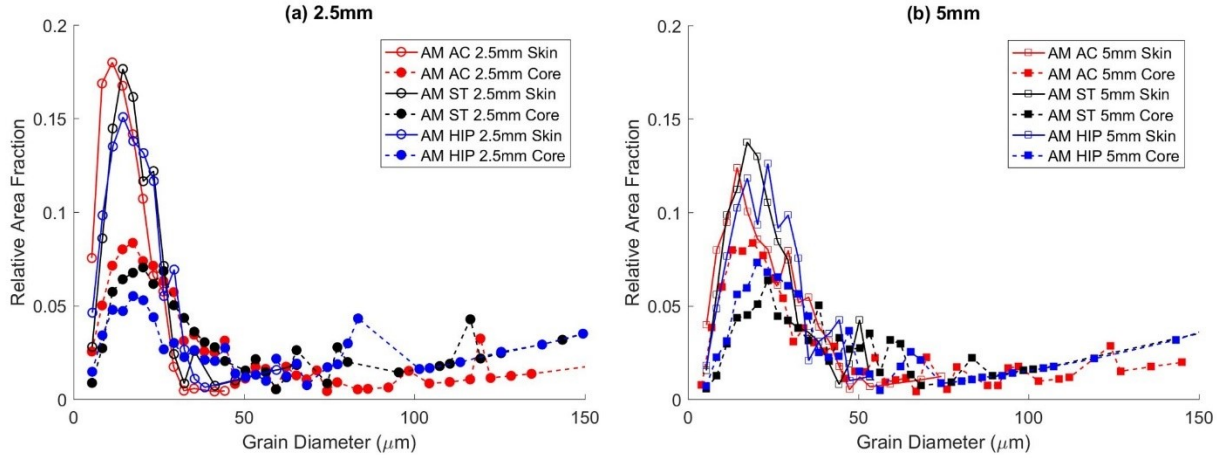

Figure 4.2: Area fraction histograms for all grains in the (a) 2.5mm and (b) 5mm plates for the as-cast, ST, HIP conditions in the AM series plates

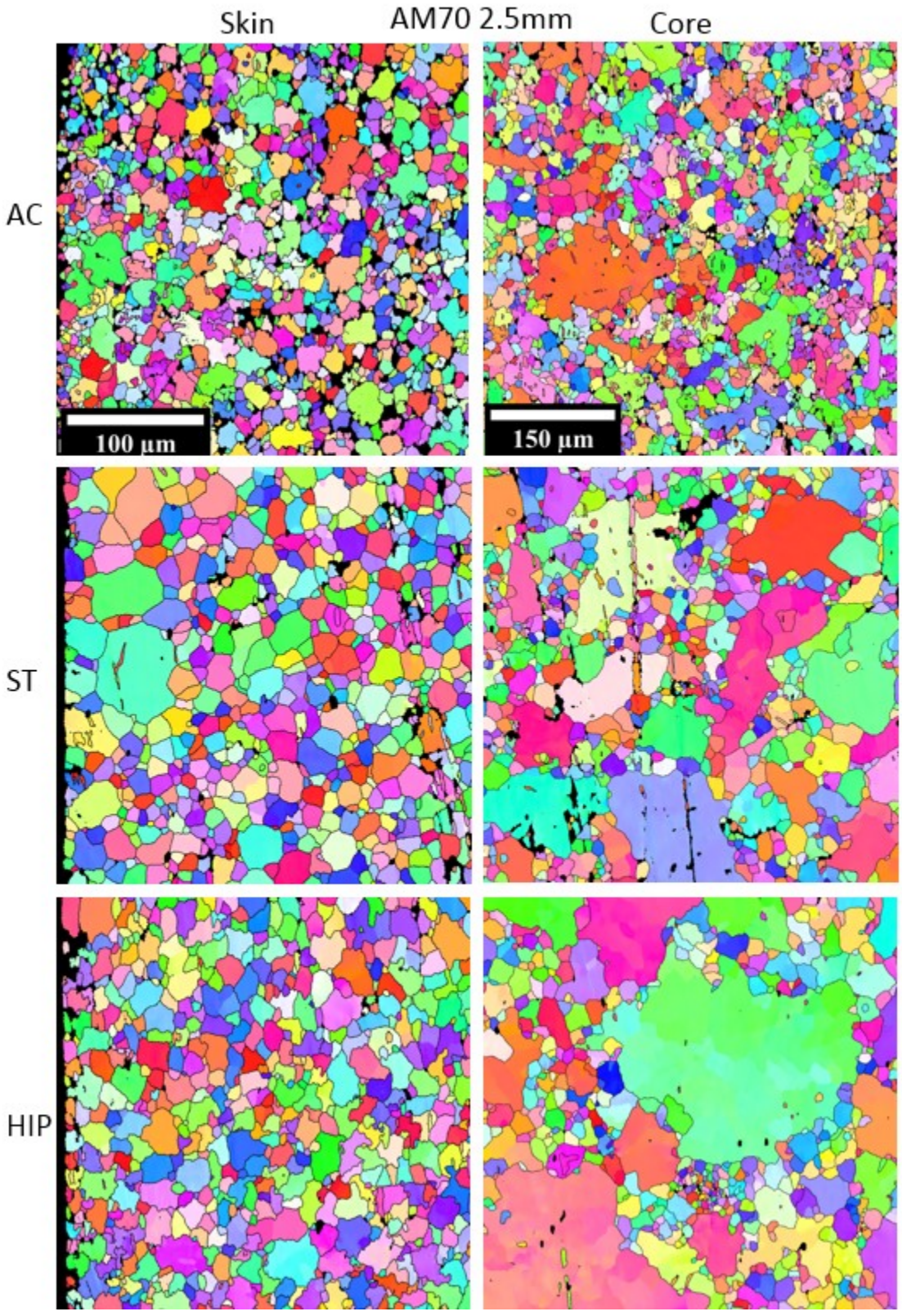

Figure 4.3: Representative EBSD maps from the skin and core of AM70 2.5mm plates for each processing condition. All skin maps have a view field of 300 µm, and all core maps have a view field of 500 µm.

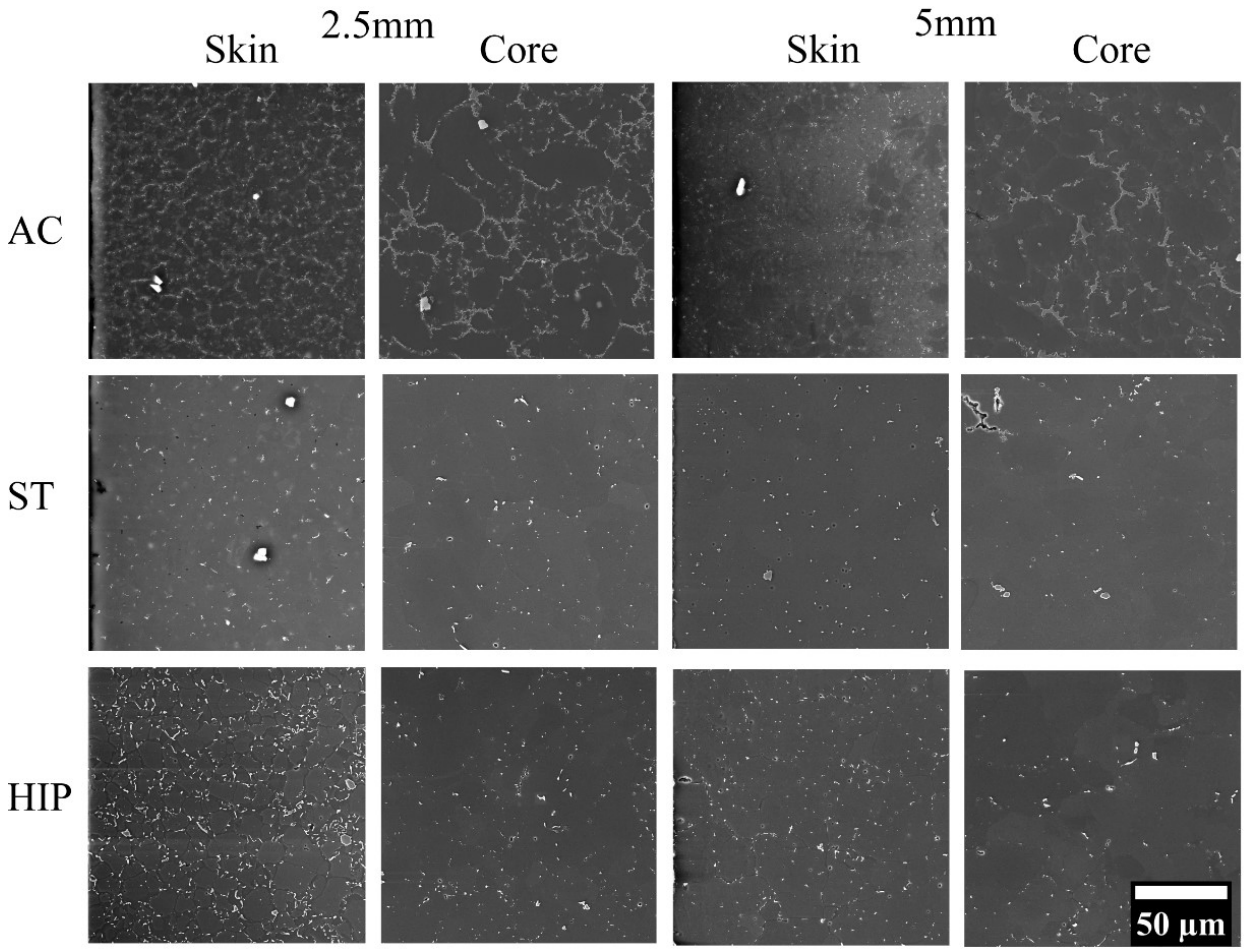

Figure 4.4: β-phase (light grey) and AlMn phases (white) as observed in the skin and core of the AM70 AC, ST, and HIP processing conditions in both plate thicknesses.

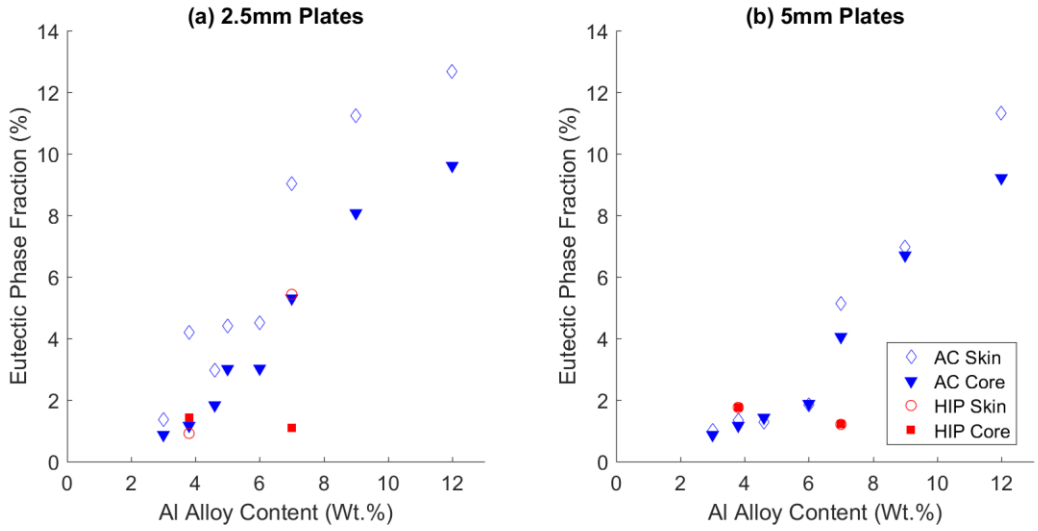

Figure 4.5: Eutectic phase fraction for skin and core in the as cast and HIP conditions in the (a) 2.5mm plates and (b) 5mm plates.

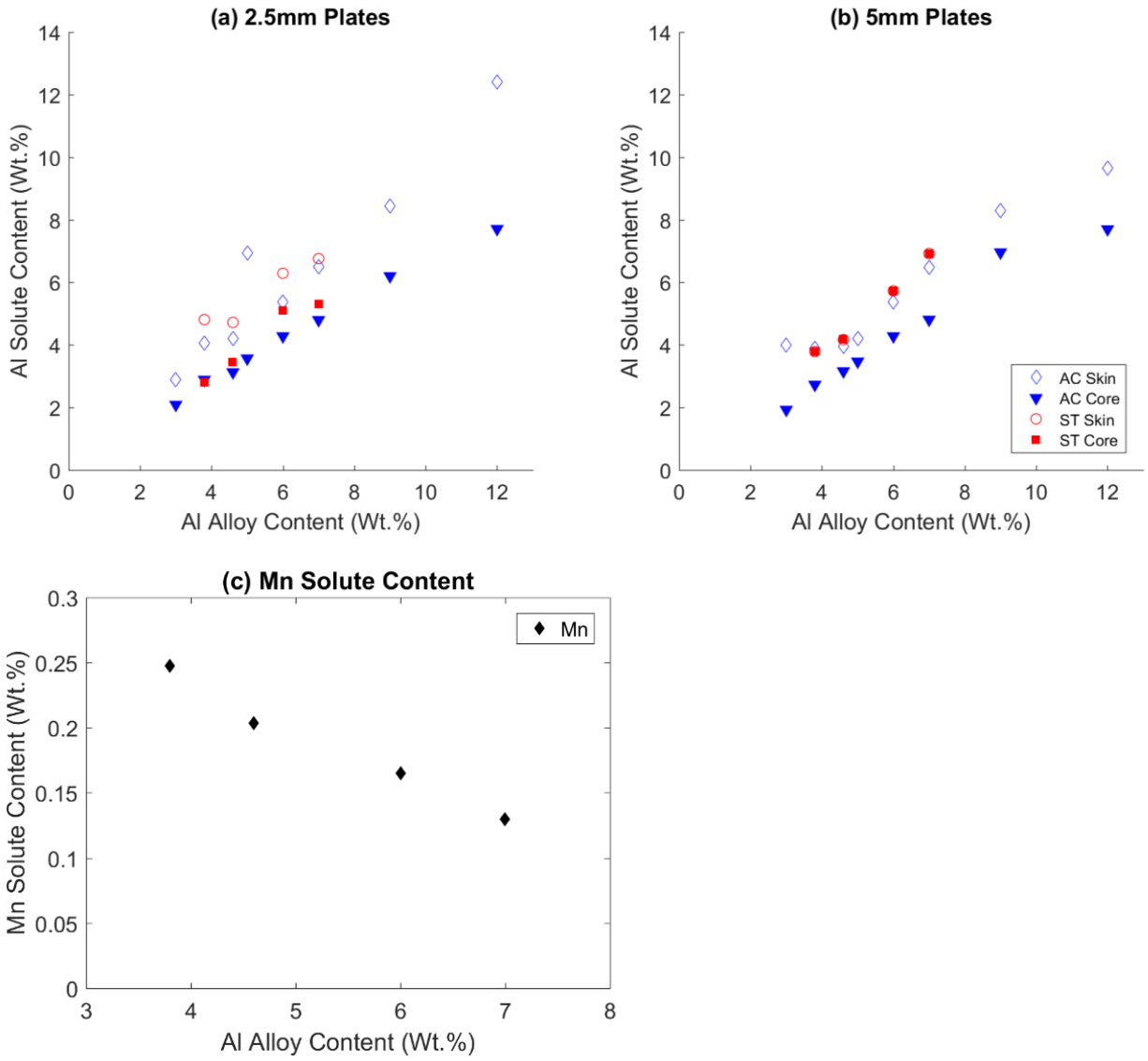

Figure 4.6: Solute fraction for the skin and core for each Al alloy content for (a) 2.5mm and (b) 5mm thick plates, and (c) the average Mn solute content for all locations.

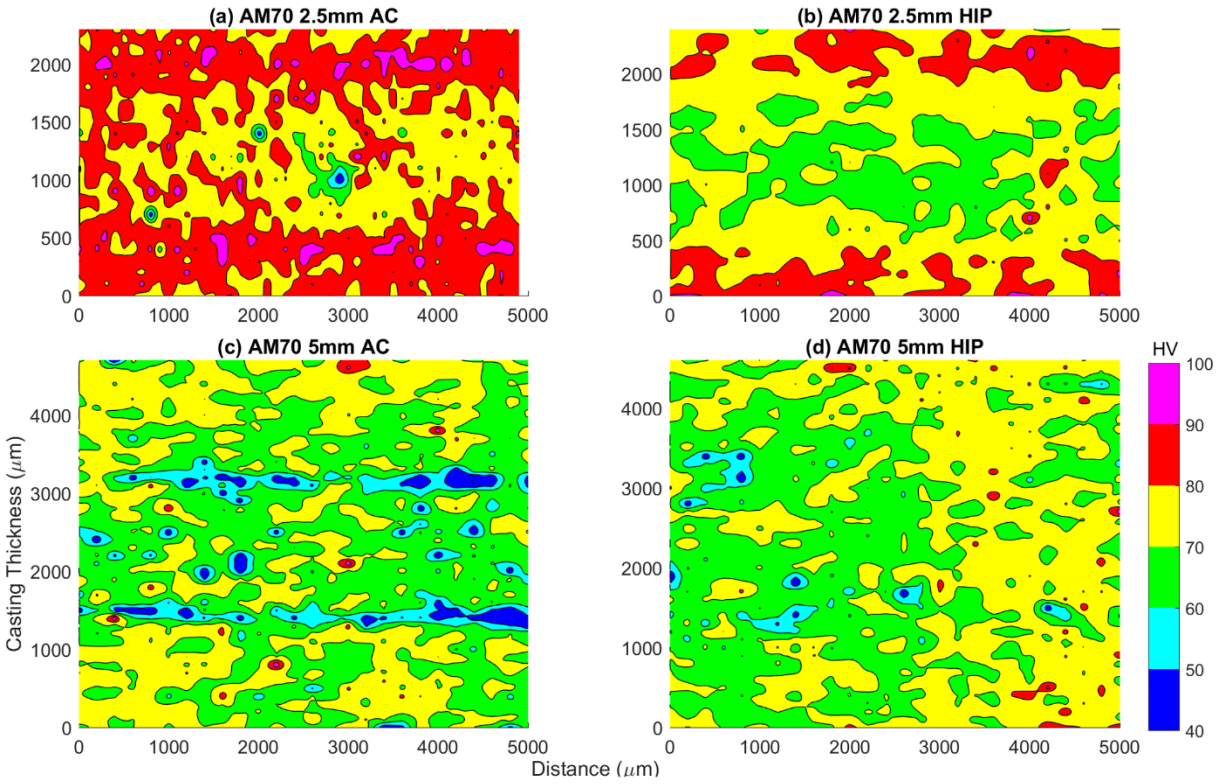

Figure 4.7: Microhardness maps for AM70 as-cast and HIP conditions for both the 2.5 and 5mm thick plates.

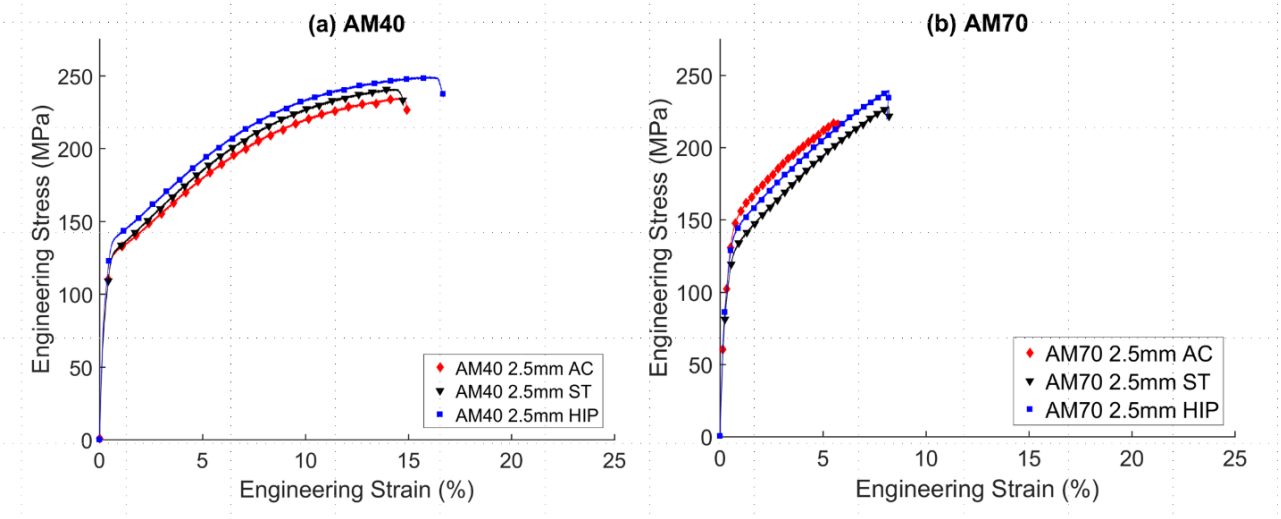

Figure 4.8: Representative tensile curves from the as-cast, ST, and HIP conditions for the 2.5mm (a) AM40 and (b) AM70 alloys.

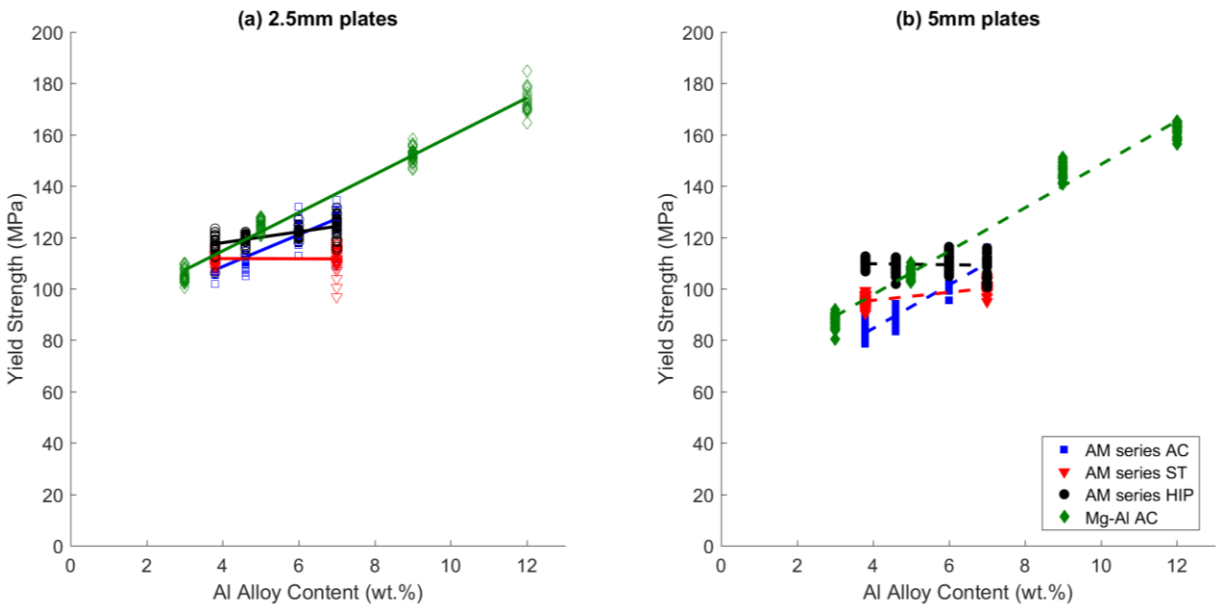

Figure 4.9: Effects of processing and Al content on the measured yield strength for (a) the 2.5mm plates, and (b) the 5mm plates.

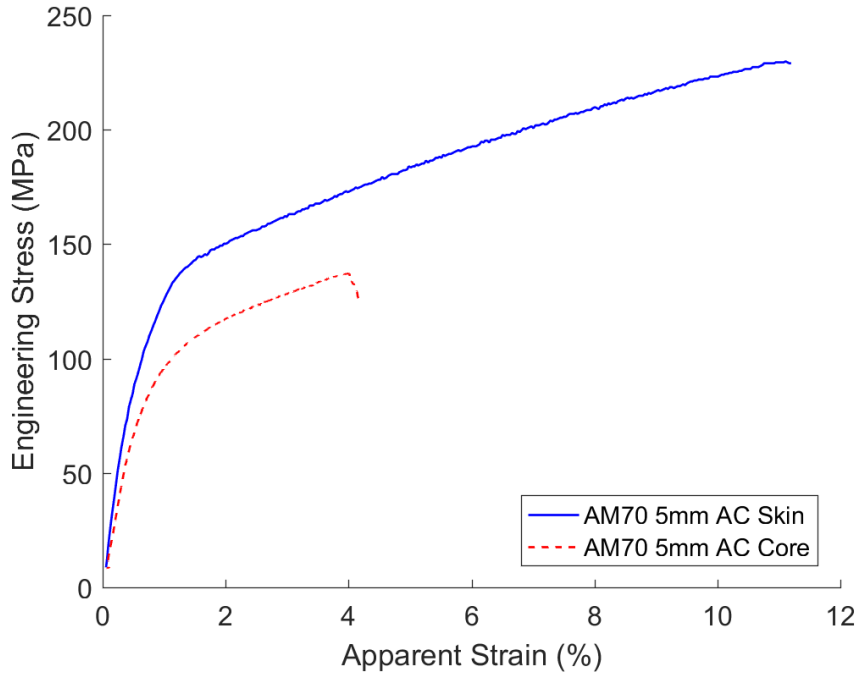

Figure 4.10: AM70 as cast micro tensile skin (solid) and core (dashed) comparison in 5mm plates for the as-cast condition.

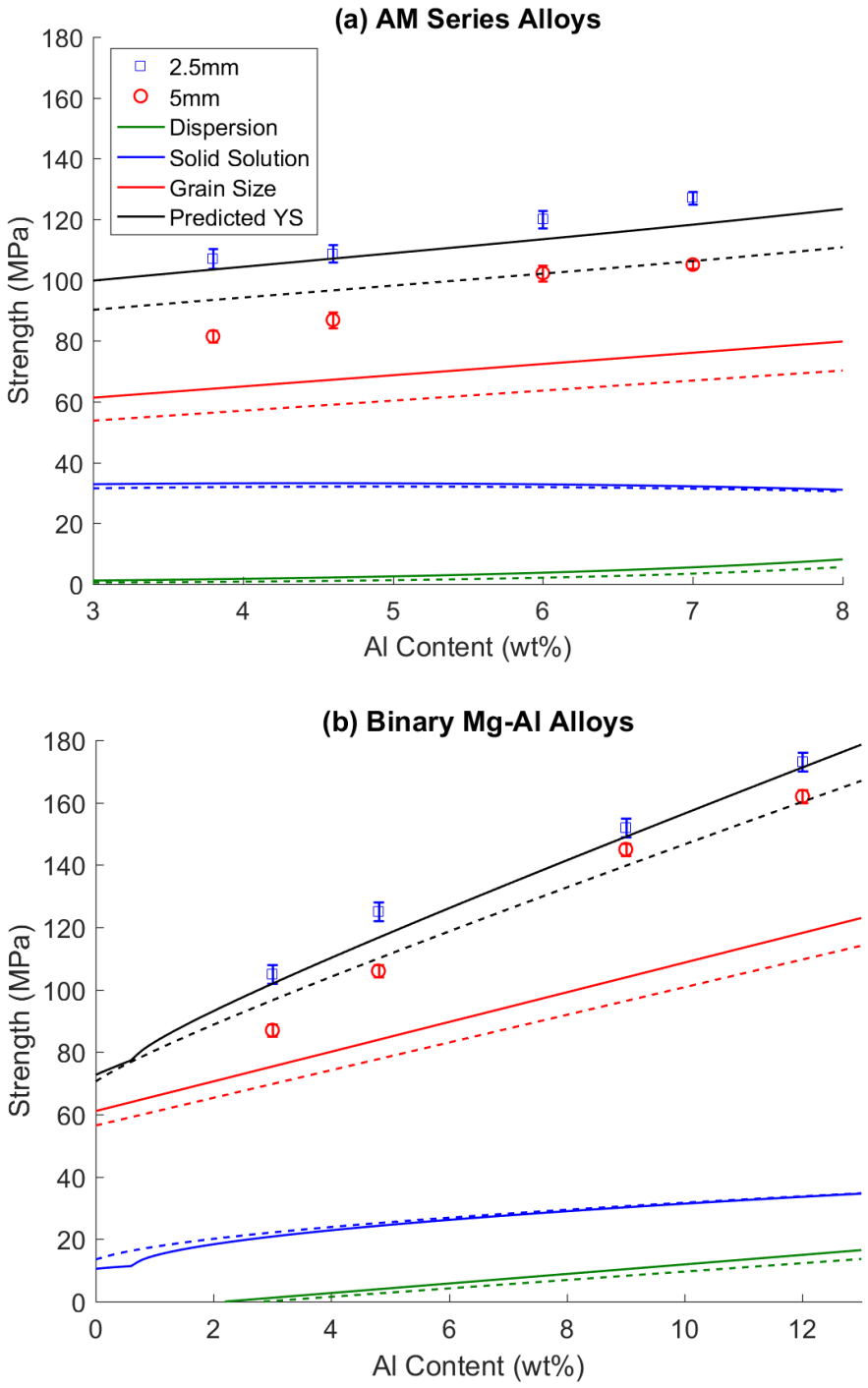

Figure 4.11: Strengthening components for the as-cast (a) AM series and (b) binary alloys for yield strength. The solid lines in each figure represent the findings for the 2.5mm plates, and the dashed lines are used for the 5mm thick plates.

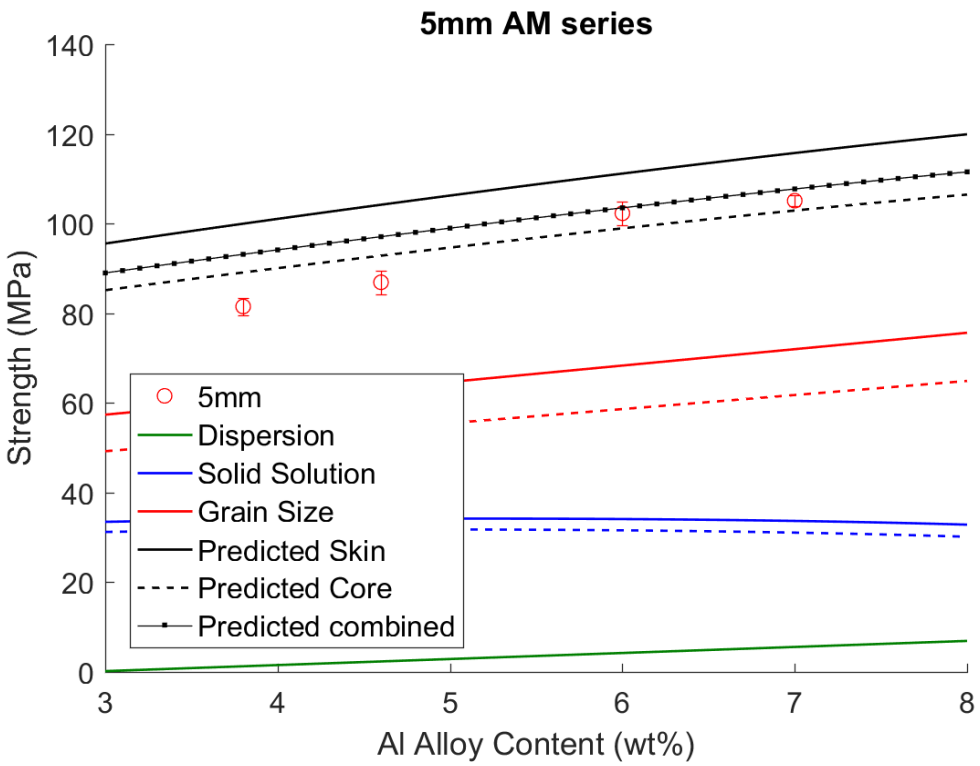

Figure 4.12: Predicted Yield strength in the skin (solid) and core (dashed) for as-cast 5mm plates. The predicted total yield strength of the skin and core is shown in the dotted line.

Chapter 5
The effect of alloying and processing on the ductility of high pressure die cast Mg alloys

Cast Mg alloys are desired for use in automotive applications; however, the ductility shows a broad distribution within a single casting, requiring overdesign or limiting their usage in production. Tensile testing is used to quantify the ductility in these alloys. In order to better understand the factors that lead to failure, high pressure die cast Mg-Al-Mn (AM series) plates were processed by either solution treatment or hot isostatic pressing (HIP) in order to identify and isolate the key intrinsic and extrinsic features in the microstructure that are related to tensile failure. Solution treatment and hot isostatic pressing were used to isolate the effects of β-phase, shrinkage porosity and oxide films. We found that there is a hierarchical effect associated with these features, which affect the total elongation. The failure distribution can be described by identifying the frequency by which each of these mechanisms causes the tensile sample to fail. Statistical analysis of the tensile behavior with the casting conditions was conducted. By understanding the frequency of failure from each type of feature, we can more completely understand the tensile ductility of these alloys and better design structural castings.

5.1 Introduction

High pressure die casting (HPDC) is used to produce parts rapidly and economically for use in automotive applications. Magnesium alloys are commonly produced by HPDC for use in

automobiles due to their high specific strength for weight reduction strategies [1,2]. HPDC is a turbulent flow process which generates a broad distribution of microstructural features through the thickness of a casting. This change in the microstructure throughout a casting has been shown to lead to variability in the tensile behavior [3]. Unpredictable, early failure is a one limitation which reduces the usage of HPDC Mg alloys in production parts. It is found that within a casting, the ductility can vary from 2% to 20% for different locations [3–5], and multiple failure mechanisms can be observed within a single casting [6]. In general, ductility is the least repeatable parameter measured in a tensile test according to ASTM standard E8. It is also one of the least understood properties of a tensile test and can be affected by alloy, microstructure and geometry [7].

In Mg alloys, as Al content is increased the ductility is observed to decrease [8–12]. The reasons for this are still not fully understood. Further study is needed to identify the dominant failure mechanisms in Mg HPDC alloys. It is generally recognized that the primary factors that limit ductility are extrinsic casting defects – including oxide films, entrapped air bubbles and shrinkage porosity [13]. Oxide films are predicted to have the largest negative impact on ductility, then shrinkage porosity, while β-phase has only a weak effect on ductility [14]. Previous work in AZ61 has shown that while the β-phase cracks during the initial loading, it doesn't tend to nucleate cracks through the microstructure [15]. Studies of these alloys have tended to focus on the effects of porosity on ductility, due to its prevalence in die cast alloys [16].

Analytical models for ductility in casting alloys have been investigated and developed for Al and Mg alloys [17–23]. These models tend to involve void nucleation and growth. Initiating factors in castings are predominantly assumed to be a function of the reduced area due to local in-homogeneities in the microstructure, such as oxide films and pores, which are predicted to act as initiation sites for small cracks [6]. It has been found by Weiler et al. that local area fraction of

porosity in AM60B was the primary factor influencing tensile failure of specimens [24]. It was observed that the fracture path tends to go through pore clusters in AM50 alloys [25,23]. This indicates that the local area fraction of defects on the surface tends to determine the failure behavior.

In order to assess the impact of shrinkage porosity, β-phase, and oxide films on the ductility, processing is used to isolate each of these microstructural features. Heat treatment is only recently applicable to die cast alloys due to refinements in the casting process such as super vacuum die casting which reduces the level of entrapped gas porosity [26], allowing castings to be heat treated. Solution heat treatment can be designed to reduce or eliminate the β-phase.

In the present study we will use solution heat treatment to isolate the effect of β-phase on the ductility distribution by comparison with as-cast plates of the same condition. In the current investigation, hot isostatic pressing (HIP) was used to reduce or eliminate the shrinkage porosity by densifying the castings. In addition, the β-phase fraction is significantly reduced during the HIP process by processing near the eutectic temperature. By isolating each of these features, the effects on ductility and strain hardening behavior can be identified. The ductility for each of these conditions can be estimated using previous developed analytical models for ductility. The change in ductility distribution is quantified and compared to the isolated microstructural features, determining the effects of each microstructural feature on the overall ductility. In this work, the model being evaluated is the Ghosh analytical model for tensile instability as described by a reduced cross sectional area function [27]. This model relates ductility to the defect fraction and the constitutive description of the strain hardening behavior of the alloy. The predicted ductility can then be found by solving for the critical strain in the inhomogenous region. The critical strain in these alloys was determined using the maximum observed ductility in the HIP plates, or the

defect free condition [20]. This model has been refined for pore size and porosity distribution [19,22], though for simplicity in this work, the base model is used to describe the overall defect fraction. In this work, by processing the as-cast material, the effects of the shrinkage porosity and β-phase can be isolated within an alloy, and trends observed across Al alloy composition. This can be used to compare to previous work on the prediction of the effect of β-phase on the hardening behavior [28].

5.2 Experimental

Magnesium plates were super vacuum die cast (SVDC) by Ford Research and Innovation Center at MagTech Corporation. Binary Mg-Al and Mg-Al-Mn (AM series Mg alloys) were die cast using the parameters described in previous work into plates of dimensions 305mm x 130mm (12”x 5”) in two thicknesses, 2.5mm and 5mm [29]. The composition of each condition is measured by Optical Emission Spectroscopy (OES), and given in Table 5.1.

In order to isolate the different microstructural features which may contribute to variation in the ductility, solution heat treatment (ST) and hot isostatic pressing (HIP) were used. In order to remove the β-phase, ST was conducted in a Carbolite open-air box furnace for 2.25 hours at 413°C. Solution treated samples were water quenched. HIP was completed at Bodycote in Princeton, KY in a 17” diameter chamber to remove both be β-phase and shrinkage porosity. Plates were processed for 2.25 hours at 410°C and 100 MPa. Plates were laid flat for processing in order to prevent creep and distortion during heating and cooling processes, and argon cover gas was used to achieve pressure at temperature without oxidation. Plates were furnace cooled at a rate of approximately 0.1°C/s.

Following plate processing, samples were machined from the plates parallel to the casting flow direction. Tensile specimens were machined according to ASTM standards E8/B557 with a gauge length of 25.4mm and a width of 6.4mm. The specimen thickness was equal to the plate thickness, 2.5 or 5mm and the as-cast surface was retained. Tensile testing was conducted on a hydraulic MTS load frame with a 25mm extensometer to measure the strain. Tensile tests were performed at room temperature at an initial strain rate of 1×10^{-3} s^{-1}, and a constant displacement rate of 2 mm/min until sample failure. At least 30 samples per condition were tested to get sufficient samples for statistical analysis.

Metallographic specimens were prepared from the grip section of the tensile specimens. Specimens were polished to a 1 μm finish, and etched for 3-5 seconds using a 5°C acetic nitric etchant. Electron backscatter diffraction and secondary electron imaging were used to quantify grain size, β-phase, porosity area fraction. Full details on microstructure quantification can be found in Chapters 3 and 4. Fractography was completed on select samples using secondary electron imaging. This was done to quantify the features on the fracture surface, and the overall area fraction of those features. Results from scanning electron microscopy were generated using a Tescan Mira FEG SEM. All experimental results from this work are archived on Materials Commons.

5.3 Results

5.3.1 Microstructure quantification

HPDC AM series alloys have intrinsic and extrinsic features associated with alloying and the die casting process, respectively. The intrinsic features such as the grain size, eutectic phase fraction, and solute content are quantified in the AC condition (Chapter 3), and for each of the processing conditions (Chapter 4). The processing conditions are referred to as the as-cast, solution treated (ST) and hot isostatically pressed (HIP) conditions. After ST, the β-phase is fully dissolved

but all other features remain constant. Similarly, after HIP, the shrinkage porosity is fused, and β-phase partially dissolved, while leaving oxide films and other casting defects as is. Each of the above microstructural features are quantified in depth in previous work.

The grain structure in these alloys consists of fine α-Mg grains and large, externally solidified crystals (ESCs). It is found that there is no change in the α-Mg grain size with aluminum content. The grain size tends to increase with plate thickness, and there is an increased fraction of ESCs in the 5mm plates. There is also a skin and core structure that forms in these castings. The skin has a fine grained structure with minimal ESCs, and a higher hardness than the core. This die cast skin has a constant thickness for all Al contents and processing conditions in the AM series alloys, though it is thicker in the 5mm plates. The skin thickness is 600 μm for the 2.5mm plates, and 1100 μm in the 5mm plates. This results in an equivalent skin fraction of 0.45 observed for both the 2.5mm and 5mm thick plates [29]. There is a slight increase in average grain size and ESC fraction in the ST and HIP conditions, and it is constant between both.

The primary eutectic phases in AM series alloys are the β-$Mg_{17}Al_{12}$ phase (referred to as the β-phase hereafter) and AlMn intermetallic phases. The area fraction of β-phase increases with aluminum content. This follows a linear trend for both the binary and ternary alloys. There is a decrease in the β-phase fraction and solute content with increased plate thickness. Again, there is no change in trend from the binary and ternary alloys. After ST, the β-phase is fully dissolved, and after HIP there is some precipitation of β-phase during the cooling process. The β-phase that forms during cooling is primarily found along the grain boundaries in the skin region.

Porosity and Oxide films

The area fraction of porosity was quantified using BSE imaging for the AM series alloys in both sample thicknesses. At least 5 images from each sample are used, comprising the full

thickness of the plates. Based on previous results [29], there is observed to be no variation of porosity with aluminum content in these plates. The average porosity in the 2.5mm as-cast plates is 0.7%, and 0.79% in the 5mm plates After ST, there is no change in the overall area fraction of porosity, with averages of 1.0% and 0.89% in the 2.5mm and 5mm thick plates respectively. There are higher porosity levels observed in the binary alloys as compared to the as-cast AM series alloys, with averages of 3.33 and 1.32% in the 2.5mm and 5mm plates respectively.

The amount of porosity is significantly reduced after HIP. The average area fraction of porosity observed after HIP in the 2.5mm plates is 0.46, with a range from 0 – 1.8%. The upper bound observed was a region of a high quantity of gas porosity There is a similar area fraction of porosity remaining in the 5mm plates, with an average of 0.39%, and a range of 0 - 0.6%. These values are included in Table 5.2.

Examples of oxide film morphologies are found in Figure 5.1. Oxides films tend to be large, planar defects, and are found throughout the full thickness of the castings. There is no change in the shape or distribution of the oxide films observed with processing. The area fraction of oxide films showed no discernable trend between different conditions or plates. The distribution of oxide films appears independent of alloying or casting parameters. Qualitatively, there were fewer oxides observed in the binary Mg-Al castings, indicating that improvements were made in the melt and casting practices for the binary alloys compared to the AM alloys. Alternatively, the formation of oxide films could be related to the composition of the AM series alloys, however further study is needed to better understand the formation of oxide films in Mg alloys.

5.3.2 Tensile results

The tensile behavior has been characterized for each condition. Representative stress-strain curves are shown in Figure 5.2 for the binary conditions. Representative curves for the as-cast

ternary AM-series alloys are shown in Figure 3.10, and are generally consistent with Figure 5.2 [29]. With increasing aluminum content in the as-cast condition, for both binary and ternary alloys, an increase in the yield strength, and a decrease in the ductility and strain hardening exponent (n) are observed. The yield strength is discussed in detail in previous work (Chapter 4). The ductility and strain hardening exponents are summarized in Table 5.3 and Table 5.4. The strain hardening exponent, n, is found using the Hollomon formulation, in Equation 5.1 [30]. It is found for both the AM series and binary alloys that with increasing Al content, n decreases, and this is similar for both the 2.5mm and 5mm thick plates.

[5.1] $\sigma = K\varepsilon^n$

Ductilities for the AM and binary alloys are shown in Figure 5.3 and Figure 5.4, respectively. The effects of solution treatment and HIP can be observed in the tensile properties. After solution treatment, there is generally an increase in the observed ductility for a given alloy content in the AM series. After HIP, there is a further increase in the average, but also an increase in the variability. The standard deviation in each condition is higher for all Al contents than both the as-cast and the ST. In addition, in Figure 5.3, there are two general trends observed in the ductility as a function of aluminum content. One trend is that the upper bound of ductility is observed to decrease with Al content. Second is that there is a nominally constant lower bound is observed, of approximately 2-5% elongation across Al contents. This lower bound is approximately constant for all processing conditions. In addition, there is a higher average ductility in the binary plates than in the AM series plates in the as-cast condition. This is shown in Figure 5.4, which compares the ductility distribution in the binary plates to the trend lines for each of the AM series conditions.

In general, the strain hardening exponent tends to decrease with increasing aluminum content, shown in Figure 5.5. There are similar strain hardening exponents observed in both the binary and ternary alloys, and for both plate thicknesses. This change in strain hardening exponent is also observed in the binary Mg-Al plates, with very similar values, shown in Figure 5.6. In short, there is no effect of the Mn solute content on the observed strain hardening exponent. After processing, there is a small change in the strain hardening exponent for the ST and HIP conditions. For the 2.5mm condition, n remains nominally constant with aluminum content for the ST condition when compared to the decrease observed in the as-cast condition. n in the AM70 conditions tends to be slightly lower and have a broad distribution due to the low ductility measurements that can be observed.

The fracture strength in these alloys has a very broad distribution of measured values, Figure 5.7. The distribution of fracture strengths is comparable to the ductility distributions, as necking is typically not observed in these alloys. For all Al contents in the as-cast condition, the average fracture strength remains nominally constant. This is true of the binary Mg-Al alloys as well, Figure 5.8. After ST, the upper bound of the fracture strength increases, and then further increases after HIP processing. The lower bound is similar for all Al contents, and is tied to samples with particularly low ductility. These trends are the same for both the 2.5mm and 5mm thick plates. The fracture strength is slightly lower in the 5mm plates however, and is again likely tied to the apparent ductility of the samples.

5.3.3 Characterizing the ductility distribution

In order to quantify the effects of types of defects on the ductility distribution, the fracture surface features of all tensile samples were qualitatively characterized. The surface features were examined visually and assigned one of three classifications: defect free, small defects, and large

defects. Example fractographs of each of these classifications are provided in Figure 5.9 and Figure 5.10. These figures show images of the full fracture surfaces, and high magnification fractographs of typical fracture surface features.

Defect-free samples were those that showed characteristics of ductile failure, and were visibly defect free or showed only isolated defects. Ductile failure is characterized by cup and cone features on the surface, and ended in shear fracture. The fracture surface was sheared at approximately a 45° angle to the loading direction. This sheared surface was only observed in the 2.5mm plates. The 5mm plate exhibited dimpled fracture surface features but the fracture surface was nominally flat and perpendicular to the loading axes. Samples characterized as having "small defects" had observable pores or oxides on the fracture surface that were nominally between 10 and 25% of the surface area for all apparent defects (e.g. approximately 1 to 4 mm^2). The "large" defect samples tended to have large inclusions, typically oxide films, which were greater than 25% of the plate thickness. These were defects greater than approximately 1000 μm in length in at least one direction, and frequently much larger, up to 3mm in size. There was a significant reduction in the effective cross sectional area of these samples.

The total elongation at fracture is used as a measure of the ductility of each condition. The distribution in measured total elongation at fracture of the AM series alloys was characterized using a cumulative probability function using a 3-parameter Weibull fit, shown in Equation 5.2. Figure 5.11, shows these distribution functions for each alloy, with separate cumulative probability distributions for the as-cast, solution treated and HIP conditions. These cumulative probability distributions were developed using techniques proposed by Tiryakioglu and Campbell [31] who used this type analysis for characterizing the ductility, tensile strength, and fatigue life of die cast Al alloy A356. The probability distribution fit to this data is a single 3-parameter Weibull fit. The

Weibull parameters, σ_T, σ_0, and m determined for these distributions are provided in Table 5.5. σ_T represents the threshold value, or the value below which no specimen should fail. σ_0 is the scale parameter, and m is the shape parameter of the Weibull distribution. Also included in Figure 5.11 are the observed defect type for each sample which are correlated with specific values of ductility. Samples in which" large defects" were observed on the fracture surface tended to show lower ductilities, although there were exceptions to this. The ST and as-cast samples had similar defect frequencies. The HIP condition exhibited a higher frequency of ductile features (e.g. shear failures in the 2.5mm thick samples), and a higher upper bound for the ductility.

$$[5.2]\ P = 1 - \exp\left(-\left(\frac{\sigma-\sigma_T}{\sigma_0}\right)^m\right)$$

5.4 Discussion

5.4.1 Tensile behavior

The processing condition (e.g. as-cast, solution treated and HIP) had a significant influence on the observed tensile behavior. In general, as Al content increased the yield strength increases, and the strain hardening exponent and ductility decreased. The reduction in ductility with increasing Al content in the as-cast condition is typical of results from other studies of both AM and AZ series [8–10,12,32]. This decrease in ductility is observed in both the upper bound of observed ductility shown in Figure 5.3, and also in the tabulated average in Table 5.3.

After processing, the ductility tends to increase, for both the ST and HIP conditions. The average ductility increased after processing in both conditions, though to a greater degree in the HIP condition. The upper bound of ductility is greater in the HIP condition than the ST condition. The increase in ductility in the ST condition can be attributed to the elimination of the β-phase, as there are no other changes in the microstructure. This influence of β-phase on the ductility is likely

only a very minor effect, where it only affects the upper end of observed ductilities. It has been observed that while the β-phase tends to crack early in the loading process, these cracks did not tend to extend across the fracture surface. This was shown in thixomolded AZ61 and HPDC AM50 [15,33], where the β-phase is observed to crack, but the cracks do not coalesce.

The increase in ductility in the HIP conditions is likely due to the reduction in shrinkage porosity. It has been commonly observed that the ductility is significantly higher in samples in which the pore volume fraction is lower [24,34]. This was also observed by Li et al., who found that in in-situ tensile tests of HPDC AZ91 cracks would propagate along the regions with shrinkage porosity or β-phase [16]. In samples in which pores were reduced, the voids propagated along a transgranular path, shown in in-situ tensile analysis of die cast AM60 [35]. The lower bound on the ductility is the same for all three processing conditions in the AM series. We attribute this to the random distribution of large oxide bifilms and other casting defects in these materials. These large oxides were not removed by the HIP process. These sites are typically considered to be sites for failure nucleation [36]. Since they were not eliminated in the HIP condition, a constant lower bound in ductility was observed for all conditions and thus paradoxically, while the average ductility is higher for the HIP condition, the range of values observed is also significantly higher.

The binary Mg-Al castings tended to have higher ductilities compared to the as-cast AM series alloys, although the range of values was similar between these two different alloys systems. The higher ductilities observed in the binary alloy samples are likely due to improvements in the casting process. The upper bound in ductility for the binary plates tended to fall along a linear upper bound with the AM series HIP conditions. It can be noted for the Mg-Al plates, that the Mg-12Al samples were so brittle that some of them failed at defects in the machined surface in the grip section or at the radius transitioning to the gauge section. Samples where failure was in the grip

section that were not included in the populations for statistical analysis. These failed at nominal strains of 0.1 to 1%, and failing in the grip section was not observed for any other alloy or processing condition.

The strain hardening exponent, n, was observed to decrease as Al content increased, for both the binary and ternary systems. The strain hardening behavior describes how much a material can deform during an applied stress. If more deformation can be expected before failure, the material would be expected to possess a higher theoretical ductility. This change in strain hardening exponent with Al is consistent with previous measurements in cast AZ alloys, where the strain hardening exponent was reported to decrease as Al increased [32]. It is observed in the as-cast condition that there is a threshold between 5 and 6 wt.% Al where the initial strain hardening behavior changes. Below 6 wt.% Al, there is an initial plateau in the strain hardening behavior observed. This is consistent with previous work by Yang et al., where this plateau was observed in binary Mg-Al alloys up to 5.51 wt.% Al [12]. Yang et al. predicts this to be due to the activation of prismatic and twinning slip systems, while the initial hardening behavior is a result of basal slip. This initial plateau was also observed in both the ST and HIP conditions, indicating that effect of β-phase or shrinkage porosity on the initial yielding behavior, beyond that explored on yield strength in further work (Chapter 4).

5.4.2 Assessing the ductility variability

One method of characterizing the local mechanical properties is the determination of local tensile instability based on reduced cross sectional areas due to imperfections in the material. An analytical approach developed by Ghosh [27] is used to quantify the effects of imperfections in strain hardening alloys. The reduction in ductility is predicted to be a function of the reduced cross sectional area as a result of defects in the material. The Ghosh model is modified in Equation 5.3

by using a simplified constitutive model, Equation 5.1, as developed by Caceres and Selling. This approach by Caceres was refined and shown to be effective in AlSiMg alloys [20], and AZ91 and AM60 [23,37]. The Ghosh model is described as characterizing the effect of strain localization caused by a reduced cross sectional area in an inhomogeneous section of a tensile specimen.

[5.3] $(1-f)\varepsilon_i^n\, e^{-\varepsilon_i} = \varepsilon_h^n e^{-\varepsilon_h}$

The elongation to failure is limited by the strain localization as a result of a reduced cross sectional area. Equation 5.3 shows how the homogenous strain, ε_h^n, which is taken to be the macroscopic plastic elongation to failure, can be defined as a function of an inhomogenous strain, ε_i, the strain hardening exponent, n, and the defect fraction, f. In our investigation, we have taken the strain hardening exponent to be the average value for each condition. The defect fraction is the expected defect fraction at the point of failure, which is taken to be the defect fraction on the fracture surface. Equation 5.3 describes the true plastic strain at failure, based on the use of the constitutive model in Equation 5.1. In this case the true strain was determined by using the relationship, $\varepsilon_T = \ln(1+\varepsilon_e)$. This is taken to be valid as necking is typically not observed in these alloys. The critical intrinsic ductility, ε_i^*, is taken to be equivalent to the maximum ductility observed, or the maximum that can be observed from a casting in the defect free, or HIP condition. in the current investigation, this intrinsic ductility used in this model was set to be a linear fit of the upper bound of the measured ductility against alloy Al content in the binary alloys and the HIP AM series alloys, similar to the trend line in Figure 5.4 for the binary Mg-Al alloys. This fit ranges from 28% engineering strain in the Mg-3Al, to 5% in the Mg-12Al for the 2.5mm plates, and 24% to 4% for the 5mm plates respectively.

By approximating the intrinsic ductility from the upper bound of the measured ductility, a nominal defect fraction for each tested as-cast sample can be calculated. The defect fraction is

found by solving Equation 5.3 with the average strain hardening exponent for each condition and the intrinsic true strain observed from tensile testing, which is found in Figure 5.5. There is an apparent strain localization due to the defects on the fracture surface. In order to determine the apparent homogenous strain, the This is done by determining the point at which the strain in the defect region, ε_i, reaches the critical strain, and finding the x-intercept, ε_h, at that point, as shown in Figure 5.12. This is done for a range of defect fractions, and the results described with a polynomial fit. By fitting the reduced apparent homogeneous strain with the defect fraction, the range of effective ductilities can be found.

The defect fractions for the measured ductility distributions can then be calculated using the fitted polynomial. Results of the calculated defect fractions can be found in Figure 5.13a) for the 2.5mm plates and b) for the 5mm plates of the AM series. The typical range of defect fractions predicted for the as-cast AM series alloys is from 5% to 25% in the 2.5mm plates, shown in Figure 5.13(a). The defect fraction is similar for the AM40, AM50 and AM60, but significantly higher in the AM70. This is consistent with nominal measurement of the bulk porosity [29]. The AM70 has shown that the typical casting quality of these plates tended to be worse than the other three AM series alloys. This was independent of the plate thickness, as the 5mm AM series plates showed similar trends. The overall defect fraction was predicted to be higher in the 5mm plates though, with a range of 8% up to 35+%.

This range of defects can be described as the apparent casting quality, or the typical quality observed in the alloys. In general, the range of calculated defect fractions is much higher than the typical pore volume fractions observed in these alloys, even when looking at local strain distributions. Typical area fractions of porosities in these alloys is less than 2% for the AM series, and the Ghosh model predicts up to 30%. The local defect fraction on the casting surface tends to

be higher, and will be a more accurate measure of the defect fraction that caused failure. The defect fractions predicted by the Ghosh model roughly correlate with the qualitative measurements of the fracture surface. However, while samples with large defects frequently have low ductility, there are some notable exceptions observed in Figure 5.11. Thus the defects on the fracture surface are likely not the full reason for low ductility, and further study is required.

In the simplified model, there is no correction for the distribution or distance to the surface of defects, which likely has a strain concentration effect [22]. The localization effect of defects near the surface could decrease the apparent ductility. This results in an over prediction of the defect fraction from the current model. By improving how defect size and distribution is captured, the range of ductility from a defect fraction will be more accurate. This refinement could be applied in the future to potentially get a more accurate defect range. Additionally, there is likely a threshold at which the impact of a large pore may be more concentrated than that predicted by the Ghosh model. One way to correct this would be to apply a large defect, fracture mechanics model to account for these failures. In order to further both of these hypotheses, more detailed analysis of the defect fraction on the fracture surface needs to be completed. While the current model likely over predicts the local defect fraction, It still allows us to find a range of apparent ductilities for a given hardening behavior and range of defects for use in modeling efforts with an upper and lower bound of apparent ductility.

5.5 Conclusions

In this study, the effects of alloying, plate thickness, and processing on the ductility have been assessed. It is found that with increasing Al content, the ductility and strain hardening exponent decrease. Solution treatment and HIP improve ductility. This is true of all Al contents and plate thicknesses. Regardless of heat treatment, the lower bound of ductility remains the same.

This lower bound of ductility observed is attributed to the deleterious effects of oxide bifilms, due to the effective reduction in cross sectional area. Bifilms can be considered a pre-existing crack in the material, which tends to significantly reduce the observed ductility. By varying the microstructure using ST and HIP, the hierarchy of defects can be validated, in that oxide bifilms have the strongest negative effect on ductility, followed by shrinkage porosity, and β-phase fraction.

The effects of the local defect fraction on the ductility can be estimated using the Ghosh model coupled with an intrinsic ductility and a calibrated "effective defect fraction". It is found that the reduction in ductility increases with increasing effective local defect fraction, which is predicted to be between 5 and 30% of the local area. This decrease in ductility with defect fraction is predicted to be related to the strain localization due to the reduction in cross sectional area. The fracture surfaces were qualitatively characterized for defect fraction, and while large defects generally led to lower observed ductilities, there were some notable exceptions. Further work is needed to understand the distribution associated with ductility, and the role of different defects in the failure behavior.

Acknowledgements

The authors are grateful to Xin Sun, Mei Li, and Joy Forsmark for many helpful discussions. Thanks to Larry Godlewski and Jacob Zindel at Ford Motor Company for providing the SVDC cast plates. Thanks to Mason Bennett for assistance in metallographic preparation and analysis. The authors gratefully acknowledge funding for this project from the Department of Energy Office of Vehicle Technologies under the Automotive Lightweighting Materials Program managed by Dr. Will Joost, via subcontract with Pacific Northwest National Laboratory. The use of the Materials Commons to archive the data presented in this paper is appreciated. Funding for

Materials Commons is from the U.S. Department of Energy, Office of Basic Energy Sciences, Division of Materials Sciences and Engineering under Award #DE-SC0008637 as part of the Center for PRedictive Integrated Structural Materials Science (PRISMS Center) at University of Michigan.

References

[1] B.L. Mordike and T. Ebert: *Mater. Sci. Eng. A*, 2001, vol. 302, pp. 37–45.
[2] W.J. Joost and P.E. Krajewski: *Scr. Mater.*, 2016, vol. 128, pp. 107–12.
[3] J.H. Forsmark, J.W. Zindel, L. Godlewski, J. Zheng, J.E. Allison, and M. Li: *Integr. Mater. Manuf. Innov.*, 2015, vol. 4.
[4] J.H. Forsmark, Z. Dowling, K. Gibson, C. Mueller, L. Godlewski, J.W. Zindel, and J.M. Boileau: *SAE Int. J. Mater. Manuf.*, 2015, vol. 8.
[5] X. Chen, D.A. Wagner, D.Q. Houston, and R.P. Cooper: in *Proc. Fo IMECE04*, 2004, pp. 1–8.
[6] J. Campbell: *Castings*, 3rd ed., Butterworth-Heineman, Oxford, 1991.
[7] *Ductility: Papers Presented at a Seminar of the American Society for Metals, October 14 and 15, 1967.*, American Society for Metals, Metals Park, OH, 1968.
[8] T.K. Aune, H. Westengen, and T. Ruden: *SAE Tech.*, 1993, pp. 51–57.
[9] P. Bakke, K. Pettersen, and H. Westengen: *JOM*, 2003, pp. 46–51.
[10] T. Abbott, M.A. Easton, and W. Song: *Mater. Sci. Forum*, 2003, vol. 419–422, pp. 141–46.
[11] T.K. Aune, H. Westengen, and T. Ruden: *SAE Tech.*, 1994, pp. 65–69.
[12] K. Vanna Yang, C.H. Cáceres, A.V. Nagasekhar, and M.A. Easton: *Mater. Sci. Eng. A*, 2012, vol. 542, pp. 49–55.
[13] D. Rodrigo, M. T. Murray, and H. Mao: *SAE Int. Congr. Magnes. Sess.*, 1999.
[14] M.A. Easton, T. Abbott, and C.H. Cáceres: *Mater. Sci. Forum*, 2003, vol. 419–422, pp. 147–52.
[15] T.D. Berman, T.M. Pollock, and J.W. Jones: *Metall. Mater. Trans. A*, 2015, vol. 46, pp. 2986–98.
[16] X. Li, S.M. Xiong, and Z. Guo: *Mater. Sci. Eng. A*, 2016, vol. 672, pp. 216–25.
[17] G. Chadha, J.E. Allison, and J.W. Jones: *Metall. Mater. Trans. A*, 2007, vol. 38, pp. 286–97.
[18] C.D. Lee and K.S. Shin: *Mater. Sci. Eng. A*, 2014, vol. 599, pp. 223–32.
[19] C.D. Lee, T.I. So, and K.S. Shin: *Mater. Sci. Eng. A*, 2014, vol. 599, pp. 28–37.
[20] C.H. Cáceres and B.I. Selling: *Mater. Sci. Eng. A*, 1996, vol. 220, pp. 109–16.
[21] J.P. Weiler and J.T. Wood: *Mater. Sci. Eng. A*, 2009, vol. 527, pp. 25–31.
[22] J.P. Weiler and J.T. Wood: *J. Alloys Compd.*, 2012, vol. 537, pp. 133–40.
[23] S.G. Lee, G.R. Patel, A.M. Gokhale, A. Sreeranganathan, and M.F. Horstemeyer: *Scr. Mater.*, 2005, vol. 53, pp. 851–56.
[24] J.P. Weiler, J.T. Wood, R.J. Klassen, E. Maire, R. Berkmortel, and G. Wang: *Mater. Sci. Eng. A*, 2005, vol. 395, pp. 315–22.
[25] J. Song, S. Xiong, M. Li, and J.E. Allison: *J. Alloys Compd.*, 2009, vol. 477, pp. 863–69.
[26] A. Luo and M.O. Pekguleryuz: *J. Mater. Sci.*, 1994, vol. 29, pp. 5259–71.
[27] A.K. Ghosh: *Acta Metall.*, 1977, vol. 25, pp. 1413–24.
[28] E.I. Barker, K.S. Choi, X. Sun, E. Deda, J. Allison, M. Li, J. Forsmark, J. Zindel, and L. Godlewski: *Comput. Mater. Sci.*, 2014, vol. 92, pp. 353–61.
[29] E. Deda, T.D. Berman, and J.E. Allison: *Metall. Mater. Trans. A*, Accepted Manuscript, 2017.
[30] J. H. Hollomon: *Trans. Am. Inst. Mining, Metall. Pet. Eng.*, 1945, vol. 162, pp. 268–89.
[31] Murat Tiryakioğlu and John Campbell: *Metall. Mater. Trans. A*, 2010, vol. 41, pp. 3121–29.

[32] N. Tahreen, D.L. Chen, M. Nouri, and D.Y. Li: *Mater. Sci. Eng. A*, 2014, vol. 594, pp. 235–45.
[33] J. Song, S. Xiong, M. Li, and J.E. Allison: *Mater. Sci. Eng. A*, 2009, vol. 520, pp. 197–201.
[34] A.M. Gokhale and G.R. Patel: *Mater. Charact.*, 2005, vol. 54, pp. 13–20.
[35] X. Li, S.M. Xiong, and Z. Guo: *J. Mater. Sci. Technol.*, 2016, vol. 32, pp. 54–61.
[36] J. Campbell: in *Complet. Cast. Handb.*, 2nd ed., Elsevier Ltd., 2015, pp. 447–528.
[37] C.D. Lee and K.S. Shin: *Acta Mater.*, 2007, vol. 55, pp. 4293–4303.

Tables

	Composition (Wt.%)			
Condition	Al	Mn	Zn	Mg
AM40	3.80	0.55	0	Bal.
AM50	4.60	0.41	0	Bal.
AM60	6.05	0.44	0	Bal.
AM70	7.05	0.44	0	Bal.
Mg-3Al	3.12	0.09	0.06	Bal.
Mg-5Al	4.80	0.09	0.06	Bal.
Mg-9Al	8.99	0.11	0.05	Bal.
Mg-12Al	11.35	0.10	0.11	Bal.

Table 5.1: Composition of each casting condition as measured by optical Emissions spectroscopy.

Condition	Plate thickness (mm)	Area fraction of Porosity (%)
AM series as-cast	2.5	0.7
AM series as-cast	5	0.79
AM series ST	2.5	1
AM series ST	5	0.89
AM series HIP	2.5	0.46
AM series HIP	5	0.39
Mg-Al as-cast	2.5	3.33
Mg-Al as-cast	5	1.32

Table 5.2: Area fraction of porosity for each plate condition, averaged across Al contents

Condition	As Cast Ductility (%)	ST Ductility (%)	HIP Ductility (%)	AC n	ST n	HIP n
AM40 2.5mm	13.8 ± 2.8	14.2 ± 3.0	15.3 ± 3.5	0.35	0.34	0.33
AM50 2.5mm	13.2 ± 2.4	-	17.5 ± 2.9	0.35	-	0.35
AM60 2.5mm	10.0 ± 1.9	-	14.3 ± 4.6	0.32	-	0.35
AM70 2.5mm	5.4 ± 1.4	8.0 ± 1.7	8.1 ± 3.4	0.26	0.34	0.31
AM40 5mm	9.6 ± 2.0	9.1 ± 1.5	13.0 ± 3.2	0.38	0.36	0.34
AM50 5mm	6.9 ± 1.7	-	11.4 ± 2.8	0.34	-	0.35
AM60 5mm	7.4 ± 2.0	-	9.6 ± 3.2	0.32	-	0.35
AM70 5mm	5.3 ± 1.2	6.8 ± 2.0	6.2 ± 2.2	0.28	0.33	0.29

Table 5.3: Average elongation to failure (%) and Hollomon strain hardening exponent (n) for all AM series processing conditions.

Binary Composition	Ductility (%)	n
Mg-3 2.5mm	20.5 ± 5.2	0.34
Mg-5 2.5mm	12.9 ± 3.9	0.32
Mg-9 2.5mm	5.4 ± 1.8	0.23
Mg-12 2.5mm	2.6 ± 1.5	0.20
Mg-3 5mm	16.0 ± 6.4	0.38
Mg-5 5mm	9.7 ± 3.8	0.33
Mg-9 5mm	6.4 ± 1.9	0.25
Mg-12 5mm	2.7 ± 0.6	0.18

Table 5.4: Ductility (average elongation to failure, %) and strain hardening exponent, n, for the as-cast binary alloys.

Alloy	Thickness	Condition	σ_T	σ_0	m	R^2
AM40	2.5mm	AC	9.77	4.48	1.13	0.96
		ST	0	15.40	5.21	0.98
		HIP	0	17.06	3.90	0.89
AM70	2.5mm	AC	1.75	4.10	2.83	0.97
		ST	0	8.76	4.87	0.94
		HIP	1.1	7.85	2.37	0.97
AM40	5mm	AC	0	10.46	4.89	0.93
		ST	1.75	7.97	5.65	0.97
		HIP	2.93	11.36	3.57	0.99
AM70	5mm	AC	0	5.84	4.65	0.96
		ST	0	7.56	3.56	0.97
		HIP	0.82	6.08	2.51	0.99

Table 5.5: Values for 3-parameter Weibull distributions for selected conditions

Figures

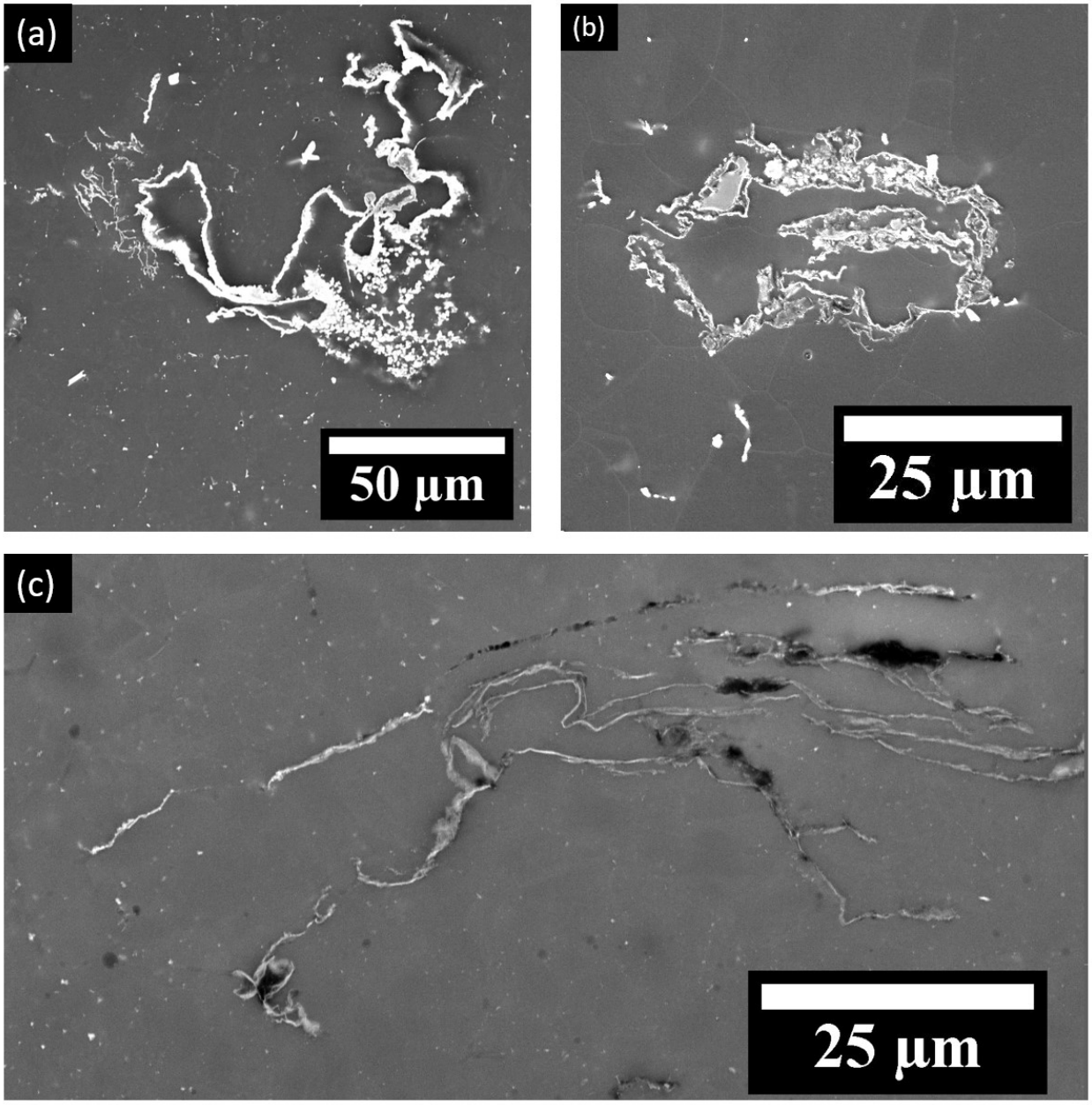

Figure 5.1: Examples of oxide film formation in these alloys.

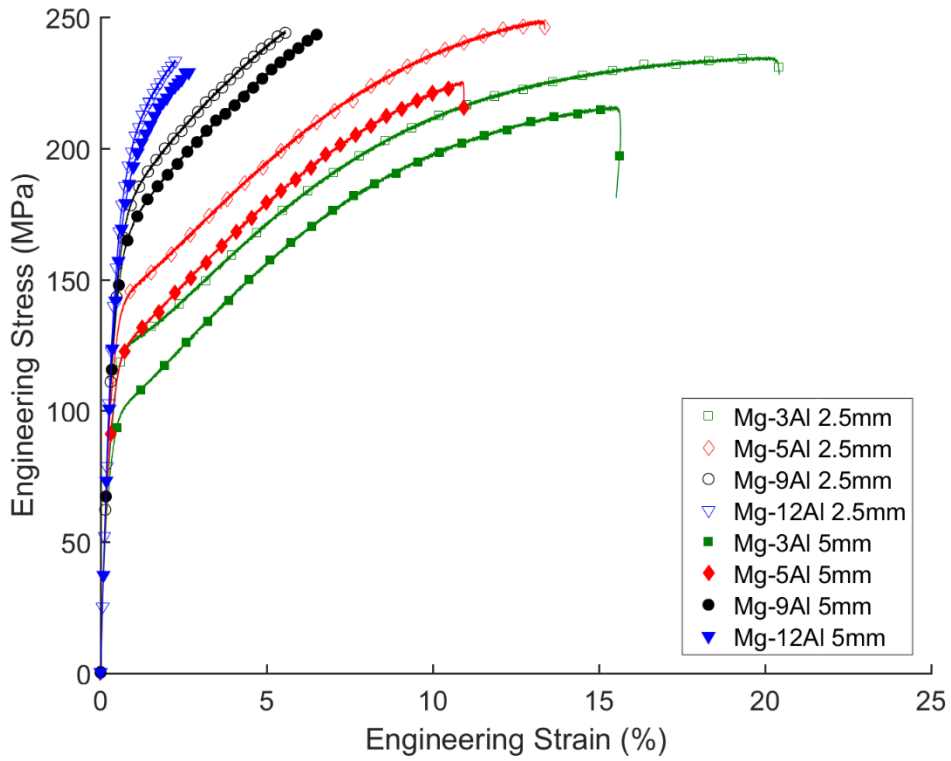

Figure 5.2: Representative stress-strain curves for the binary Mg-Al alloys

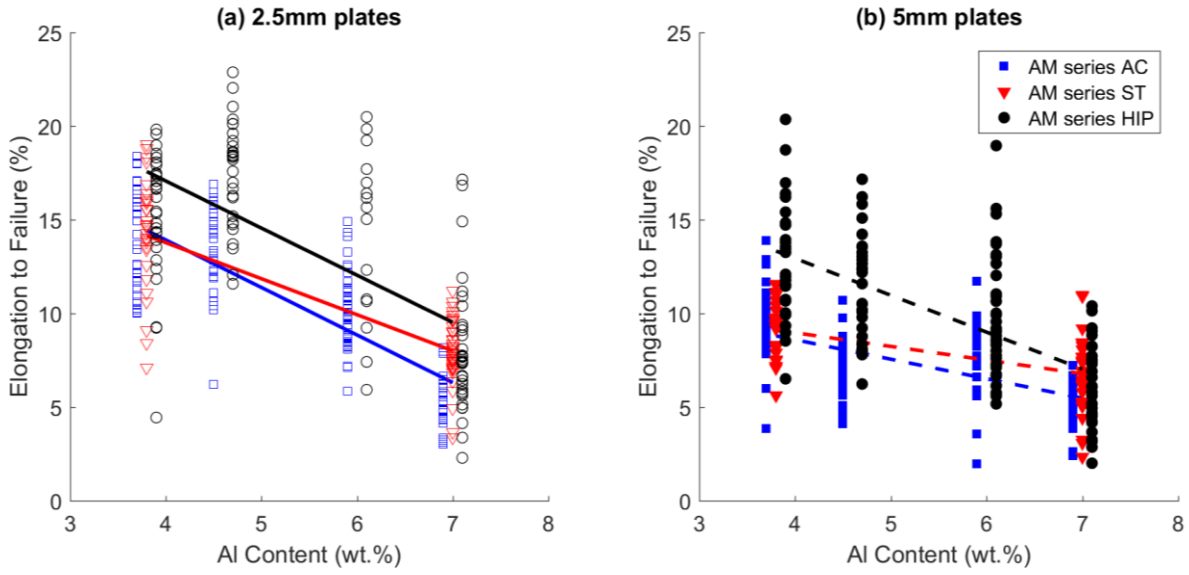

Figure 5.3: The influence of Al content, solution treatment and HIP on ductility for AM series alloys in the (a) 2.5mm plates and (b) 5mm plates.

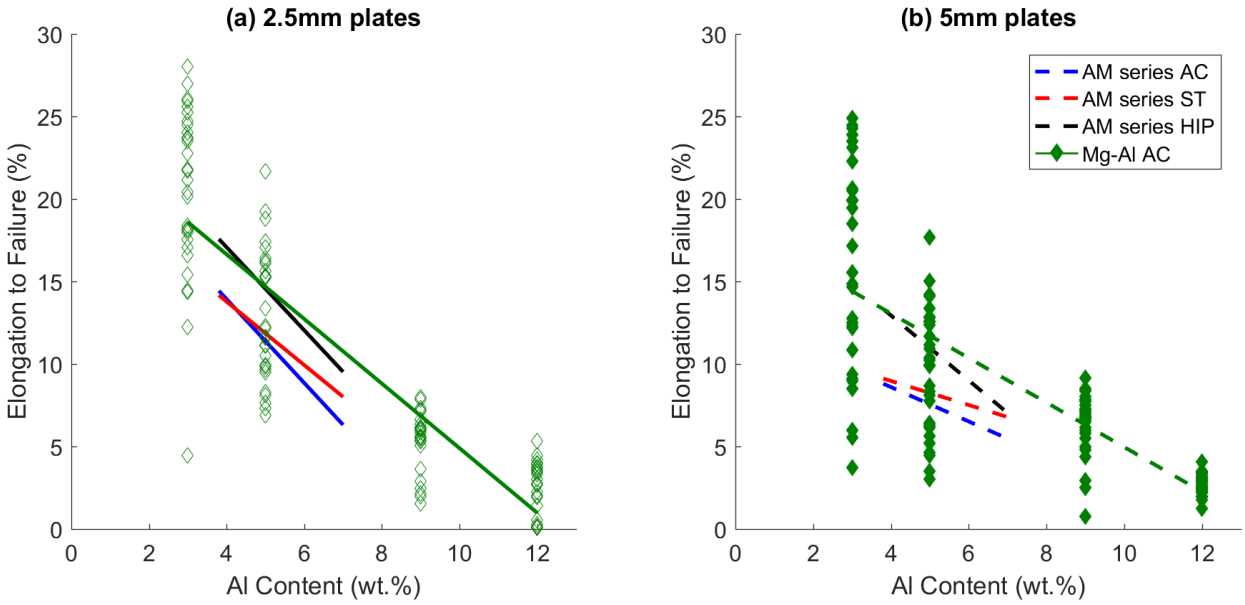

Figure 5.4: The influence of Al content on ductility for the binary Mg-Al alloys in the (a) 2.5mm plates and (b) 5mm plates.

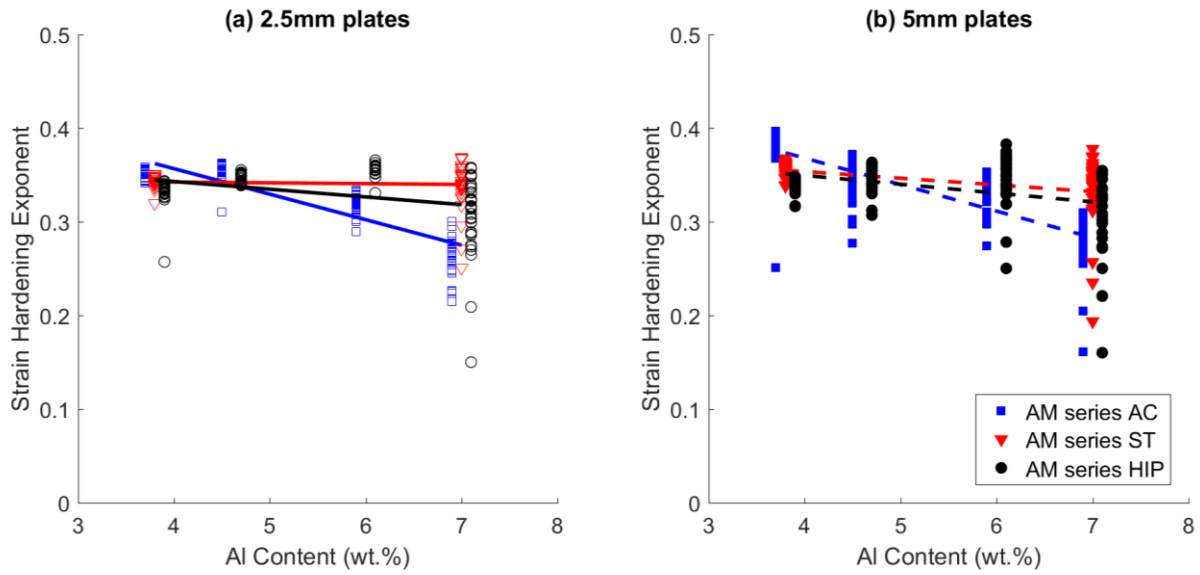

Figure 5.5: The influence of Al content, ST and HIP on strain hardening exponent in the (a) 2.5mm plates and (b) 5mm plates.

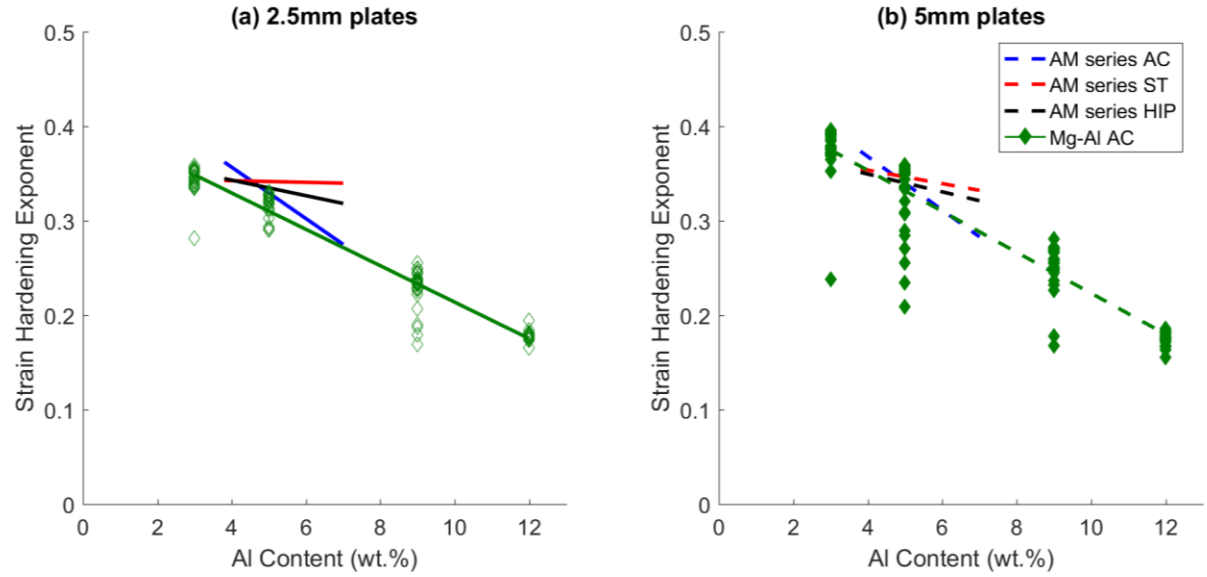

Figure 5.6: The influence of Al content on the strain hardening exponent in the binary Mg-Al alloys for the (a) 2.5mm plates and (b) 5mm plates.

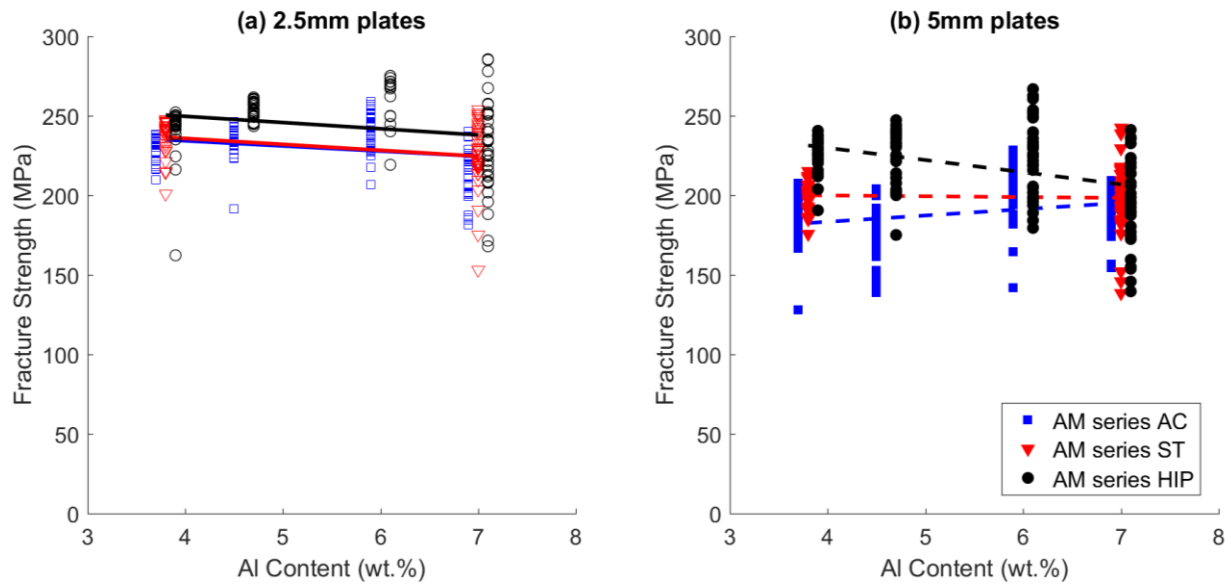

Figure 5.7: The influence of aluminum content, ST and HIP on the fracture strength of AM alloys in the (a) 2.5mm plates and (b) 5mm plates.

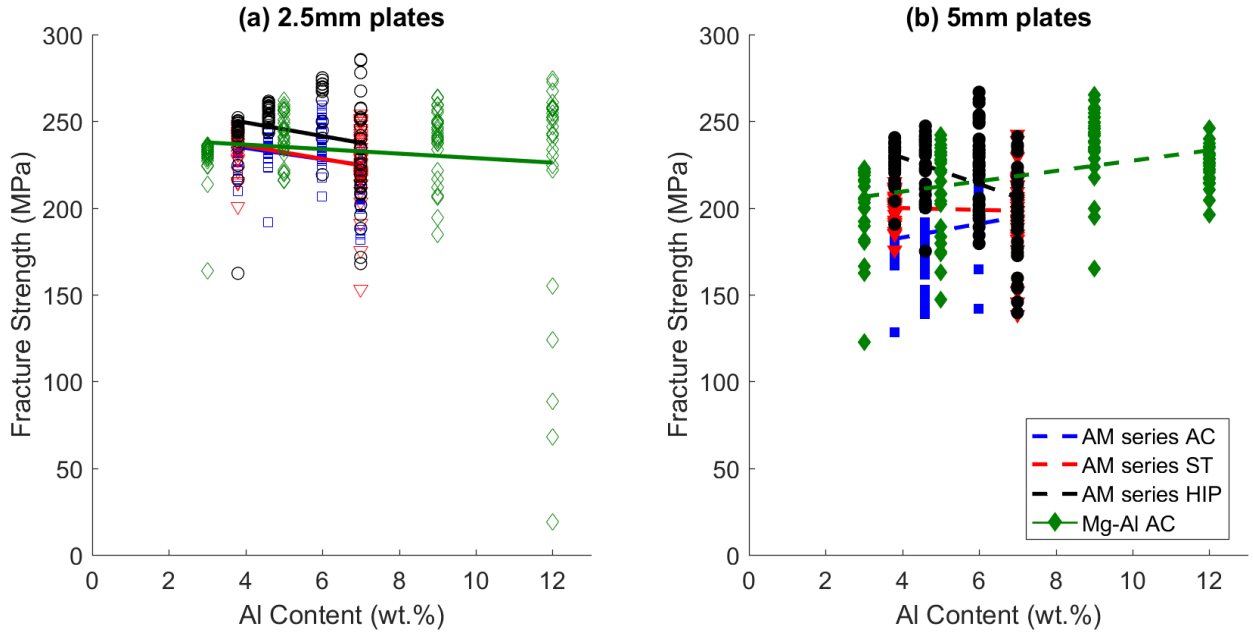

Figure 5.8: The influence of Al content on the fracture strength in the binary Mg-Al alloys for the (a) 2.5mm plates and (b) 5mm plates.

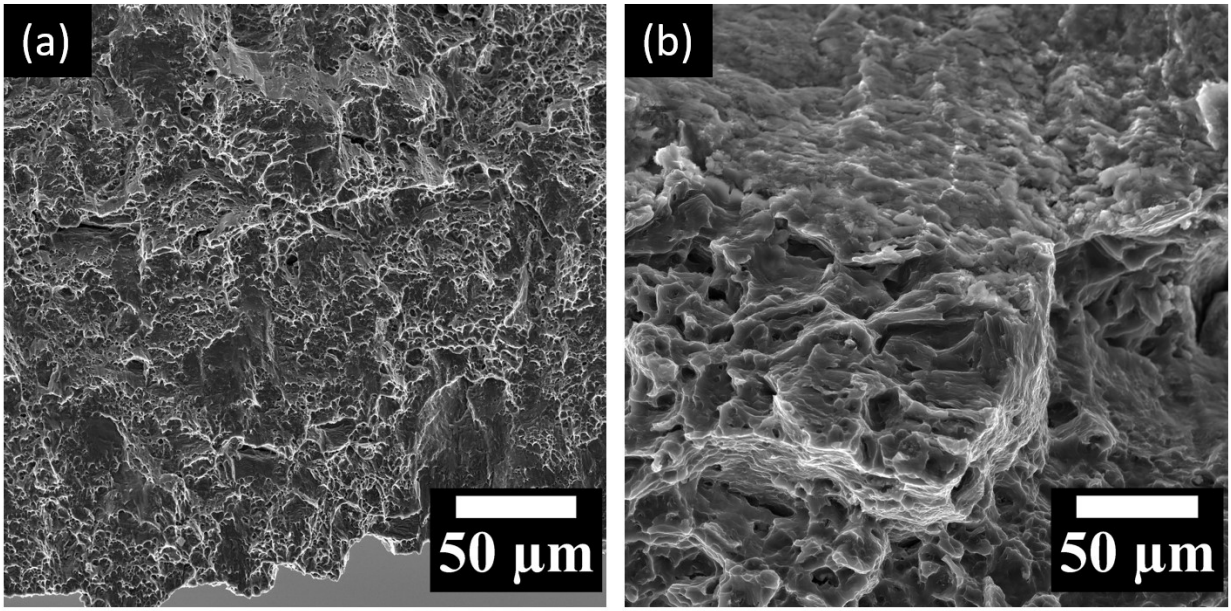

Figure 5.9: Reference fractographs for regions where (a) ductile and (b) brittle failure is observed.

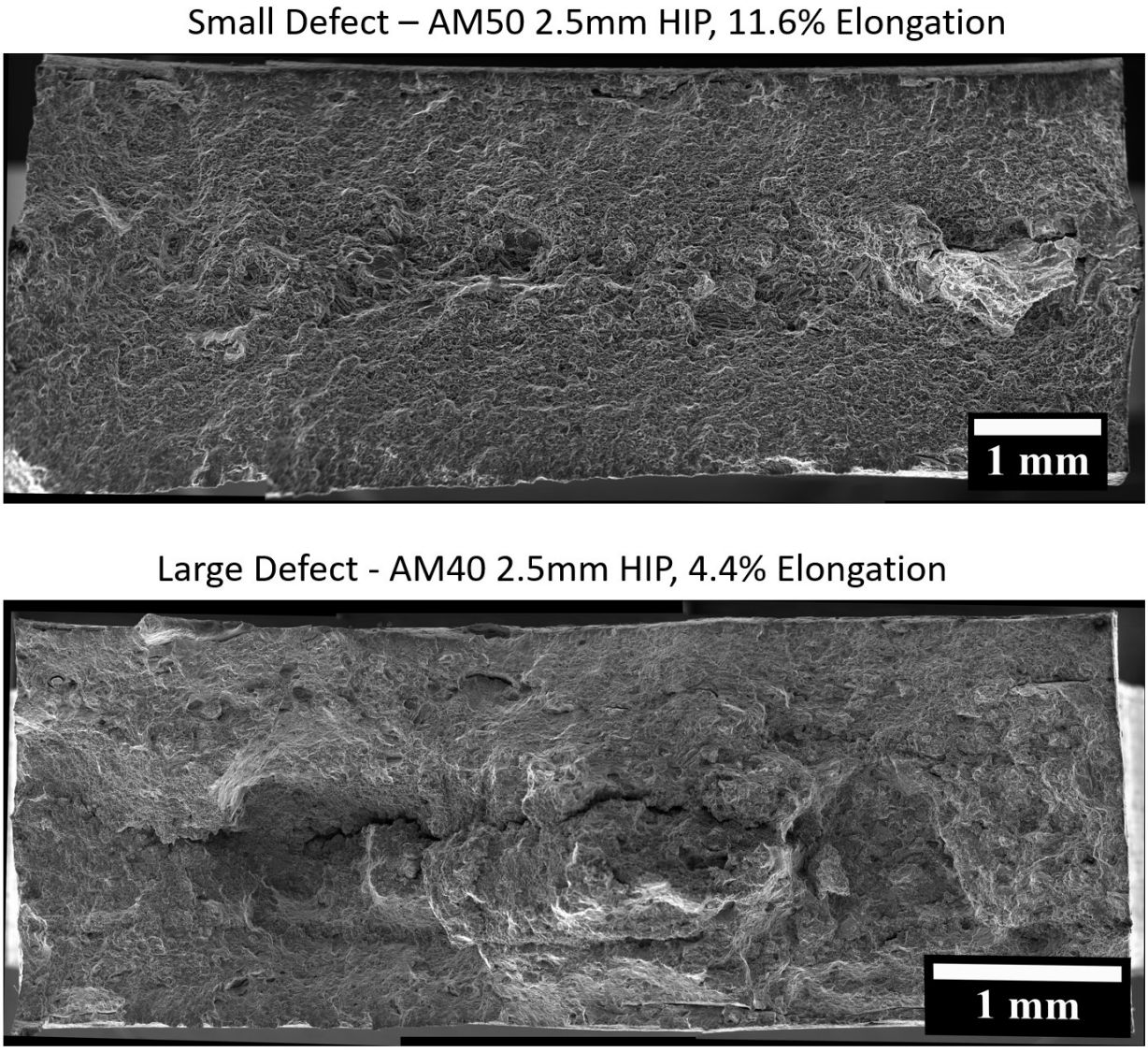

Figure 5.10: Representative fracture surfaces for small (top), and large defects (bottom).

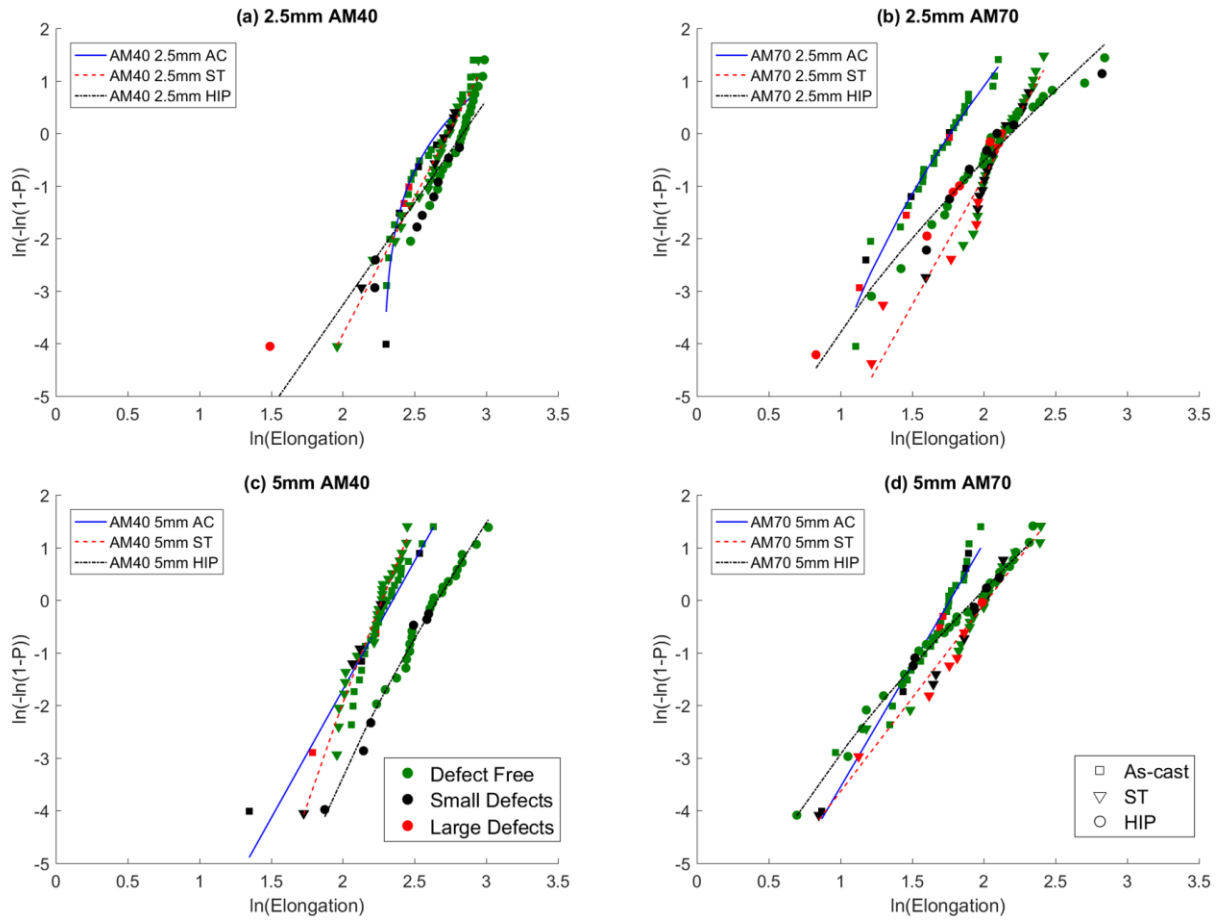

Figure 5.11: Cumulative probability functions of the (a) AM40 2.5mm, (b) AM70 2.5mm, (c) AM40 5mm, and (d) AM70 5mm plates. Defect level observed on the fracture surface is plotted for no defects, small, and large fractions in the as-cast, ST and HIP conditions.

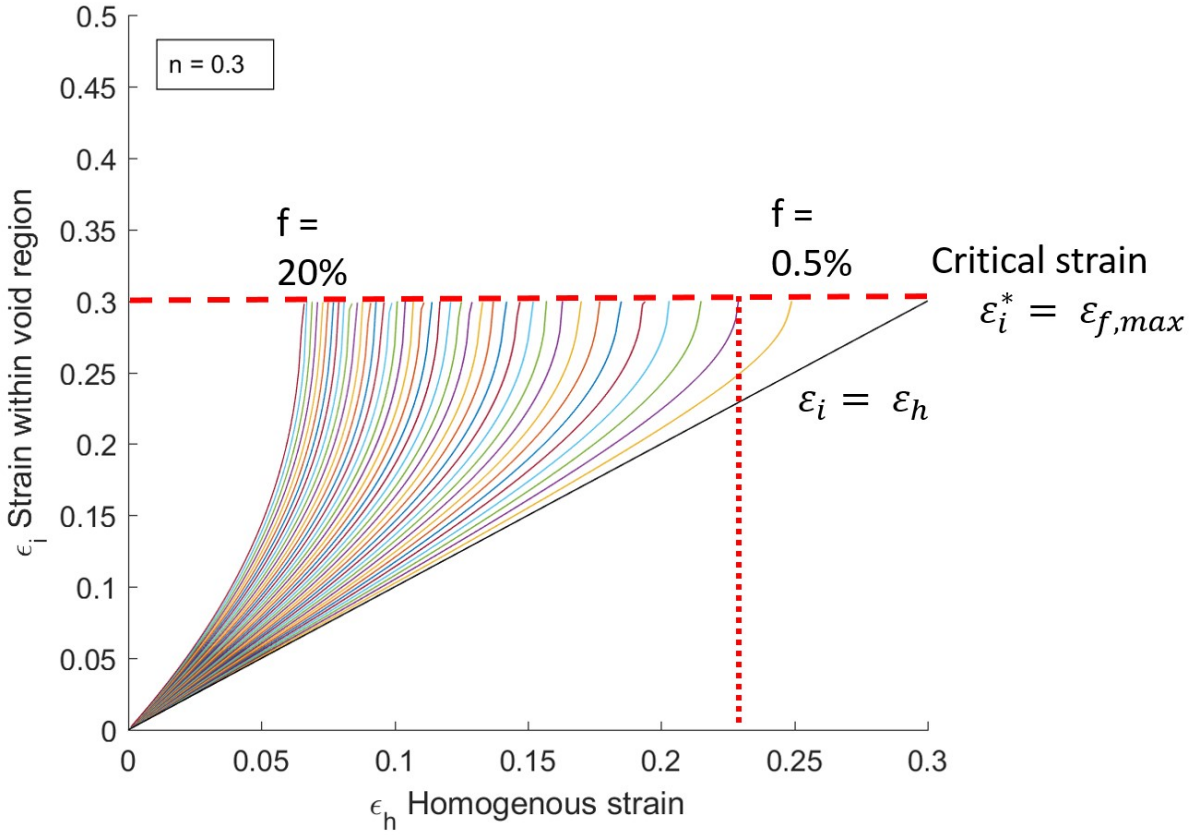

Figure 5.12: The inhomogeneous strain, ε_i, in the defect region, plotted as a function of the homogenous strain, ε_h, for various defect fractions, f. The predicted failure strain is found at the critical strain, ε_i^* in the inhomogeneous region.

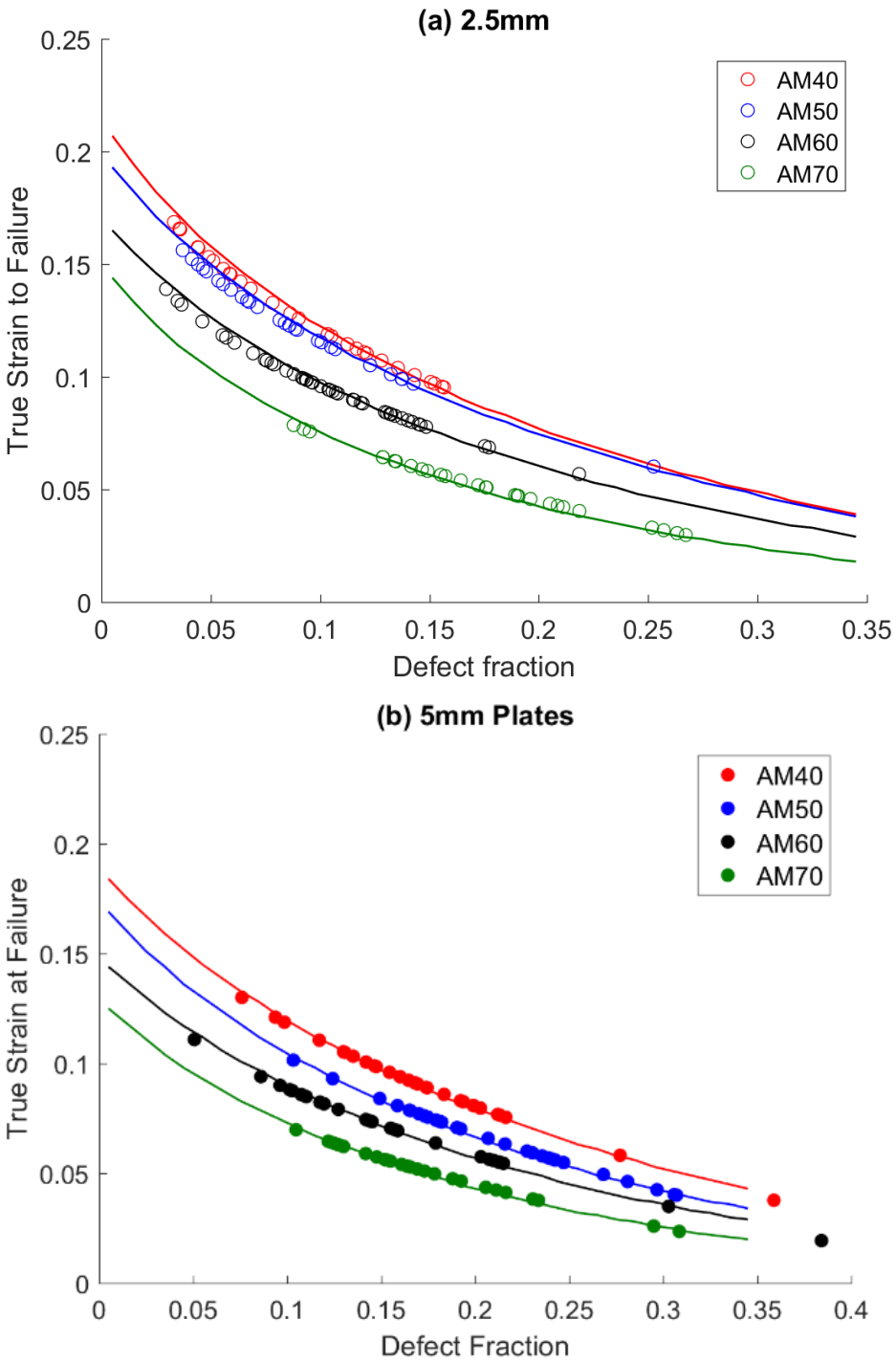

Figure 5.13: Cumulative distribution of true strain to failure as a function of the predicted defect fraction found by Equation 5.3 in the AM series alloys. It is found that the (a) 2.5mm plates tend to have a lower predicted defect fraction than the (b) 5mm plates.

Chapter 6

Conclusions and Future Work

6.1 Conclusions

By quantifying the effects of processing on the microstructure and tensile behavior in SVDC Mg alloys, trends between the two can be better understood. This allows these relationships to be used in predictive models in more complex castings for increased usage in automotive applications [1].

The microstructure and tensile behavior of SVDC Mg-Al-Mn as-cast alloys have been quantitatively characterized for a range of Al contents and plate thicknesses. It is observed that the yield strength increases, and the ductility and strain hardening exponent decrease with increasing Al content. Based on the microstructure and tensile characterization, a physics-based model has been developed that captures the influence of alloy content and plate thickness on yield strength. This model takes in to account microstructure gradients created by the die casting process that exist in the skin and core regions of high pressure die castings. The increase in yield strength is modeled using a linear super position model which accounts for the grain boundary hardening, solid solution strengthening, and dispersion hardening. Microstructure quantification of the as-cast material shows that the eutectic β-phase fraction increases with Al content, and that there is no

dependence of the in-mold grain size on Al. Significant solute hardening effects are observed and these separately involve classical solute hardening and a solute dependence of the Hall-Petch relationship.

The yield strength model that was developed takes into account the bimodal nature of the grain structure in high pressure die castings. The most significant effects on strength are observed to be grain boundary hardening and solid solution strengthening. Dispersion strengthening due to the presence of β-$Mg_{17}Al_{12}$ particles is estimated to provide only a minimal increase in the strength. The yield strength was significantly lower in the 5mm plates as compared to the 2.5mm plates. This is attributed to the difference in ESC fractions observed in the skin and core. The relative size and area fraction of ESCs was observed to be higher in the 5mm plates in both the skin and the core.

In order to validate the yield strength model developed in Chapter 3, alloying and processing were varied in order to isolate different microstructural features predicted to have an effect on the tensile behavior. To accomplish this, the local microstructure and tensile behavior was quantitatively characterized for a wide range of Mg-Al and Mg-Al-Mn alloys in solution heat treated and hot isostatically pressed conditions. The effects of solution treatment and HIP on the grain size, β-phase formation, and solute redistribution are all quantified. It is observed that after either solution treatment or HIP, the yield strength is observed to be independent of alloy Al content. This is attributed to the homogenization of the local microstructure which reduces or eliminates the solute rich regions near the grain boundaries and can be appropriately incorporated into the Hall-Petch locking parameter. Yield strength was not significantly reduced by solution treatment, which could be used as a processing option to increase corrosion resistance in these alloys.

The microstructures used in this study to validate a linear superposition model for strength were solute content, grain size, β-phase fraction and porosity. The model also accounts for the differences in these metallurgical variables that exist between the die casting skin and its core regions. The relative impact of the skin and core were assessed using microtensile tests. The difference in yield strength measured in the microtensile tests were consistent with that predicted by the model. The linear superposition model works well for predicting the strengths of as-cast alloys, as it predicted the yield strength of the Mg-Al binary alloys well.

The effects of alloying, plate thickness and processing on the ductility have also been studied. It is found that with increasing Al content, the ductility decreases. It is observed that for both the solution treated and HIP processing conditions, the average ductility increases. This is true of all Al contents and plate thicknesses. However, it is also observed that regardless of heat treatment, the lower bound of ductility remains the same. This is likely due to the deleterious effects of oxide bifilms on the ductility. There are two potential mechanisms for the reduction in ductility – a decrease in the effective reduction in cross sectional area, or as a pre-existing crack in the material. By varying the microstructure using ST and HIP, the hierarchy of defects can be validated, in that casting defects and oxide bifilms have the strongest negative effect on ductility, followed by shrinkage porosity, and β-phase fraction.

The effects of the local defect fraction on the ductility can also be estimated using the Ghosh model coupled with an intrinsic ductility and a calibrated "effective defect fraction". It is found that the reduction in ductility increases with increasing effective local defect fraction, which is predicted to be between 5 and 30% of the local area. These effective defect fractions are much higher than the observed defect fractions on the fracture surface pointing out the limitations of this approach. The Ghosh model predicts that the ductility is a function of the strain hardening exponent

and local defect fraction [2,3]. This decrease in ductility with defect fraction is predicted to be related to the strain localization due to the reduction in cross sectional area. The fracture surfaces were qualitatively characterized for defect fraction, and while large defects generally led to lower observed ductilities, there were some notable exceptions. This work highlights the importance of understanding the role of casting conditions and casting defects on the overall microstructure and mechanical properties. By better understanding the relationships, the properties can be better controlled for increased use in production parts.

6.2 Future Work

The work in this dissertation has made a contribution to the understanding of the mechanical behavior of high pressure die cast Mg alloys by connecting the tensile behavior with the microstructural features present. Further study is recommended to address several important questions which follow from this work, but which were beyond the current scope.

One important finding was that after solution treatment or HIP processing, yield strength was constant over the range of Al from 4 to 7 wt.% Al in the ternary AM series alloys. This is in sharp contrast to the as -cast conditions which showed a strong dependence of yield strength on Al content. The exact cause of this is still unclear and requires further study. It is posited that the lack of the dependence on Al content for these condition is due to the homogenization of the microstructure and the elimination of the solute enrichment near the grain boundaries. Further study is required to ascertain the impact of solute enrichment near the grain boundaries on the total grain boundary hardening, and how this would change with grain size variation. The effect of alloying on the grain boundary locking parameter, k_y, is still not completely clear. Current predictions for the relationships between k_y and alloying are all based on fits from experimental data. The fundamental mechanisms for this relationship are still unknown, and could significantly

impact the ability to predict the effects of alloying on the grain boundary hardening behavior of cast alloys.

Another important piece of continued work is a complete analysis of the effect of HIP on Mg castings, and isolation of secondary phases. During the cooling process of the HIP cycle, some β-phase was formed. In order to isolate the β-phase effects in HIP, an additional ST process is needed in order to fully de-convolute the effects of β-phase and shrinkage porosity on the ductility. The understanding of the effect of different HIP times, temperatures and heating and cooling rates in Mg alloys also has not been explored fully. The effect of cooling rates can have a significant effect on the microstructure, and the observed properties in turn. Recent developments in HIP allow for faster cooling rates, though not at the rate of a water quench. Depending on the achievable speeds, it may be necessary to conduct a post-HIP solution treatment.

Further work is needed to understand the effects of large defects on the ductility. A broad range of ductility values were observed in this study, however there is still not a full understanding of the effect of local defects on the tensile behavior. X-ray tomography has been used to characterize porosity in these alloys [4,5], but the effects of oxide defects have not been effectively explored. Oxide films are difficult to isolate, and the relationship between the size of the defect, location relative to a casting surface, and the overall ductility is still unclear. In addition, the factors controlling the upper bound of ductility in the nucleation and growth of voids in these alloys have not been studied due to the prevalence of casting defects. The continued use of these tensile results to develop a weak-link model for the ductility as controlled by each of the different factors is an area of continued study in these alloys.

Finally, component level tests are needed to validate the use of the models developed in this study with the actual deformation behavior of cast parts. Particular areas of study should

include machining effects on excised tensile bars from cast plates compared with as-cast surfaces in cast plates and large HPDC components [6,7]. The use of component level tests such as bend testing would allow the study of the change in microstructure with casting parameters and alloying, and how those parameters could be used in more realistic stress states to predict component deformation and failure.

References:

[1] J.H. Forsmark, J.W. Zindel, L. Godlewski, J. Zheng, J.E. Allison, and M. Li: *Integr. Mater. Manuf. Innov.*, 2015, vol. 4.
[2] A K Ghosh: *Acta Metall.*, 1977, vol. 25, pp. 1413–24.
[3] C.H. Cáceres and B.I. Selling: *Mater. Sci. Eng. A*, 1996, vol. 220, pp. 109–16.
[4] J. Song, S. Xiong, M. Li, and J.E. Allison: *Mater. Sci. Eng. A*, 2009, vol. 520, pp. 197–201.
[5] K.S. Choi, E.I. Barker, G. Cheng, X. Sun, J. Forsmark, and M. Li: *SAE Int. J. Mater. Manuf.*, 2016, vol. 9, pp. 2016-01–0290.
[6] J.H. Forsmark, J.W. Zindel, L. Godlewski, and A. Caliskan: *SAE Int.*, 2012, pp. 2–10.
[7] J.H. Forsmark, Z. Dowling, K. Gibson, C. Mueller, L. Godlewski, J.W. Zindel, and J.M. Boileau: *SAE Int. J. Mater. Manuf.*, 2015, vol. 8.